Strength and dendritic organization of thalamocortical synapses onto excitatory layer 4 neurons

Carl Edward Schoonover

Submitted in partial fulfillment of the
requirements for the degree of
Doctor of Philosophy
under the Executive Committee
of the Graduate School of Arts and Sciences

COLUMBIA UNIVERSITY

2013

Abstract

Strength and dendritic organization of thalamocortical synapses onto excitatory layer 4 neurons

Carl Edward Schoonover

The thalamus is a potent driver of cortical activity, even though cortical synapses onto layer 4 (L4) neurons outnumber thalamic synapses ten to one. Previous *in vitro* studies have suggested that enhanced efficacy of thalamocortical (TC) relative to corticocortical (CC) synapses explains the effectiveness of the thalamus. We investigated possible key anatomical and physiological differences between these inputs onto excitatory L4 neurons *in vivo*. We developed a high-throughput light microscopy method, validated by electron microscopy, to completely map the locations of synapses across an entire dendritic tree. This demonstrated that TC synapses are slightly more proximal to the soma than CC synapses, but detailed compartmental modeling predicted that dendritic filtering does not appreciably

favor one synaptic class over another. Measurements of synaptic strength in intact animals revealed that both TC and CC synapses are weak and approximately equivalent. We conclude that thalamic potency relies, not on enhanced TC strength, but on coincident activation of converging inputs.

Table of Contents

List of Figures

Acknowledgements

Preliminary light-microscopy data were generated, by my advisor, Dr. Randy M. Bruno, in the course of his postdoctoral fellowship in the laboratory of Dr. Bert Sakmann at the Max Planck Institute in Heidelberg, Germany. There, he was assisted by Dr. Verena Wimmer, who contributed to the development of the confocal imaging method, and Verena Schilling, who performed some of the imaging and reconstruction. After Dr. Bruno established his laboratory at Columbia University, I built upon and extended these preliminary methods and results.

In collaboration with Dr. Juan-Carlos Tapia, I developed the correlative light/electron microscopy method that relies on scanning electron microscopy. This effort rested upon preliminary results I obtained in the course of developing, in collaboration with Rich Blazeski and Dr. Carol A. Mason, an approach that employs transmission electron microscopy. The correlative light-/electron-microscopy experiment was performed in close collaboration with all three. My

fellow graduate student, Elaine Zhang, performed the Channelrhodopsin virus injections.

I performed all the physiological experiments and the biophysical modeling.

Limited sections of Chapters 1 and 2, and significant portions of Chapters 3, 4 and 5 form part of a manuscript, which we wrote together, and which was edited by all of the collaborators listed above. It is currently in review.

Preface

The neurons in a given area of the neocortex receive long-range projections from many presynaptic circuits, as well as inputs from neighboring neurons. To permit efficient transfer of the right information, at the right time, it would seem necessary for each circuit to deploy mechanisms that gate long-range and local inputs, allowing the correct one(s) to predominate. In addition, each presynaptic circuit must be able to influence the postsynaptic circuit despite the likelihood that the number of synapses that can carry its information will constitute only a fraction of the total synapses onto a single postsynaptic neuron.

The thalamic projection to Layer 4 of neocortex, perhaps one of the most intensely studied long-range projection, constitutes a good model for addressing this second problem: despite controlling the state of only 10 percent of the synapses in the thalamorecipient neuropil, the thalamocortical projection can wield outsized influence over the activity of the postsynaptic circuit. What mechanism ensures this efficient transmission of information?

In **Chapter 1**, I summarize the anatomy of the somatosensory system from

the periphery to the neocortex, and focus on the connectivity principles of its fourth layer. A discussion of available methods for the anatomical study of central synapses follows. In **Chapter 2**, I outline aspects of synaptic transmission and integration that are relevant to my project, with an emphasis on the passive filtering of dendritic arbors. In **Chapter 3**, I present a fast, reliable light-microscopy-based synapse mapping strategy, which we employed to map the complete dendritic arbors of excitatory Layer 4 neurons, revealing asymmetrical distributions of thalamic and cortical inputs. In **Chapter 4**, I describe a compartmental model of this cell type and determine that those anatomical distributions do not play a functional role in how it integrates synaptic inputs. This prediction is then tested *in vivo*. In **Chapter 5**, I discuss the technical limitations of this work, place our results in the context of other work on this subject, and discuss its implications on the mechanism by which thalamic information is transmitted to the neocortex.

Chapter 1

Anatomy of Layer 4 Barrel Cortex Circuitry

1.1. General anatomical organization of the somatosensory system

In the rat, mechanoreceptors at the base of the whiskers on the snout's whisker pad detect whisker motion, which is transmitted by afferent axons in the trigeminal nerve to the principal trigeminal nucleus and the spinal trigeminal nucleus (**Figure 1.1.**) (Lubke and Feldmeyer 2007). These nuclei relay sensory information to primarily two nuclei in the thalamus, the ventroposterior medial nucleus (VPM) and the posterior medial nucleus (POm). In the VPM, neurons that encode sensory information signals from individual whiskers are grouped into "barreloids" that have a one-to-one correspondence with the whiskers on the whisker pad, and consist of an estimated 250-300 cells. (Land, Buffer et al. 1995) Both VPM and POm project to the posteromedial barrel subfield (PMBSF) the primary

somatosensory cortex but are segregated into two pathways: “lemniscal” and “paralemniscal” (Jones and Diamond 1995).

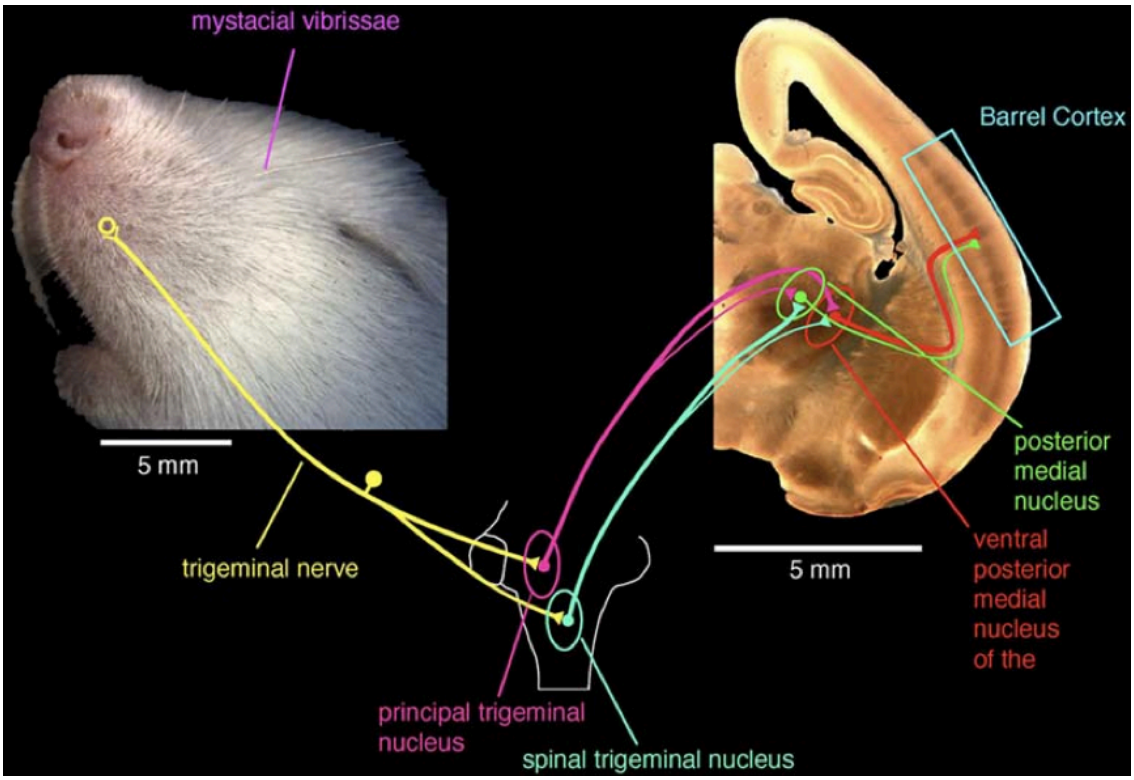

Figure 1.1. *General organization of the somatosensory system. Mechanoreceptors detect whisker motion, which is transmitted to the brainstem by the trigeminal nerve. There, the principal trigeminal nucleus and the spinal trigeminal nucleus project to both the posterior medial nucleus (POm, paralemniscal system) and the ventral posterior medial nucleus (VPM, lemniscal system) of the thalamus. Both nuclei project to the primary somatosensory cortex, in complementary ways with respect to its lamina and barrel/septum organization. Figure from (Lubke and Feldmeyer 2007).*

As for the VPM barreloids, the PMBSF exhibits a striking, and consistent, spatial organization that reflects the topography of the whisker pad on the rodent snout (**Figure 1.2.**). The one-to-one relationship between individual "barrels" and specific whiskers on the whisker pad was proposed based on Nissl-stained sections cut tangential to the *pia mater* (Woolsey and Van der Loos 1970), although histological studies in the first quarter of the 20th century had already reported their existence. (Lorente de Nó 1922)

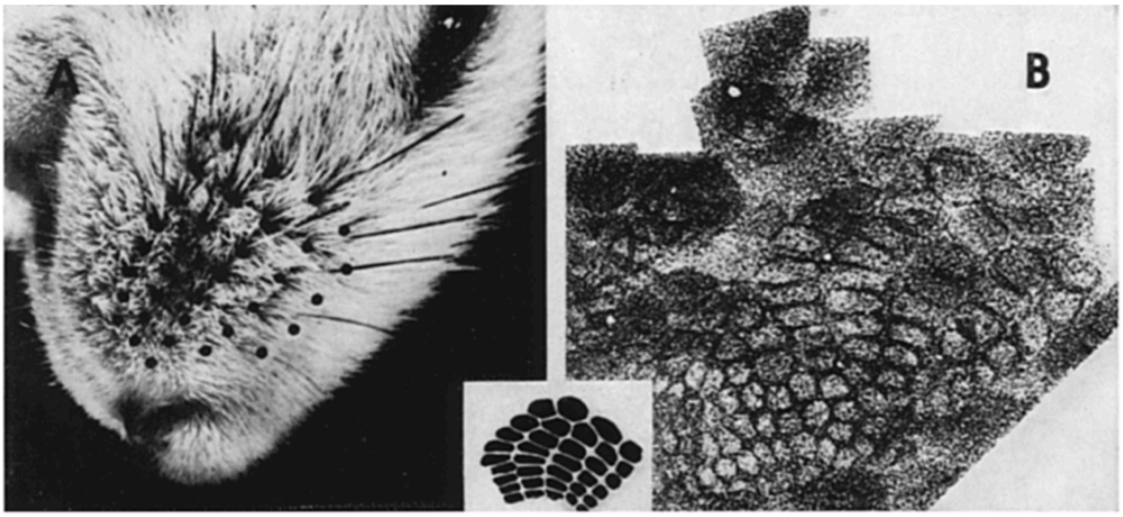

Figure 1.2. *One-to-one correspondence between whiskers and barrels. Figure illustrating the relationship between individual whiskers on the whisker pad of a rat (left), and individual barrels in L4 of somatosensory cortex (right). From (Woolsey and Van der Loos 1970).*

The lemniscal pathway is formed by afferents from VPM to areas of the PMBSF vertically aligned with individual barrels, specifically lower Layer 3 (L3), L4 (which forms the barrel and receive the highest density of VPM inputs), Layer 5B (L5B), and Layer 6A (L6A). The paralemniscal pathway is formed by afferents from POm to the septa—the spaces between neighboring barrels—in L4, as well as Layer 1 (L1) and Layer 5A (L5A) (**Figure 1.3.**) (Lubke and Feldmeyer 2007, Wimmer, Bruno et al. 2010). For the most part, neurons in a given barrel receive their VPM inputs the corresponding barreloid (Land, Buffer et al. 1995, Swadlow 1995, Oberlaender, Ramirez et al. 2012).

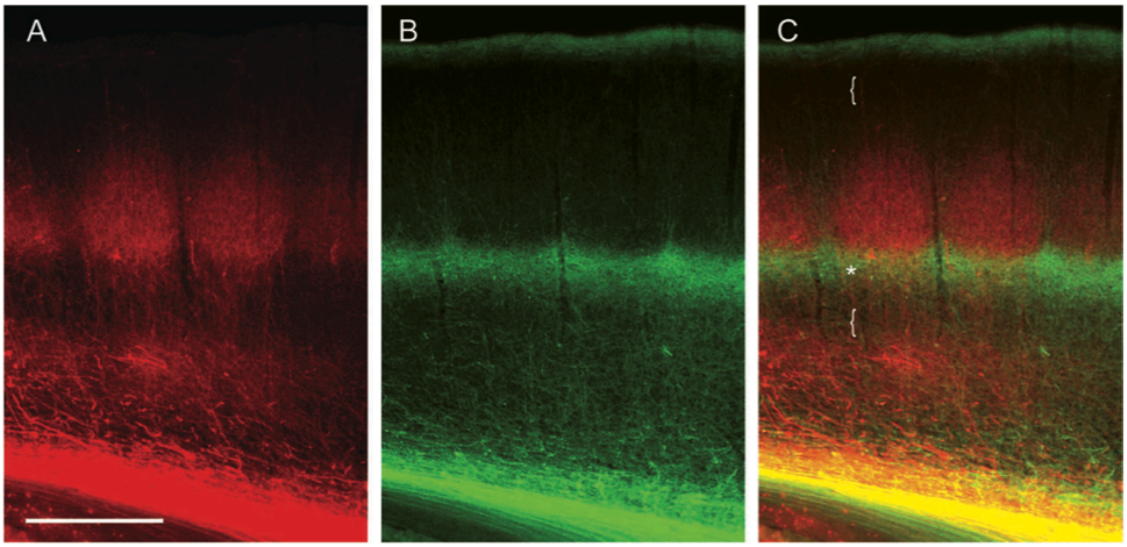

Figure 1.3. *Complementary innervation of VPM and POM axons. Thalamocortical section of rat somatosensory cortex showing the pattern of thalamic axons distribution throughout the cortical layers. VPM neurons are infected with monomeric red fluorescent protein (red, left); POm neurons are infected with*

enhanced green fluorescent protein (EGFP) (green, middle); the right panel shows a merge of the two left panels. Figure from (Wimmer, Bruno et al. 2010).

1.1.1. Sources of thalamocortical and cortical input to excitatory L4 barrel neurons

Inhibitory neurons in L4 account for ~15% of cell bodies; excitatory L4 barrel neurons form two morphological categories: spiny stellate cells (~70%) which do not contain an apical dendrite, and a minority of star pyramids (~15%) which do, but whose dendritic arborization is not as extensive as pyramidal neurons in Layer 2/3 (L2/3) or Layer 5 (L5) (Peters and Jones 1984, Simons and Woolsey 1984, Lubke and Feldmeyer 2007).

The sources of input to excitatory L4 barrel neurons can be divided into thalamocortical (TC) and corticocortical (CC) synapses (**Figure 1.4.**). Because POm does not innervate the barrel in L4, the VPM projection is the sole source of TC inputs to these neurons and is characterized by a high convergence rate of ~0.43, (Bruno and Sakmann 2006). The overwhelming majority of CC inputs are from other L4 barrel neurons, which exhibit significant recurrent connectivity rates (0.2-0.3, (Feldmeyer, Egger et al. 1999)). In addition, a subset of L6 neurons sends an axon collateral to L4 (Lubke and Feldmeyer 2007). Functional L6 to L4 synapses have been observed in paired recordings in acute slices of young adult cat

visual cortex (Stratford, Tarczy-Hornoch et al. 1996), but analogous experiments in the somatosensory cortex of young mice have failed to detect any connections (Lefort, Tomm et al. 2009). Thus, though the anatomy supports a L6 to L4 synapse, it is likely to represent only a small fraction of CC inputs to L4 excitatory neurons.

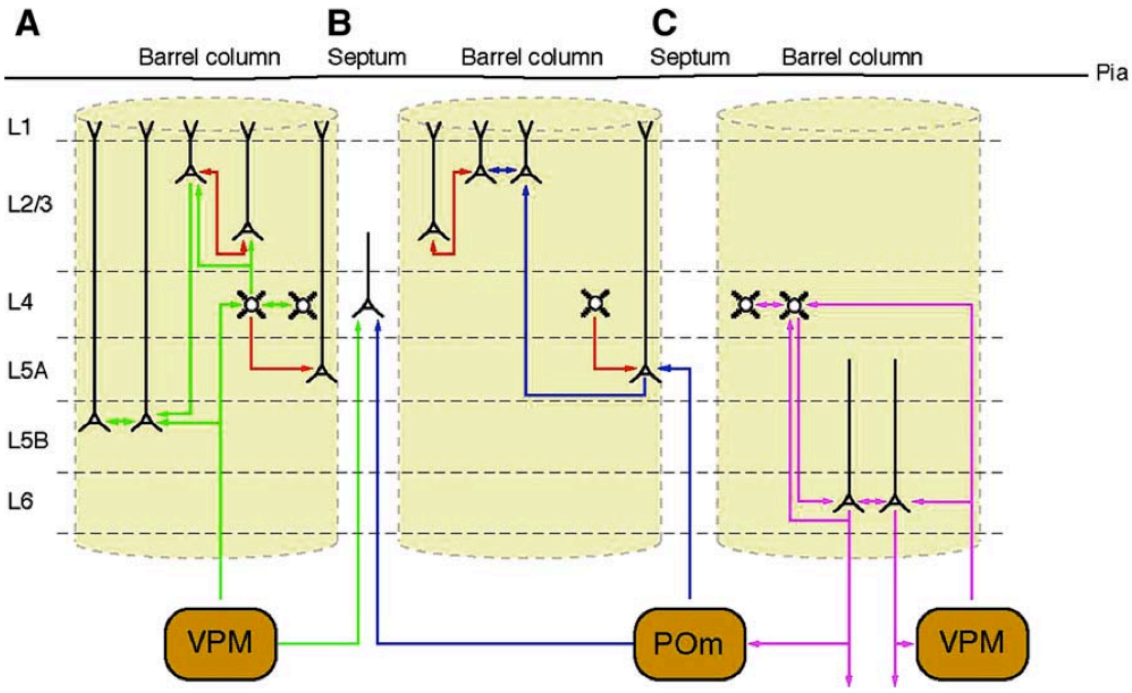

Figure 1.4. *Excitatory connections of the primary somatosensory cortex. L4 barrel excitatory neurons receive excitatory inputs from other L4 barrel neurons, a small number of L6 neurons, and VPM neurons. They do not receive inputs from POm neurons, or any other supra- or infra-granular excitatory neurons. Figure from (Lubke and Feldmeyer 2007).*

1.1.2. Fraction and molecular identity of TC inputs to excitatory L4 barrel neurons

Early studies to distinguish TC from CC synapses in the L4 barrel employed electrolytic lesions performed in the thalamus that render degenerating VPM axons electron-dense (**Figure 1.5.**). Limited segments of dendrites of Golgi-impregnated L4 spiny neurons in L4 were reconstructed allowing visualization of both the spine and the presynaptic terminal under transmission electron microscopy (TEM).

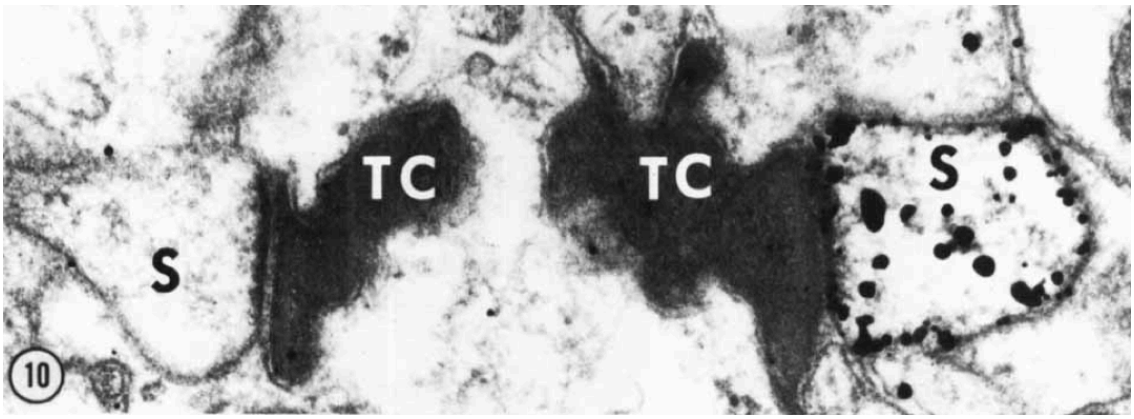

Figure 1.5. *Visualization of TC synapses under TEM. Electron photomicrograph of two spine heads ("S") forming asymmetrical synapses with one or two degenerating TC terminal(s) ("TC"), caused by electrolytic lesion of the VPM. Figure from (Benshalom and White 1986).*

Based on this approach, it was estimated that the fraction of TC inputs to spiny neurons is ~0.14, with pronounced variability from segment-to-segment. TC synapses forming directly onto the shaft of the dendrite account for a marginal fraction (<1%).

The advent of immunolabeling and viral-mediated transfection methods has permitted molecular identification of TC terminals. Vesicular Glutamate Transporter 2 (VGluT2) protein labels thalamic but not cortical terminals in L4 of primary sensory cortex of several mammalian species. VGluT2 exclusively labels thalamic but not cortical terminals in L4 of ferret (Nahmani and Erisir 2005) and mouse primary visual cortex (V1) (Coleman, Nahmani et al. 2010). Lesioning thalamus depletes VGluT2 immunoreactivity in rat somatosensory cortex (Fujiyama, Furuta et al. 2001). In situ hybridization reveals dense VGluT2 expression in thalamus but little or no VGluT2 mRNA in mouse somatosensory cortex except in a subset of Layer 3 (L3) cells (Graziano, Liu et al. 2008), which generally do not establish synapses in L4 (Bruno, Hahn et al. 2009, Lefort, Tomm et al. 2009). Measurements of the perimeter (Graziano, Liu et al. 2008) and area (Nahmani and Erisir 2005) of terminals visualized in 2-dimensional plans obtained using TEM reveal that VGlut2+ terminals are larger than CC terminals in mature animals.

An alternative to immunohistochemistry for labeling terminals is to express a synaptophysin-enhanced green fluorescent protein (EGFP) fusion protein

encoded by an adeno-associated virus delivered to the cell body (**Figure 1.6.**). Overexpression of this fusion protein labels puncta contained within VPM axons, presumably corresponding to either terminals or synaptophysin in the course of being trafficked, without affecting synaptic transmission (Wimmer, Nevian et al. 2004, Wimmer, Broser et al. 2010). Both VGluT2 immunostaining, and bulk injection of synaptophysin-EGFP virus into VPM, result in labeling barrels in L4 of primary somatosensory cortex.

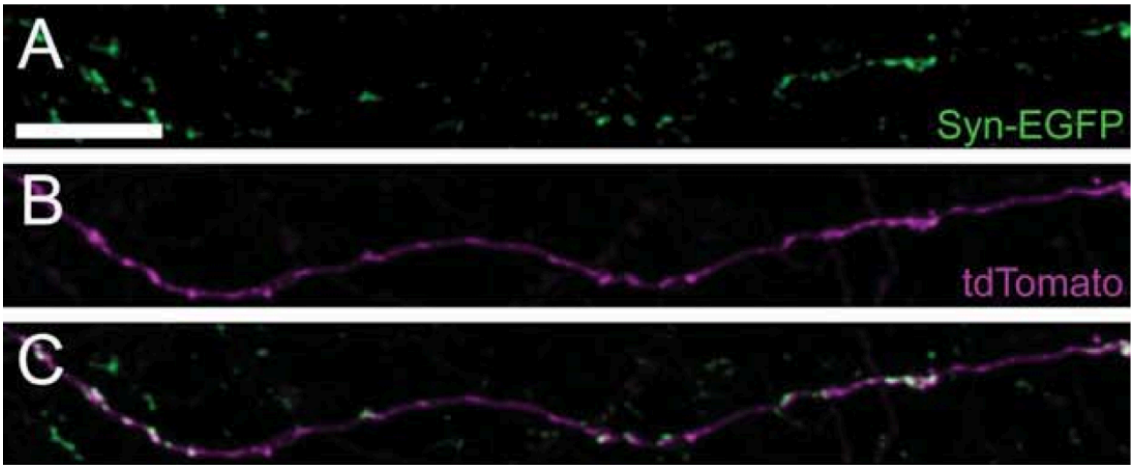

Figure 1.6. *Labeling presynaptic molecules in axons. Synaptophysin-EGFP (Syn-EGFP) (top, green) and tdTomato (middle, purple) simultaneously expressed in a single L2/3 axon above a barrel; the bottom panel shows a merge of the two top panels. The punctate pattern of Syn-EGFP corresponds to synaptic vesicles contained in terminals or large aggregations of synaptophysin in the course of being trafficked. Figure from (Wimmer, Broser et al. 2010).*

1.2. Techniques for the study of the anatomy of synapses

There exist many techniques for mapping the location of a class of inputs onto the dendritic arbor of a given postsynaptic cell type. However, all are subject to tradeoffs between resolution and field of view. Here I review here their strengths and limitations.

1.2.1. Fundamental limits on the resolution of light-based microscopy

Because of their size, certain synapses of the nervous system such as the neuromuscular junction are amenable to study using light microscopy, even in living animals (Lu and Lichtman 2007, Turney, Walsh et al. 2012). However, many of the pre- and post-synaptic structures of the central nervous system, and in particular of the cerebral cortex, are so small, dense and intertwined that they present challenges to study under the light microscope (Briggman and Bock 2012). Perhaps the single most significant barrier to light microscopy-based synaptic anatomy is posed by the fundamental resolution limits the resolution of optical microscopy. An arbitrarily small light point will appear as a blurry volume in the X, Y and Z dimensions referred to as the point spread function (PSF), which is determined by the wavelength λ of light and the numerical aperture (NA) of the objective, defined as:

$$NA = n\sin(\theta) \qquad \textbf{(Eq. 1.1.)}$$

where n is the refractive index of the imaging medium, and θ is the angle of the

objective's aperture angle. The theoretical resolution limit of a light microscope, defined as the separation between two light sources necessary to distinguish them from one another, was first approximated by Ernst Abbe (Abbe 1873) as:

$$\text{Limit}_{xy} = \lambda / 2NA \qquad \textbf{(Eq. 1.2.)}$$

for sources in the objective's lateral (xy) image plane, and:

$$\text{Limit}_{z} = 2\lambda / NA^2 \qquad \textbf{(Eq. 1.3.)}$$

for sources in the objective's axial (z) dimension.

Thus even under optimal conditions (high numerical aperture, high imaging medium refractive index, low imaging wavelength), the finest lateral resolution achievable is ~250 nm, and the finest axial resolution is ~500 nm. Since the molecular and cellular components of neighboring neocortical synapses typically occupy volumes of approximately this size and smaller they cannot be distinguished unambiguously using conventional light microscopy.

Santiago Ramón y Cajal's neuron doctrine (Ramón y Cajal 1995) was based on indirect experiments, since direct observation of the separation between two closely apposed neurons was impossible due to the resolution limits of light microscopy. Indeed, the neuron doctrine received its definitive validation only in the middle of the 20th century, when it was possible to employ transmission electron microscopy (TEM) to observe pre- and post-synaptic elements, as well as the synaptic cleft (Palade and Palay 1954, De Robertis and Bennett 1955).

More recently, an attempt to identify synaptic connectivity between pre-

and post-synaptic neurons in L4 of cat V1 neocortex using bright-field microscopy (da Costa and Martin 2011) resulted in a high (~68%) false positive rate, defined as a contact between the pre- and post-synaptic structures observed in light that did not correspond to a true synapse. Therefore, while light microscopy is well suited to imaging the large (500 x 500 x 500 MICRON) volumes of tissue occupied by whole dendritic arbors in an automated fashion, fundamental resolution limits do not permit unambiguous identification of synapses.

1.2.2. Transmission electron microscopy

Electron microscopy (EM) has been employed for decades to resolve structures that are smaller than the resolution of light microscopy. However, while TEM presents a clear advantage in terms of resolution, it is neither automatable, nor can it be employed to examine large volumes of tissue. Traditionally, visualizing synapses under TEM has required significant manual processing both in preparing the sample and imaging it, that is difficult to scale (**Figure 1.7.**) (Harris, Perry et al. 2006). After staining the tissue with osmium (which binds plasma membranes) it is cut into ultrathin (~70 nm) sections, and depending on the labeling protocol required, often post-stained with heavy metals such as lead citrate and uranyl acetate (which bind proteins, nucleic acids and carbohydrates) to improve contrast and/or highlight structures of interest (Tapia, Kasthuri et al. 2012). A small number of sections is then manually mounted onto a metal grid so that a beam of

accelerated electrons (80–120 kV) can be directed through the tissue. The areas of the sample that contain heavy metals scatter electrons in the beam, which passes through relatively unhindered in the other areas. A detector on the other side of the sample, consisting in a phosphor and a CCD camera, records the resulting image.

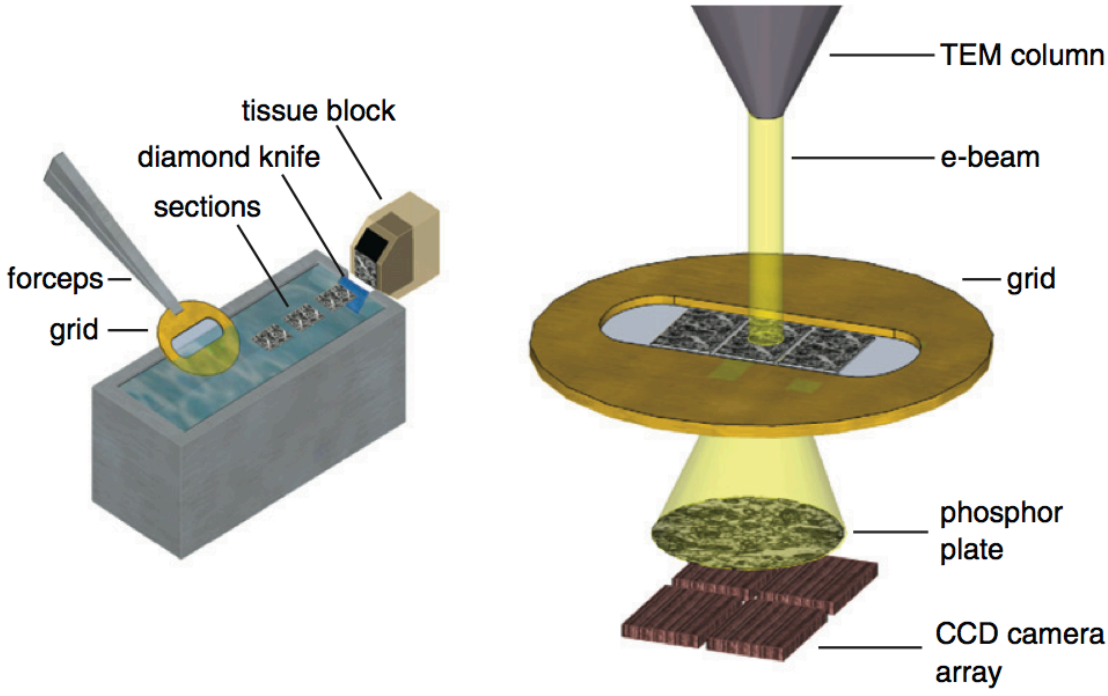

Figure 1.7. *Principle of serial section transmission electron microscopy. Sections are cut and collected manually onto grids using an ultramicrotome (left), and then imaged by shining a high energy electron beam through them (right). Figure from (Briggman and Bock 2012).*

When questions do not require large 3-dimensional volumes of tissue to be imaged under electron microscopy (EM), TEM is a powerful solution. However for volumes spanning even just a few microns in the z axis, imaging serial sections under TEM is problematic. Although a recent heroic effort has produced a large TEM volume (450*350*52 MICRON at <5 nm lateral and <50 nm axial resolution, (Bock, Lee et al. 2011), the skilled manual labor required renders TEM imaging difficult to scale and is prone to inconsistency and error (Briggman and Denk 2006). More problematic for applications that require re-imaging the same area of tissue at different magnification, such as in a multi-resolution strategy, the strength of the electron beam is such that section damage is inevitable over time, compromising axial resolution.

1.2.3. Scanning electron microscopy

To overcome the issue of scaleability in traditional TEM (due to the limitations of manual collection, and the narrow field of view both in the lateral and the axial dimensions), several new approaches have recently been developed to automate the collection and imaging of ultrathin planes of tissue. Most of these strategies employ scanning electron microscopy (SEM) (Briggman and Bock 2012). Instead of shining a beam of electrons through the sample, contrast is generated in SEM by raster-scanning a low energy (1-3 kV) beam across it and detecting back-scattered rather than transmitted electrons (**Figure 1.8.**) (Tapia, Kasthuri et al. 2012). SEM

has far inferior lateral resolution relative to TEM but can distinguish structures in the 1-2 nm range, which is sufficient to clearly resolve the organelles and membranes that form the synapse (Goldstein 2003).

We selected automated tape-collecting ultramicrotome scanning electron microscopy (ATUM-SEM) (Hayworth, Kasthuri et al. 2006, Tapia, Wylie et al. 2012) although several other SEM-based approaches are available (for a review of these, see (Briggman and Bock 2012)). The chief advantage of ATUM-SEM over TEM is that ultrathin tissue sections are cut and collected automatically onto a tape. Since it is relatively immune to inconsistency and human error, the method can be scaled to process significant volumes (100s of microns) without sacrificing axial resolution due to the section damage, loss or inconsistency typical of manual collection for TEM. Unlike other SEM-based approaches (Denk and Horstmann 2004, Heymann, Hayles et al. 2006, Knott, Marchman et al. 2008) ATUM-SEM permits re-imaging the same area at different resolutions. Moreover, because the required energy of the electron beam is significantly lower for SEM relative to TEM, section damage, even after repeated imaging of the same are of the sample, is no longer an issue.

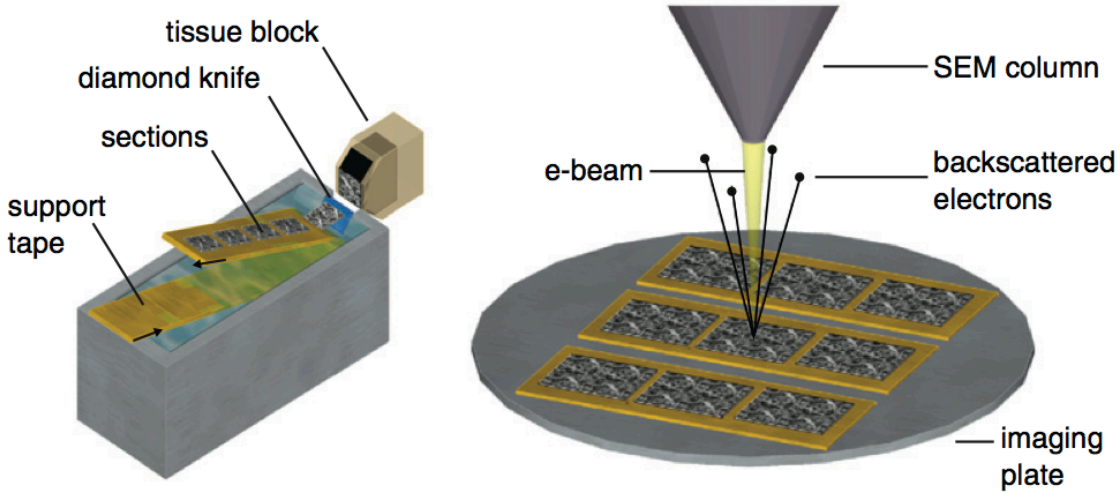

Figure 1.8. *Principle of ATUM-SEM. Sections are cut using an ultramicrotome and collected automatically by a conveyer belt onto a carbon-coated tape (left). They are then mounted onto a silicon wafer, and imaged by shining a relatively low energy electron beam while measuring backscattered electrons. Figure from (Briggman and Bock 2012).*

Theoretically the anatomical component of the work presented here could have been performed entirely using ATUM-SEM. However, automated segmentation and three-dimensional reconstruction of neurites based on image stacks generated by ATUM-SEM and other EM-based strategies, remains an unsolved problem. Thus, while significant progress has been made in speeding up and automating sample preparation and image acquisition, the time required for analysis continue the limit the scalability of all EM-based these methods

(Lichtman and Denk 2011). Short of having a small army of human tracers available to perform the segmentation manually ((Briggman, Helmstaedter et al. 2011); for an interesting 'crowd-sourcing' approach, see https://eyewire.org), there currently exists no practical solution for analyzing EM-acquired volumes of tissue at the scale of the complete dendritic arbor.

1.2.4. Light-based nanoscopy

Recent advances in light-based microscopy have partially circumvented the resolution limits described above, although they remain at the proof-of-principle stage and with few exceptions (Ding, Takasaki et al. 2009, Dani, Huang et al. 2010) have not yet been deployed by laboratories that do not primarily specialize in microscopy.

Three major classes of "nanoscopy" of "sub-diffraction" strategies have been developed: photo-activated localization microscopy (PALM) (Betzig, Patterson et al. 2006, Hess, Girirajan et al. 2006), which is similar in principle to stochastic optical reconstruction microscopy (STORM) (Bates, Huang et al. 2007), structured illumination microscopy (SIM) (Heintzmann, Jovin et al. 2002, Gustafsson 2005), and stimulated emission depletion microscopy (STED) (Hell and Wichmann 1994, Klar, Jakobs et al. 2000). Both PALM/STORM, which are based on stochastically switching small numbers of the sample's fluorophores on and off to calculate their positions, and SIM, in which the sample is excited using structured illumination,

causing detectable Moiré patterns that betray structures at nominally sub-diffraction spatial frequencies, significantly improve lateral resolution (10–30 nm for FPALM/STORM, ~50 nm for SIM) (**Figure 1.9.**). However both of these imaging strategies require wide-field illumination and therefore are not suited for microscopy applications that require tissue penetration. In STED microscopy, a laser-scanning approach, the contours of the excitation laser's PSF are overlapped by a second laser, whose donut-shaped PSF, which is centered on the first one, temporarily quenches fluorescence emission. By eliminating fluorescence in all but the center of the laser excitation spot, the PSF is thus rendered effectively smaller than the optical system's limits. Producing a spherical depletion PSF (Wildanger, Medda et al. 2009) permits axial quenching, and imaging in biological tissue has been achieved at 45 nm lateral, and 108 nm axial, resolution. By contrast with the wide-field-based PALM/STORM and SIM approaches STED uses point illumination, and light emitted from above or below of the plane of focus is eliminated using a confocal pinhole. Thus STED microscopy is in principle better equipped to address questions that require tissue penetration.

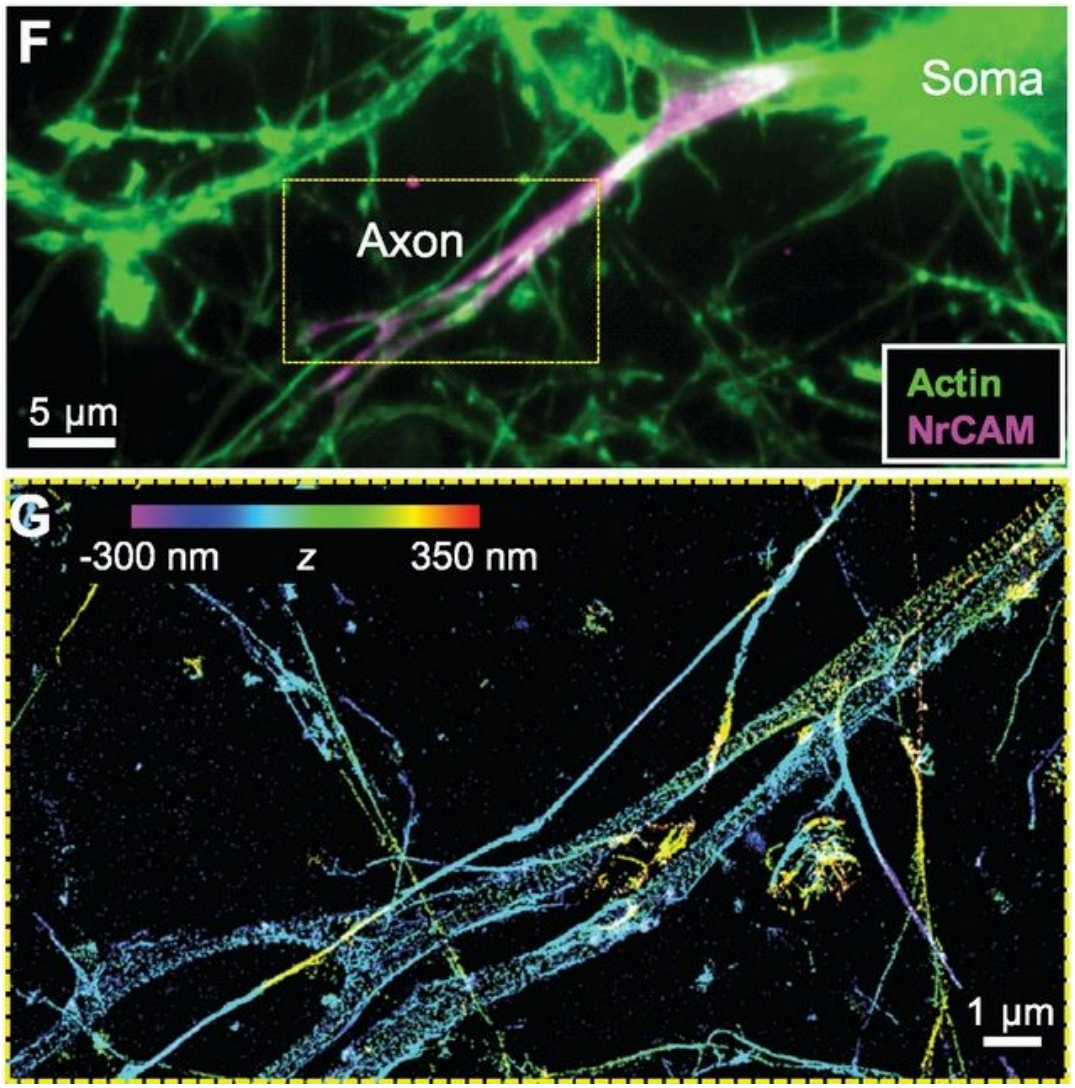

Figure 1.9. *Nanoscopy imaging using STORM reveals subdiffraction structures. Epifluorescence (top) and STORM (bottom) imaging of a segment of the axon of a cultured neuron. The axon initial segment is labeled using an antibody against neuronal cell adhesion molecule (NrCAM) (magenta, top); anti-actin labelling (green, top; and bottom) reveals a highly periodic arrangement that would not be resolvable using conventional light microscopy. Color map in bottom panel corresponds to axial position. Figure from (Xu, Zhong et al. 2013).*

1.2.5. Deconvolved confocal light microscopy

Now a standard tool in neurobiology laboratories, the laser scanning confocal microscope, invented by Marvin Minsky in the middle of the 20th century (Minsky 1961, Minsky 1988, Conchello and Lichtman 2005) but only adopted in its last decade, is also subject to the fundamental limits on traditional light microscopy. It employs point illumination via a raster-scanned excitation laser beam traveling across a focal plane in the sample. A tube lens focuses emitted light emitted from the focal plane through a pinhole approximately the size of the system's PSF; in-plane light is then collected by a photomultiplier tube (PMT). Light emitted from above or below the objective's focal plane is defocused around the pinhole by the tube lens, resulting in relatively little out-of-plane emission light reaching the PMT. In this way, the confocal microscope collects light emitted only from the objective's plane of focus—provided that the tissue is sufficiently clear, and scattering is sufficiently low, to prevent out-of-plane emission light from being erroneously focused onto the pinhole. A precise mechanical or piezoelectric stage manipulator permits acquisition of sequential optical planes of section through the sample, resulting in a three-dimensional stack of two-dimensional images.

Despite the fundamental optical limits described above, it is possible to slightly improve on the effective resolution of confocal microscopy to recover part of the original signal by using deconvolution of the image stack (Van Kempen, Van Vliet et al. 1997, Conchello and Lichtman 2005). The system's PSF, whose

volume is roughly approximated by Abbe's equations (**Eq. 1.2.** and **Eq. 1.3.**), can be measured, using sub-diffraction (< 50 nm) spherical beads of known diameter, or calculated based upon the lens, excitation wavelength and immersion medium properties. The acquired three-dimensional image stack f is a convolution described by:

$$f = s * p + \varepsilon \qquad \textbf{(Eq. 1.4.)}$$

Where s is the actual source, p is the system's PSF and ε is photon noise due to the low number of photons collected from each position in the raster-scan (ε, which exhibits a Poisson distribution, can be decreased by longer spot dwell times, or line- and frame-averaging). Given an estimate of ε, a measured or calculated p, it is possible to solve equation (4) and recover an estimate of s (**Figure 1.10.**).

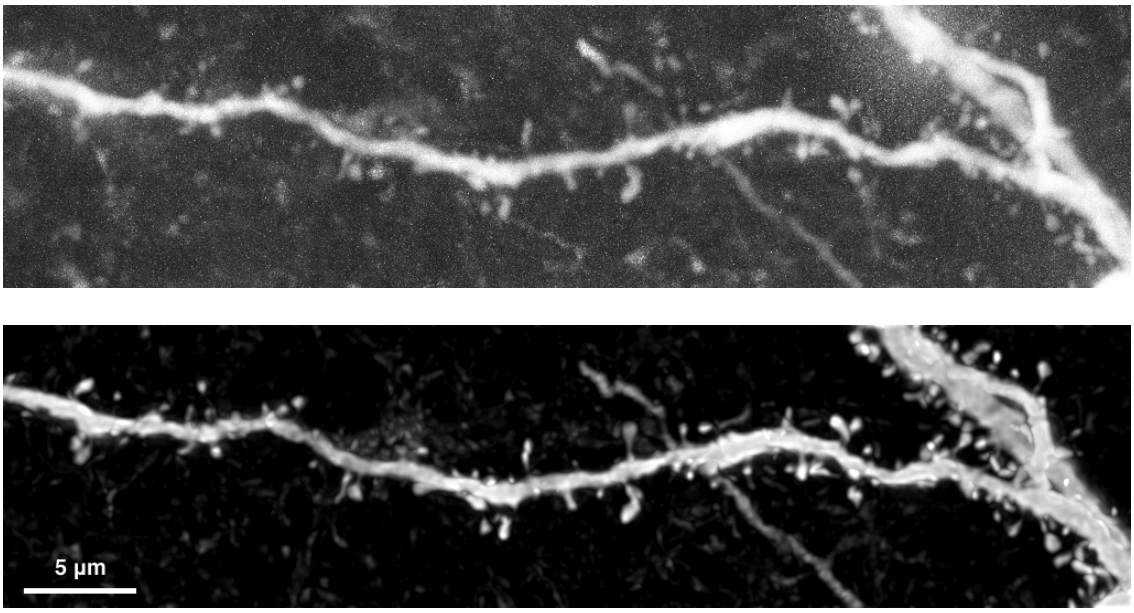

Figure 1.10. *Raw versus deconvolved confocal stack. Maximum z-projection a 237-plane stack obtained using confocal microscopy, showing a biotin-filled dendrite and spines, labeled using streptavidin, before (top) and after (bottom) deconvolution.*

Chapter 2

Synaptic transmission and integration

2.1. Synaptic Transmission

2.1.1. The quantal nature of synaptic transmission

Bernard Katz and colleagues demonstrated the quantal nature of chemical synaptic transmission and provided the basic statistic framework for its analysis. (Del Castillo and Katz 1954, Katz 1969). Under conditions of high extracellular magnesium, which reduces the probability of neurotransmitter release, the magnitudes of stimulus-induced end-plate potentials (EPPs) recorded in the muscle over many trials observe a Poisson distribution. The mean of the distribution of spontaneous EPPs, which reflect postsynaptic depolarizations caused by a single quantum of neurotransmitter, is referred to as the quantal size. It is equal to the mean of the first peak of evoked EPPs; the means of subsequent peaks are multiples of the quantal size (**Figure 2.1.**).

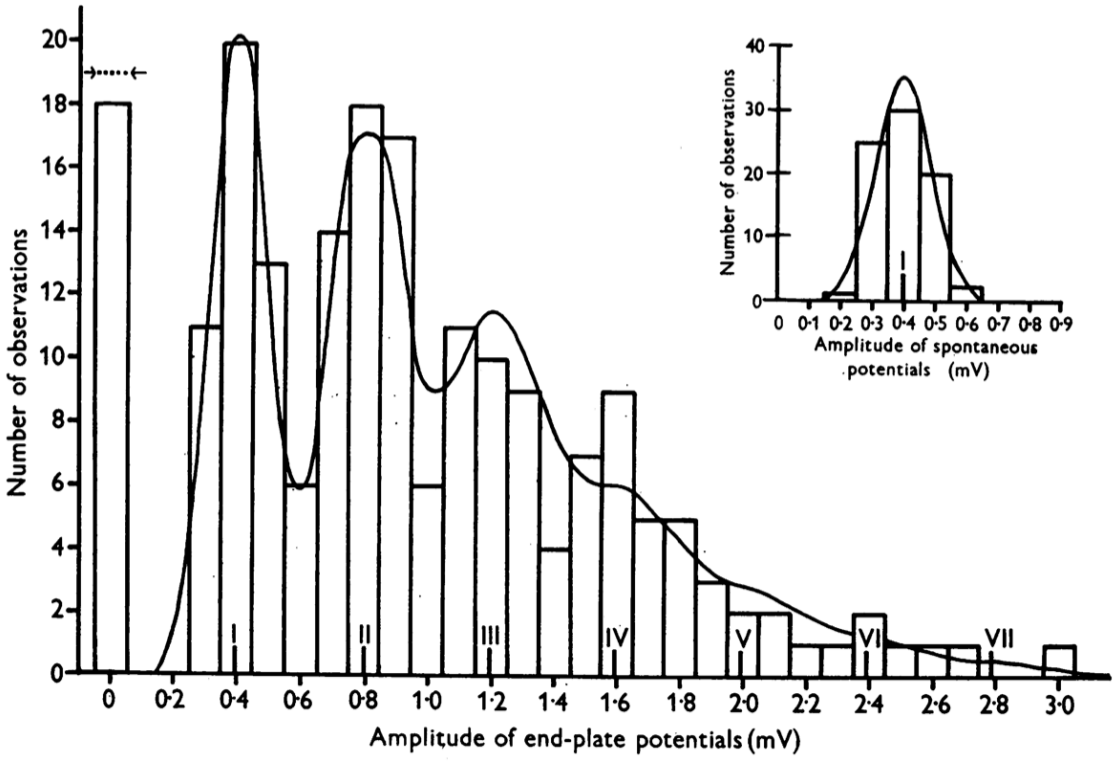

Figure 2.1. *Quantal release of neurotransmitter. Inset: amplitude distribution of spontaneous release events (due to presumably single quanta). Histogram: recorded potentials; line: single-Gaussian fit. Main panel: the amplitudes of EPPs follow a Poisson distribution whose peaks are centered at multiples of the mean of the spontaneous potentials (quantal size). Histogram: recorded potentials; line: seven-Gaussian predicted distribution, in which the means of each Gaussian are multiples of the first mean, which is set to the quantal size. The Gaussians' variances are also multiples of the variance of the spontaneous potentials. Figure from (Boyd and Martin 1956).*

A measure of efficacy, of a given synaptic connection, is given as:

$$e = q \cdot n \cdot p_r \qquad \textbf{(Eq. 2.1.)}$$

Where q is the quantal size, n is the number of independent sites from which neurotransmitter may be released, and p_r is the probability that neurotransmitter release will occur at a release site during an action potential. Note that quantal size is a function of both presynaptic and postsynaptic factors (number of neurotransmitter per quantum, density of postsynaptic receptors and postsynaptic intrinsic membrane properties). Here the term "efficacy" will refer to this simple definition, although theoretical work has proposed a separate meaning, based on information theory, that relates synaptic input to spike output in the presence of background synaptic activity (London, Schreibman et al. 2002).

For a fiber that has multiple independent release sites (either at different synapses, or within the same terminal) the probability p_s of successful transmission, i.e. of observing one or more quantal releases is:

$$p_s = 1 - (1 - p_r)^n \qquad \textbf{(Eq. 2.2.)}$$

where $(1 - p_r)^n$ is probability that all n release sites will fail on a given stimulation.

2.1.2. Short-term plasticity

When a synapse is stimulated by high-frequency pulses, the magnitude of the postsynaptic depolarization typically varies over the course of the pulse train in a phenomenon called short-term synaptic plasticity. This effect is intricately linked

to the quantal nature of synaptic transmission (Zucker and Regehr 2002). Short-term synaptic facilitation, in which a postsynaptic depolarization (or current) is greater than the one that precedes it, is believed to be caused by residual calcium. Normally maintained at very low concentration intracellularly, calcium concentration is transiently elevated following stimulation, and then can affect the mechanism of neurotransmitter release. Short-term synaptic depression, in which a postsynaptic depolarization (or current) is smaller than the preceding one, occurs when the pool of vesicles available for release is depleted by prior release. In addition, post-synaptic mechanisms like receptor desensitization contribute to short-term depression. Both depression and facilitation are thought to affect p_r (the release probability) and/or n (the number of release sites), but not q (the quantal size).

2.2. The integration of synaptic inputs

At first approximation the membrane of a neuron can be modeled as a simple RC circuit, where the resistor (R) represents the resistivity of its membrane, and the capacitor (C) represents its capacitance (**Figure 2.2.**).

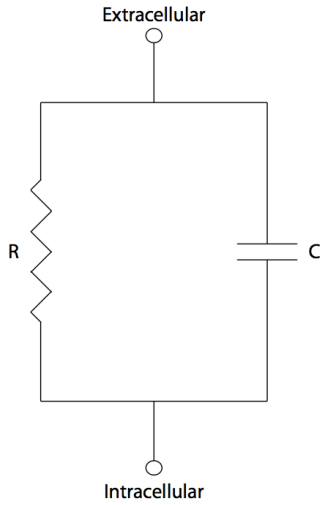

Figure 2.2. *RC circuit representing a neuron's cell membrane.*

2.2.2. Passive dendritic filtering

However, since neurons are not arbitrarily small spheres, but rather exhibit an extraordinarily diverse set of morphologies (Ramón y Cajal 1995), in order to understand how synaptic conductances are integrated and represented at the soma it is necessary to include these morphologies in any account of a neuron's filtering characteristics (**Figure 2.3.**) (Rall 1962). In the absence of conductances that are time and voltage-dependant, that is, when the membrane's properties are strictly passive, they are determined by the morphology of the neuron's processes, its specific resistance (R_m, in Ωcm^2), specific capacitance (C_m, in $\mu F/cm^2$) and the resistance of the cytoplasm, or axial resistance (R_i, in Ωcm). These parameters may

not be uniform across the entire dendritic arbor (Stuart and Spruston 1998). Modeling tools such as NEURON (Hines and Carnevale 1997) permit the researcher to produce compartmental models that take into account both the morphological and the electrical properties of neurons.

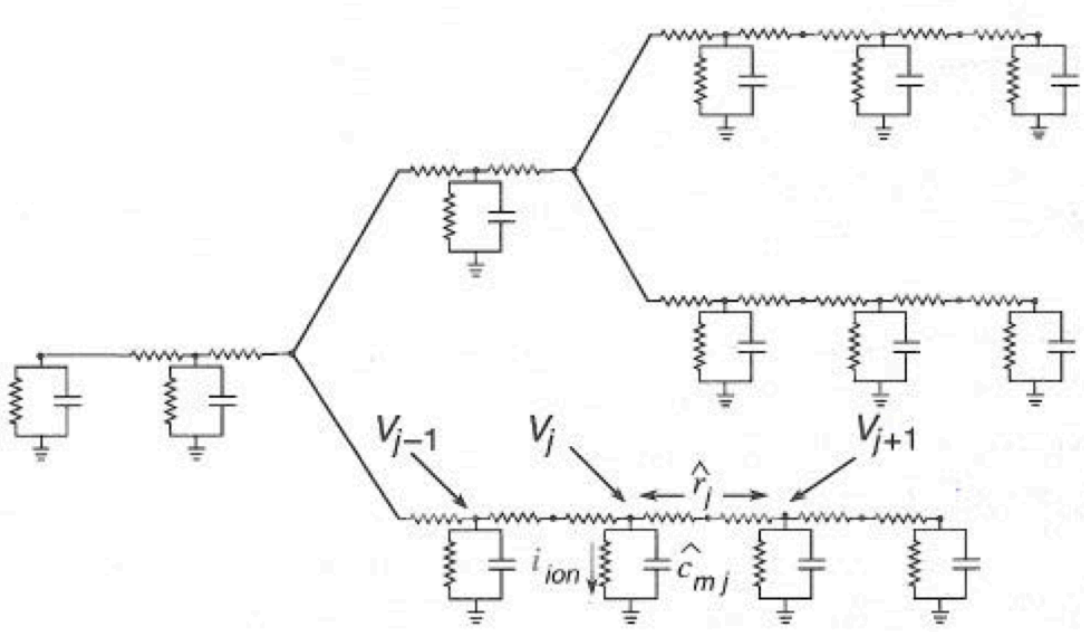

Figure 2.3. *Compartmental model of a dendritic arbor. Segments of the modeled dendrite are partitioned into individual RC circuits, connected to one another by resistors that correspond to the cytoplasmic resistor. Figure from (Stuart, Spruston et al. 1999).*

Since typically the resistance of the membrane is much higher than the resistance of the cytoplasm, most of the current that enters at the synapse flows through the cytoplasm. However, as the current travels towards the soma dendritic filtering typically results in pronounced voltage attenuation, as well as smoothing in the time domain due to the membrane's capacitance (**Figures 2.4.** and **2.5.**) (Rinzel and Rall 1974, Jack, Noble et al. 1975).

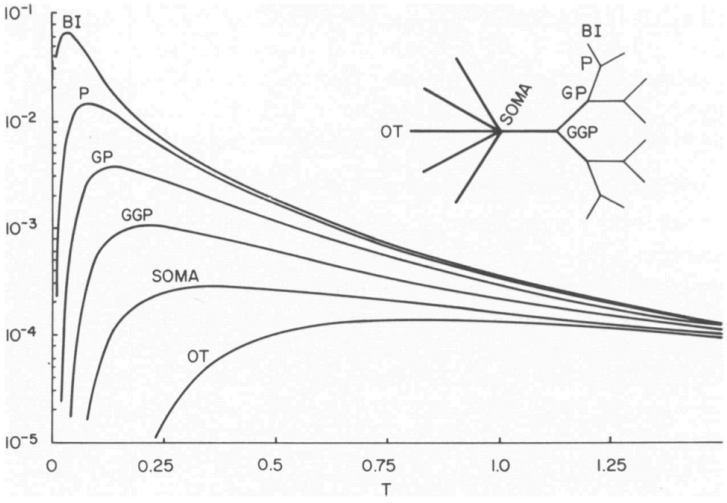

Figure 2.4. *Voltage and temporal attenuation by passive membranes. Inset: representation of the model neuron. Main panel: substantial voltage attenuation (note the log y axis) in response to a brief current injected at BI (input branch), recorded at several nodes of the neuron's dendritic arbor indicated by P (parent), GP (grandparent), and GGP (great grandparent). X axis a dimensionless time variable (seconds over τ), Y axis in log Volts. Figure from (Rinzel and Rall 1974).*

Figure 2.5. *Experimental observation of passive dendritic filtering. Simultaneous recording of dendritic (large-amplitude, 400 μm from the soma) and somatic (small amplitude) voltage response to synaptic stimulation near the dendritic recording site. Note that somatic voltage waveform is not strictly a function of passive membrane properties, as revealed in this same study. Figure from (Stuart and Spruston 1998).*

Voltage attenuation typically increases with distance from the soma, but this is partially counteracted by the local impedance characteristic of distal dendrites (**Figure 2.6.**). First, because they are typically thinner, relatively electrotonically isolated from the soma (which is low-resistance), and relatively close to the dendrite endings, the local input impedance at the distal dendrites can be considerably higher than at the proximal dendrites or the soma, resulting in a larger local excitatory postsynaptic potential (EPSP) for the same amount of current.

However, because the voltage change might be considerable, this exposes distal dendrites to saturation effects as the local voltage approaches the reversal potential for that synapse. (Rall and Rinzel 1973, Rinzel and Rall 1974) Second, as the local input impedance in distal relative to proximal dendrites is high, a greater fraction of current will flow across the cytoplasmic resistor towards the soma, rather than leaked across the membrane.

On the whole, the effect of passive dendritic filtering is greater than the boosting of EPSP as distance from the soma increases, so EPSPs generated distally are smaller, and more temporally attenuated than those generated proximally.

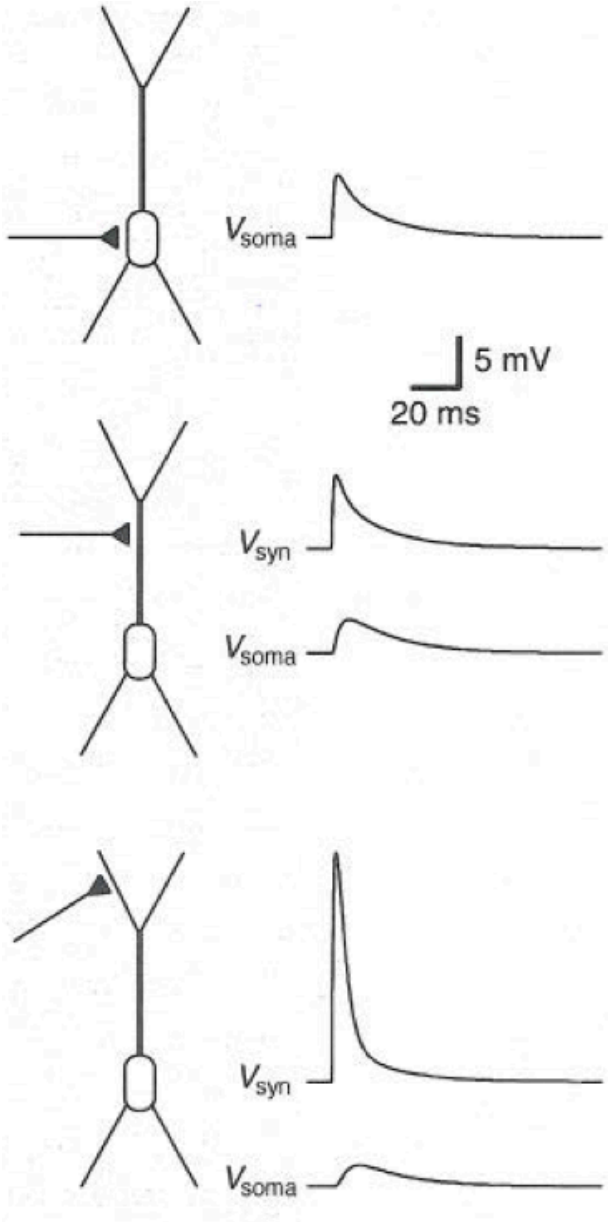

Figure 2.6. *Effect of dendritic location on local and somatic voltage. Left diagrams: location of simulated synaptic conductance along a model neuron's dendritic arbor. Right traces: voltage response recorded at the soma, and locally in the dendrite (bottom two cases). Although more distal inputs are more attenuated than proximal ones, this is partially counteracted by an increasing voltage change in response to the same conductance, as the local impedance increases in distal dendrites. (Note that temporal attenuation is not counteracted by this mechanism.) Figure adapted from (Stuart, Spruston et al. 1999).*

2.2.3. Nonlinear properties of dendrites

Rall hypothesized that to counteract the passive filtering of inputs along the dendritic arbor, an active conductance in the spine head might help to boost them. (Miller, Rall et al. 1985) Indeed, in addition to strictly linear mechanisms that counteract the filtering properties of dendrites, several nonlinear mechanisms have been observed. Voltage-gated sodium channels amplify excitatory inputs generated in the apical dendrites of neocortical layer 5 (L5) pyramidal neurons (Schwindt and Crill 1995); although this amplification is likely to be mediated by somatic and axonal sodium currents (Stuart and Sakmann 1995). In CA1 pyramidal neurons the hyperpolarization-activated current (I_h), which increases as a function of distance from soma, reduces the effect of dendritic location on EPSP kinetics (but not amplitude), normalizing temporal summation (Magee 1999).

Additionally, in CA1 pyramidal neurons, the magnitude of individual synaptic conductance increases with distance from the soma (Magee and Cook 2000). But note that this mechanism might actually counteract itself in the context of elevated presynaptic activity as encountered *in vivo*, due to increased shunting by local synapses in progressively more distal portions of the dendrite (London and Segev 2001); and this scaling is not a common feature of all pyramidal neurons (Williams and Stuart 2002).

Under specific conditions—in particular, spatiotemporal coincidence of synaptic inputs—dramatic regenerative currents produced by NMDARs, voltage-

gated calcium channels, or voltage-gated sodium channels, are observed in dendrites (London and Hausser 2005). These might further counteract the passive filtering of distal inputs, improve the computational power of single neurons, serve as coincidence detectors, or play a role in synaptic plasticity. Despite recent *in vivo* studies of the effect of how these nonlinear dendritic events relate to sensation and behavior (**Figure 2.7.**) (Lavzin, Rapoport et al. 2012, Xu, Harnett et al. 2012), their precise function and relevance in the awake, behaving animal remain unresolved.

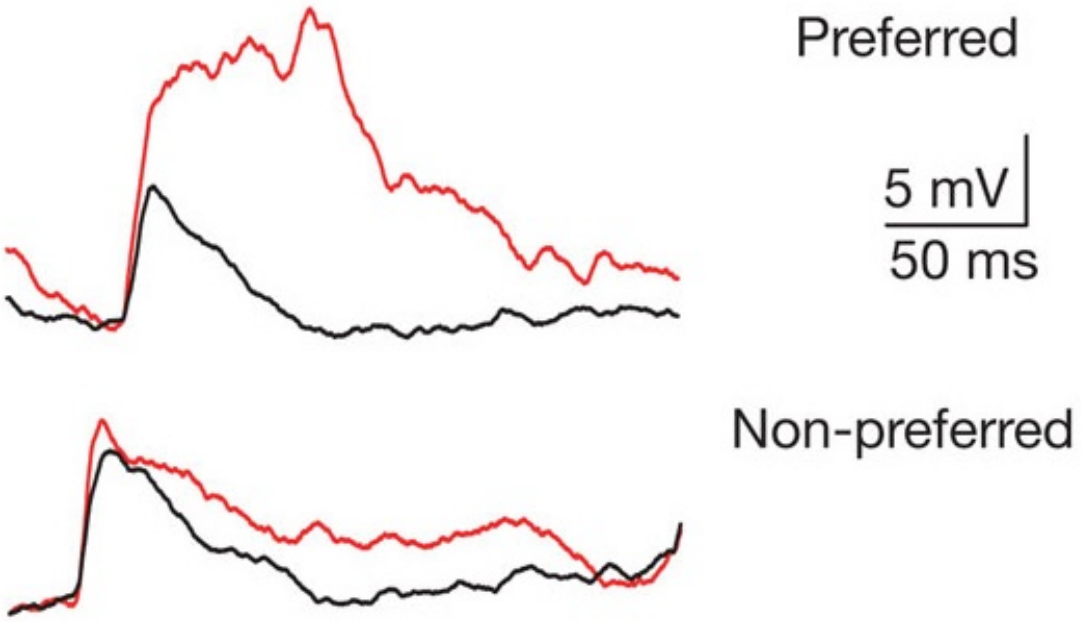

Figure 2.7. *A role for hypothesized NMDA spikes in direction preference.* In vivo *whole-cell current clamp recording of a L4 barrel neuron in response to preferred (top) and non-preferred (bottom) directions of whisker deflection. Red traces correspond to this neuron's response immediately after break-in; black traces were obtained 32 minutes later. The N-methyl-D-aspartate receptor (NMDAR) blocker MK801, included in the pipette had by then had time to diffuse throughout the cell. Hyperpolarizing the neuron using negative current injection to block NMDARs had a similar effect as dialyzing MK801. Figure from (Lavzin, Rapoport et al. 2012).*

2.3. Methods for measuring the strength of a synaptic input

2.3.1. Dual intracellular recordings

In order to obtain measurements of the properties of unitary synapses, it is necessary to relate individual action potentials in a single presynaptic neuron, to their effect on the postsynaptic membrane, such as EPSPs. This is most reliably achieved when simultaneous intracellular access to both the presynaptic and the postsynaptic neurons is achievable. During intracellular recordings of connected pairs of neurons, one can elicit precisely timed action potentials in the presynaptic neuron and simultaneously record their effect postsynaptically, thus obtaining a complete description of the single afferent fiber's effect on its postsynaptic partner.

However, it is often difficult to obtain intracellular recordings of connected pairs of neurons. For experiments performed in acute slices, it is not always possible to design an angle of section that contains both the pre- and post-synaptic populations of neurons, as well as axons connecting the two within the slice. Even when it is, one must assume that that critical axonal and dendritic processes have not been severed by the slice preparation, even if a sufficient number remain to detect connected pairs. (This would cause one to underestimate the number of release sites per fiber, as well as the total synapse strength.) In intact preparations, the yield for obtaining simultaneous, good-quality intracellular recordings is drastically lower, and studies that employ dual intracellular recordings *in vivo* (Okun and Lampl 2008, Gentet, Avermann et al. 2010, Yu and Ferster 2010) are

relatively rare. The situation is further complicated both *in vitro* and *in vivo* if the actual connection probability between the two neuron populations is low (Lefort, Tomm et al. 2009).

2.3.2. Minimal stimulation: principle

"Minimal stimulation" (Raastad, Storm et al. 1992, Stevens and Wang 1995, Gil, Connors et al. 1999) can be employed to circumvent these issues, with the caveat that this method does not permit the same degree of certainty as intracellular recordings of connected pairs. During minimal stimulation, the postsynaptic neuron is recorded intracellularly but the presynaptic fiber is recruited using extracellular stimulation. At low stimulation intensities, the pulse fails to recruit any fibers that form synapses with the postsynaptic cell, and the postsynaptic membrane potential is unaffected (**Figure 2.8.**). (However it may recruit other fibers that do not form synapses onto the postsynaptic cell.) As the stimulation intensity is increased, trials result in all-or-none synaptic events, reflecting whether or not a presynaptic fiber was successfully recruited. For a given stimulation intensity, the probability p_e of observing a postsynaptic event is:

$$p_e = p_s \cdot p_a \qquad \textbf{(Eq. 2.3.)}$$

Where p_s is the synapse's overall success probability (see **Eq. 2.2.**) and p_a is the probability, at that stimulation intensity, of eliciting an action potential in a fiber that forms a synapse onto the postsynaptic cell. To achieve minimal stimulation the

first step is to calibrate the stimulation level such that that $p_e \approx 0.5$. Once this is achieved, the criteria for successful minimal stimulation (based on (Gil, Connors et al. 1999)) are:

(1) all-or-none synaptic events

(2) little or no variation in EPSC/EPSP latencies

(3) a small change in the stimulus intensity did not change the mean size or shape of the EPSC/EPSP

(4) lowering stimulus intensities by 10-20% results in complete failure to evoke EPSCs/EPSPs

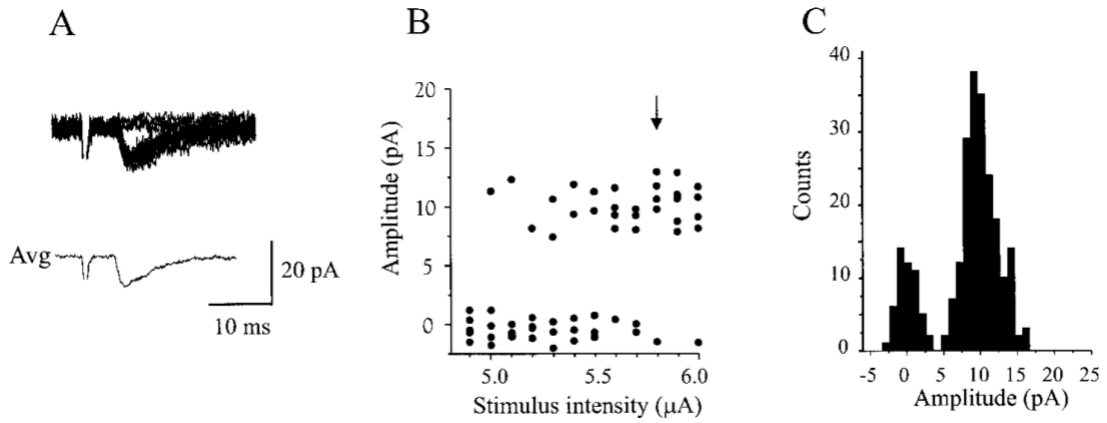

Figure 2.8. *Minimal stimulation results in all-or-none EPSCs. Left panel, top: 50 trials of a L4 neuron recorded in whole-cell voltage clamp during stimulation of TC fibers at a single intensity level, resulting in both successes and failures in transmission. Left panel, bottom: average of those 50 trials. Middle panel: as stimulation intensity increases, the probability of eliciting successful transmission increases without affecting the magnitude of the EPSC. Right panel: amplitude histogram in response to stimulation at the level indicated by the arrow in the middle panel. It appears that this fiber forms only one release site onto the postsynaptic neuron. Figure from (Gil, Connors et al. 1999).*

2.3.3. Minimal stimulation: limitations

Unlike intracellular recordings of connected pairs, minimal stimulation is subject to many potential confounds that cloud interpretation (Stevens and Wang 1995,

Cruikshank, Urabe et al. 2010).

First, in a heterogeneous neuronal population it is often impossible to determine with certainty that the stimulated fiber emanates from a neuron that belongs to the targeted presynaptic population. This issue can be resolved using optogenetic methods: by targeting a light-activated cation channel such as Channelrhodopsin2 to a genetically- and/or anatomically-defined presynaptic population, and adapting minimal stimulation protocols to employ light rather than electrical pulses (Cruikshank, Urabe et al. 2010, Franks, Russo et al. 2011). However, due to the considerable variability, relative to electrical stimulation, in the latency between stimulation onset and action potential onset, the second condition for minimal stimulation (little or no variation in EPSC latencies) is difficult to satisfy (Cruikshank, Urabe et al. 2010).

Second, this method does not randomly sample synapses as it is biased towards synapses with high p_s. Indeed, low p_s synapses might rarely or never release quanta over the course of a limited number of trials.

Third, it is impossible to confirm that only a single connected fiber is recruited by the stimulus, and that the same fiber is recruited on consecutive trials. This proves particularly problematic for fibers that form synapses containing many release sites (high n). In that case, it can be difficult to disambiguate between true single fiber stimulation and multiple fiber stimulation, both of which result in highly variable amplitudes (**Figure 2.9.**).

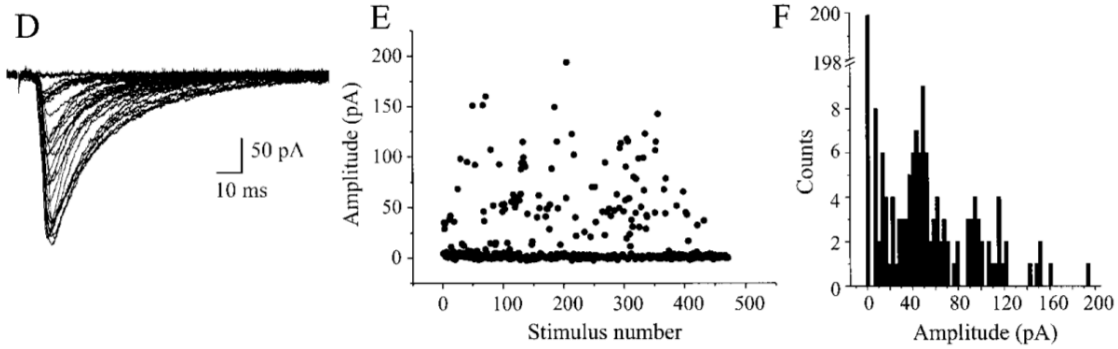

Figure 2.9. *Minimal stimulation of a highly variable fiber. Left panel, top: many trials of a L4 neuron recorded in whole-cell voltage clamp during stimulation of TC fibers at a single intensity level, resulting in failures and successes that are highly variable in amplitude. Middle panel: EPSC amplitude over time. Right panel: amplitude histogram. It appears that this fiber has multiple release sites onto the postsynaptic neuron. However it cannot be ruled out that the highly variable amplitudes of successful transmission are observed because more than one fiber is being recruited at this stimulation level. Figure from (Gil, Connors et al. 1999).*

Therefore, conclusions that rest on minimal stimulation experiments must be considered provisional, pending confirmation from methods that afford better interpretation such as intracellular recordings of connected pairs. In some cases (Stratford, Tarczy-Hornoch et al. 1996), side-by-side experiments using these two

approaches have validated measurements that depend on minimal stimulation; but validation for one class of synapses is not generalizable to others given the wide variety of synaptic properties observed in the nervous system.

2.4. The relative efficacy of thalamocortical and corticocortical inputs onto L4 barrel excitatory neurons

Activity in thalamus strongly excites neurons in primary sensory neocortex (Reid and Alonso 1995, Ferster, Chung et al. 1996, Brecht and Sakmann 2002, Wehr and Zador 2003) even though, as outlined above, thalamic terminals comprise only a small minority of synapses onto cortical neurons (Benshalom and White 1986, Peters and Payne 1993). A long-standing hypothesis is that thalamus succeeds in driving cortex because thalamocortical (TC) synapses are significantly stronger than corticocortical (CC) synapses.

When measured in acute neocortical slices, unitary TC synaptic connections onto neurons in thalamorecipient layers of primary sensory cortical areas are significantly stronger, and exhibit more short-term depression, than unitary CC connections (**Figure 2.10.**)--properties that have been observed across multiple species and sensory modalities (Stratford, Tarczy-Hornoch et al. 1996, Gil, Connors et al. 1999, Richardson, Blundon et al. 2009). Similarly, in the anterior piriform cortex, which receives its input from the sensory epithelium via the

olfactory bulb rather than the thalamus, local excitatory CC inputs are far weaker than inputs from bulb (Franks and Isaacson 2006, Franks, Russo et al. 2011).

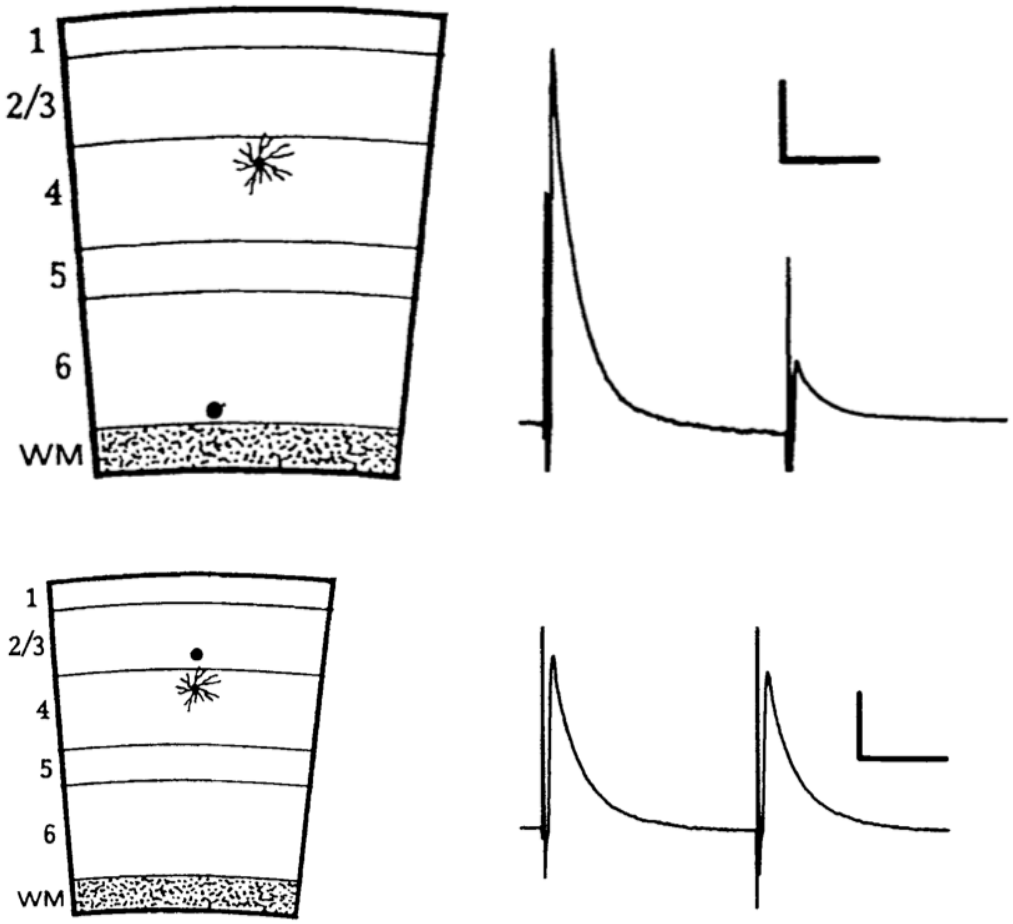

Figure 2.10. *Minimal stimulation of TC and CC fibers* in vitro. *Electrode placement (diagrams in left column, black dot) for TC (top) and CC (bottom) inputs result in different synaptic properties. Whole-cell current clamp recordings (right column) reveal strong, highly depressing TC synapses, and relatively weaker and less depressing CC synapses. Traces are averages of 1,650 (TC) and 800 (CC)*

trials. Scale bars: 20 ms and 300 μV (TC) / 400 μV (CC). Figure adapted from (Stratford, Tarczy-Hornoch et al. 1996).

2.4.1. Proposed mechanism for strong TC inputs (I): synaptic properties

Several factors have been proposed to explain the relative strength of TC synapses. Although quantal size (q) is the same for both classes of inputs, TC fibers are believed to have more release sites (estimated by dividing the average putative unitary fiber EPSC strengths by the estimated quantal size), and higher release probability (inferred from short-term plasticity exhibited during high-frequency stimulation, and by measuring relative decay rates in N-methyl-D-aspartate receptor (NMDAR)-mediated EPSC strength during repetitive stimulation in the presence of NMDAR antagonist MK-801) (Gil, Connors et al. 1999).

However, these quantities are difficult to measure without unambiguous control of presynaptic action potentials; although intracellular paired recordings of cortical neurons are relatively routine (Feldmeyer, Egger et al. 1999), intracellular paired recordings of a VPM and a cortical neuron have not yet been reported. Therefore these conclusions must remain provisional since they rest on results obtained using extracellular electrode stimulation to recruit TC pathways, and isolate putative single fibers. It is possible neither to determine the identity of those

fibers with certainty (although published protocols that employ optogenetics (Cruikshank Connors 2010 Neuron) could now be employed to address this issue and repeat the release probability experiments), nor to confirm that the average unitary fiber EPSC strength truly reflects the action of single fiber.

2.4.2. Proposed mechanism for strong TC inputs (II): passive membrane properties

Recent physiological studies have suggested that TC synapses may be located more proximally to the soma than CC synapses and consequently are less filtered by the passive membrane properties of the dendrites (**Figure 2.11.**). In addition, these TC synapses may form preferentially onto morphological classes of dendritic spines that produce stronger depolarization at the soma when activated (Richardson, Blundon et al. 2009).

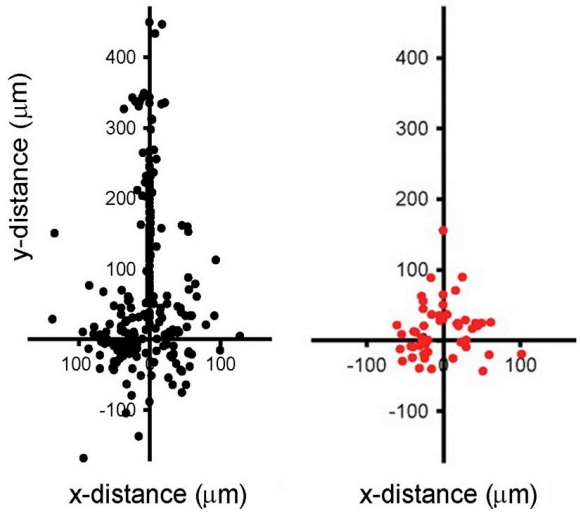

Figure 2.11. *Distribution of TC and CC inputs in thalamorecipient neurons of auditory cortex. Left: composited spatial locations of the 272 CC inputs on 87 thalamorecipient neurons, detected using 2-photon calcium imaging of their spines during electrical stimulation of CC fibers. Right: composited spatial locations of the 46 detected TC inputs on 31 thalamorecipient neurons. 0 represents the soma. Figure adapted from (Richardson, Blundon et al. 2009).*

2.4.3. Proposed mechanism for strong TC inputs (III): circuit dynamics

An alternative hypothesis for how the thalamus drives cortical activity does not require that TC synapses be significantly stronger than CC synapses. Pronounced

cortical excitation could simply be achieved by a suitable pattern of population activity in the thalamus (to be discussed in more detail in **Chapter 5**).

A recent estimate the strength of TC synapses *in vivo* (Bruno and Sakmann 2006) has found that they are considerably weaker than when measured in acute slices, opening the possibility that TC and CC input strengths in the intact animal may not be as distinguishable as when they are measured *in vitro*. However these previous experiments required averaging post-synaptic membrane potential under conditions of elevated thalamic firing rates induced by sensory stimulation, potentially limiting measurement to partially depressed TC synapses. And a direct, side-by-side comparison of TC and CC input strengths *in vivo* has not yet been reported. Therefore, it remains an open question whether the thalamus exerts its strong influence on cortical activity because of the relative strength of its synapses or because of the pattern of the thalamic network's activity.

2.5. Strategy

Here we set out to resolve this issue, testing whether thalamic synapses differ from cortical synapses, either in their anatomical configuration or in their physiological strength. This study characterizes and compares the detailed anatomy and physiology of rat L4 barrel TC and CC synapses *in vivo*, where pre- and post-synaptic structures are fully intact. We present a fast, reliable, high-throughput light microscopy method to construct a complete map of the TC synapses onto the

dendritic arbor of individual cortical neurons. This comprehensive mapping approach demonstrates a slight proximal bias of TC synapses relative to CC synapses. Compartmental modeling predicts, however, that this bias is insufficient to significantly enhance TC strength. By adapting *in vitro* minimal stimulation protocols for use in the living animal, we measure the strengths of TC and CC synapses in a manner that eliminates the potential confound of synaptic depression due to sustained thalamic activity during whisker stimulation. We find that the strengths of TC and CC synapses are both weak, and similar to each other, suggesting that previous comparisons of TC and CC inputs *in vitro* did not accurately reflect their relative strengths *in vivo*.

Since differences in synaptic strength cannot alone explain how the thalamus drives the neocortex, we conclude that this is achieved by the thalamic network's pattern of activity.

Chapter 3

Reliable mapping of dendritic trees using light microscopy

3.1. Identification of putative synapses by light microscopy

3.1.1. Labeling pre- and postsynaptic structures

Excitatory L4 barrel neurons receive excitatory inputs from primary but not secondary thalamic nucleus (Wimmer, Bruno et al. 2010), and cortical inputs primarily from other L4 cells and a small fraction of L6 cells (McGuire, Hornung et al. 1984, Ahmed, Anderson et al. 1994, Stratford, Tarczy-Hornoch et al. 1996). To map the distribution of cortical and thalamic synapses onto L4 neurons, we identified pre- and post-synaptic structures by selectively labeling the synaptic terminals of ventral posteromedial nucleus of thalamus (VPM) (**Figure 3.1.**) and the dendrites of single excitatory neurons in L4 of somatosensory cortex (**Figure 3.2.,** red). Cortical neurons were juxtasomally labeled with biocytin. We employed

two different approaches to labeling thalamic axon terminals. In one approach we expressed a synaptophysin-EGFP fusion protein encoded by an adeno-associated virus injected into VPM (85-95% infection efficiency).

Alternatively we labeled TC terminals by immunostaining against the Vesicular Glutamate Transporter 2 (VGluT2), which labels thalamic but not cortical terminals in L4 (Fujiyama, Furuta et al. 2001, Graziano, Liu et al. 2008, Coleman, Nahmani et al. 2010) (and see Methods). Under both approaches, the clustering of thalamic axons into discrete barrels was clear in tangential sections of somatosensory cortex (**Figure 3.2.**, green), and synaptic staining was sparse and punctate under high-magnification (**Figure 3.4.**. green).

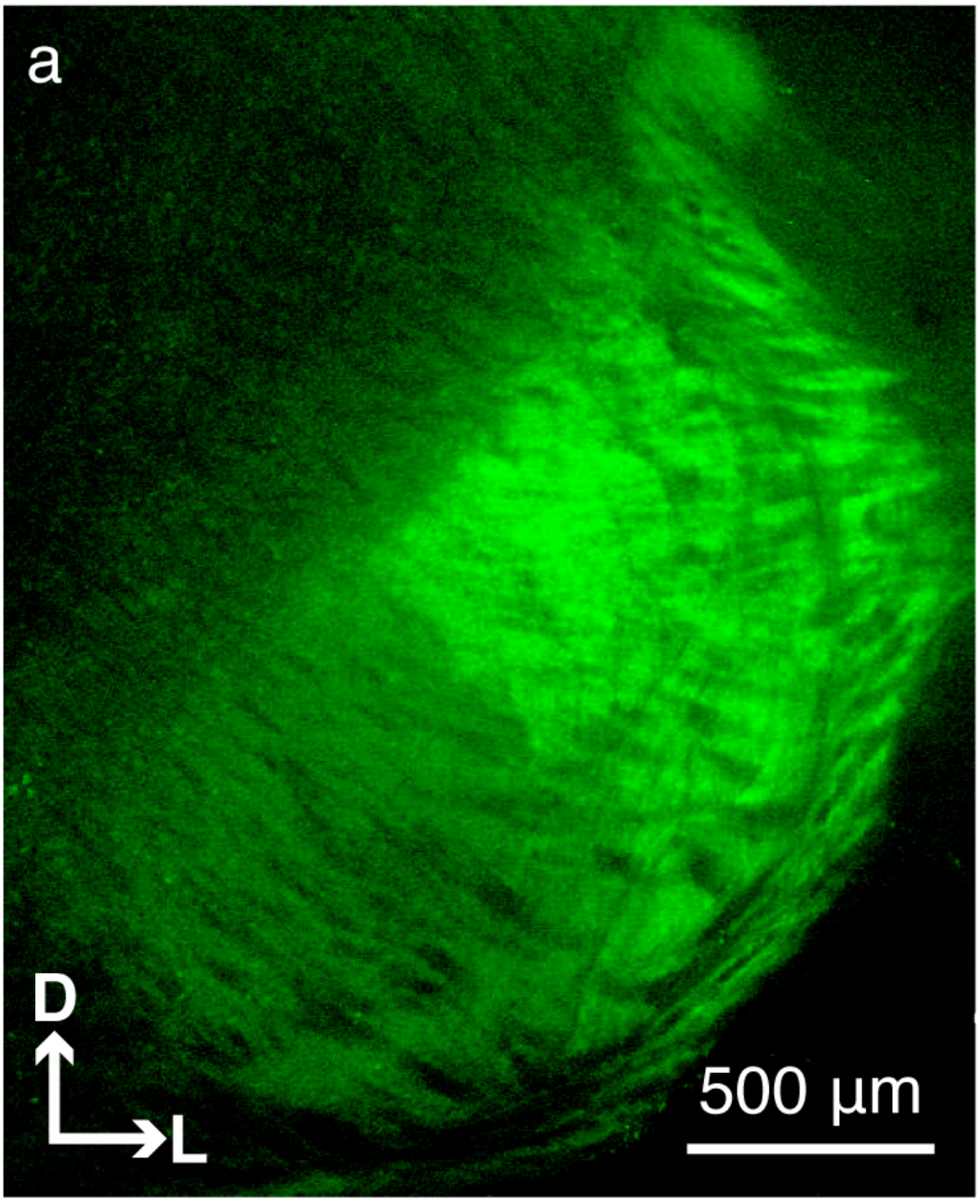

Figure 3.1. *Expression of synaptophysin-EGFP in VPM after AAV injection. Virus was allowed to express for ~5 months. Injections typically infected 85-95% of thalamic neurons*

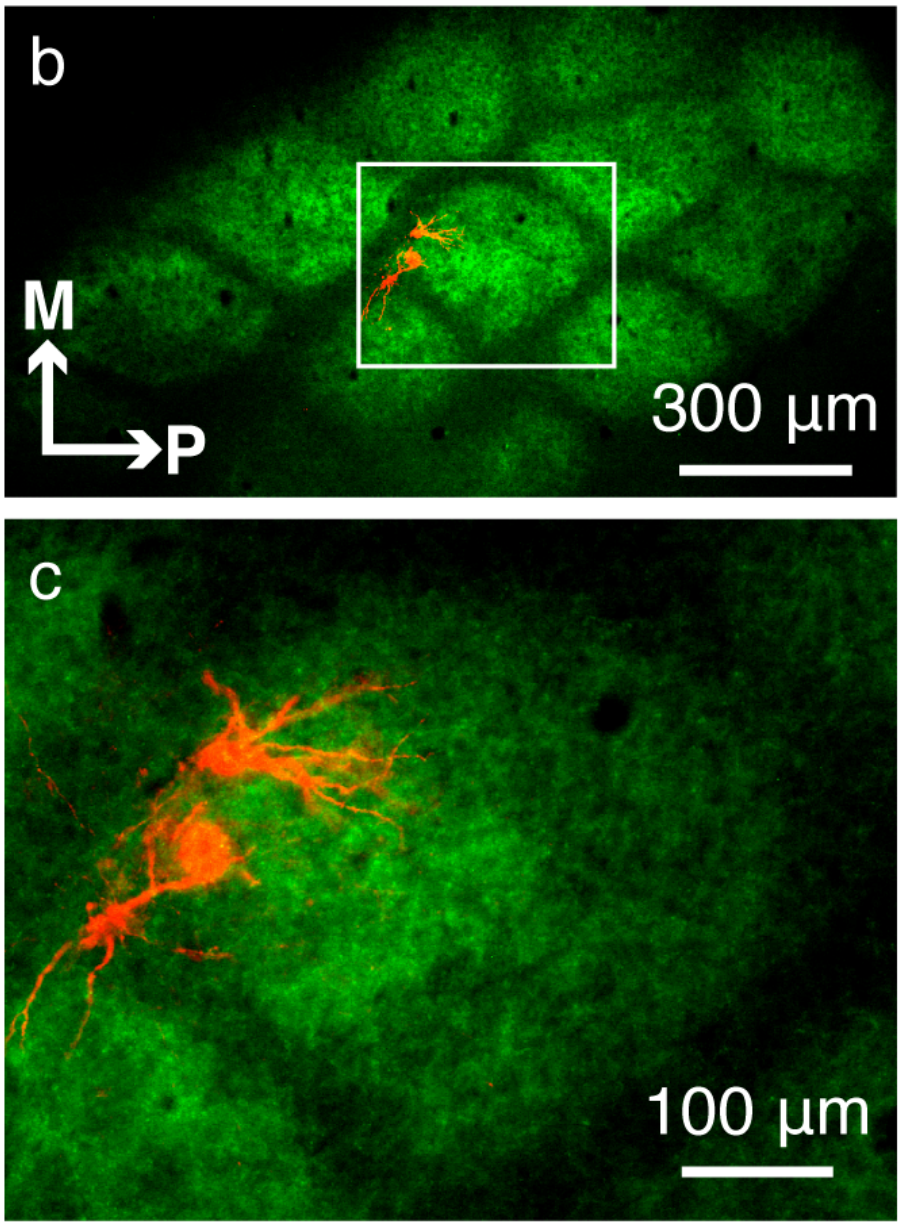

Figure 3.2. *Overview of pre- and post-synaptic. Two excitatory neurons in L4 of somatosensory cortex juxtasomally-filled with biocytin visualized under epifluorescence microscopy. Red: cells stained with streptavidin-conjugated Alexa594; green: synaptophysin-EGFP. Bottom: higher-magnification view of the region outlined in the top panel*

3.1.2. Constructing synaptic maps of complete dendritic arbors

To comprehensively map synaptic contacts onto the cortical neuron, it was essential to reconstruct the neuron's entire dendritic arbor. To do this we employed high-magnification confocal microscopy and deconvolution (see Methods), acquiring image stacks of dendritic arbors of filled neurons. We could then visualize these stacks with sufficient X, Y and Z resolution to clearly distinguish dendritic spines (**Figure. 3.3.**).

We established the following criteria to distinguish TC from CC synapses: those spines that directly apposed, or overlapped with, a VGluT2+ thalamic terminal were classified as TC (**Figure. 3.4.**: synaptophysin-EGFP, except for bottom right panel which is VGluT2). Those spines that did not appose a labeled terminal were classified as receiving CC inputs. This method allowed us to map putative excitatory synaptic inputs across the entire dendritic tree using light microscopy.

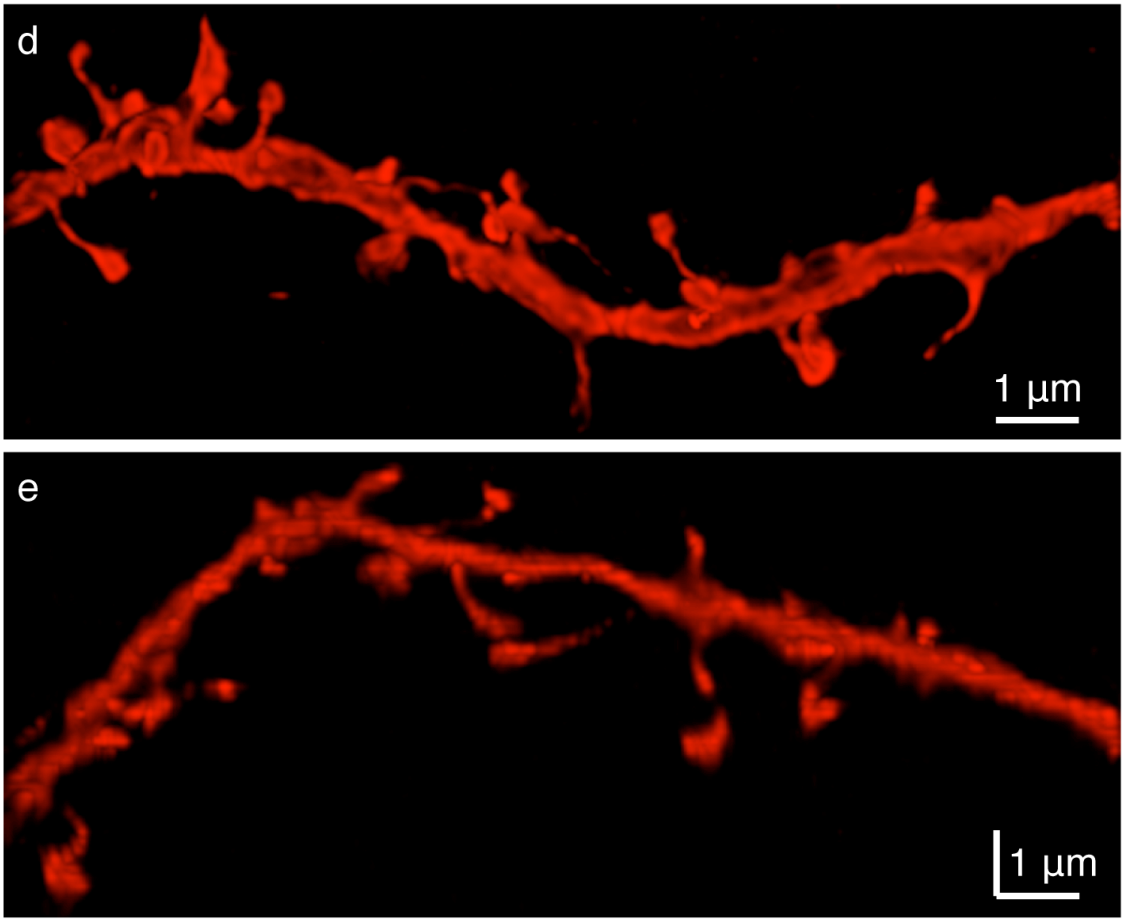

Figure 3.3. *High-resolution lateral and axial resolution with confocal microscopy. Top: z-projection of dendritic segment after confocal imaging and deconvolution demonstrates adequate x and y resolution to distinguish spine heads and spine necks.* ***.*** *Bottom: y-projection of same image stack shows that z resolution is also adequate.*

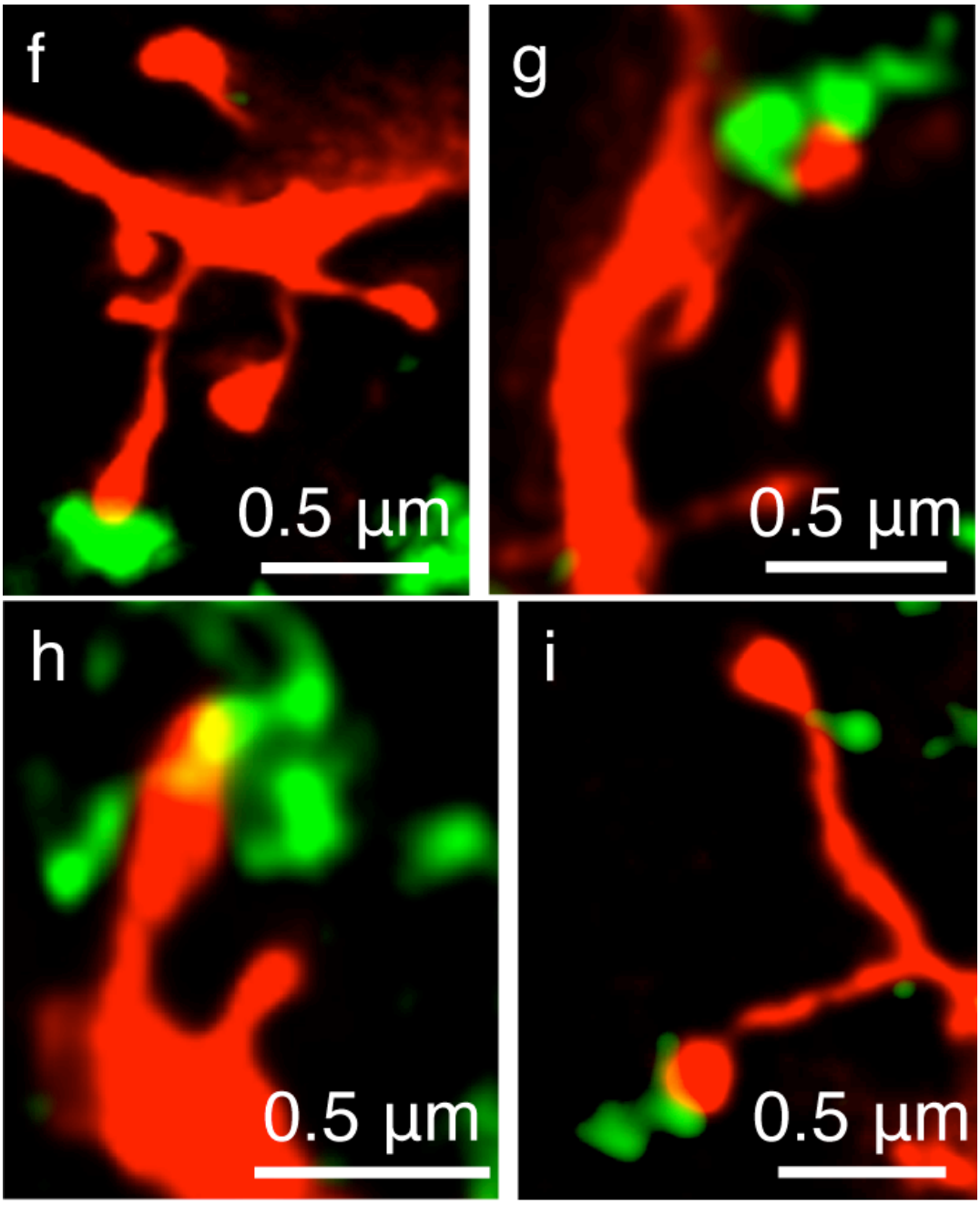

Figure 3.4. *Putative TC contacts under confocal microscopy. Examples of a subset of spines apposed to markers for presynaptic vesicle pools in TC boutons. Green: synaptophysin-EGFP except for bottom-right panel, in which it represents anti-VGluT2.*

3.2. Most putative contacts are true synapses at the EM level

The spatial resolution of light microscopy, even at high resolution and deconvolved, is potentially too coarse to detect true synapses. To check its reliability we developed a correlative light (LM) and electron microscopy (EM) strategy to determine the fraction of those TC contacts predicted by LM that are true synapses at the ultrastructural level.

3.2.1. Correlative LM/EM method

In order to maximize the contrast of the electron-dense stain while still retaining sufficient ultrastructure to reveal post-synaptic densities (PSDs) and vesicle pools, we designed our staining strategy such that the staining intensities of the pre- and post-synaptic structures could be calibrated independently of one another, without masking relevant intracellular structures. (See appendix) The biocytin-filled dendrite was incubated with an Alexa-nanogold-streptavidin triple-conjugate, ensuring that a fluorescent molecule detectable with LM would yield a corresponding EM signal, after silver enhancement of its conjugated gold particle. To label VGluT2+ thalamic neuron terminals across both imaging modes, we simultaneously reacted two secondary antibodies against the anti-VGluT2 primary—one conjugated to a fluorophore, and the other conjugated to horseradish peroxidase (HRP).

After imaging both dendrite and thalamic terminals under high-magnification confocal microscopy we deconvolved the image stacks and scored spines as putative TC or CC as above. We then reacted the tissue to render those same structures electron-dense (silver enhancement of nanogold particles for dendrites; DAB polymerization for VGluT2+ vesicle pools) and prepared the tissue for visualization under EM, which resulted in shrinkage of the cellular structures. We examined dendritic segments chosen at random throughout the neuron's arbor, reconstructing them from ultrathin 70-nm serial sections and registering individual spines across both imaging modes (**Figure. 3.5.**).

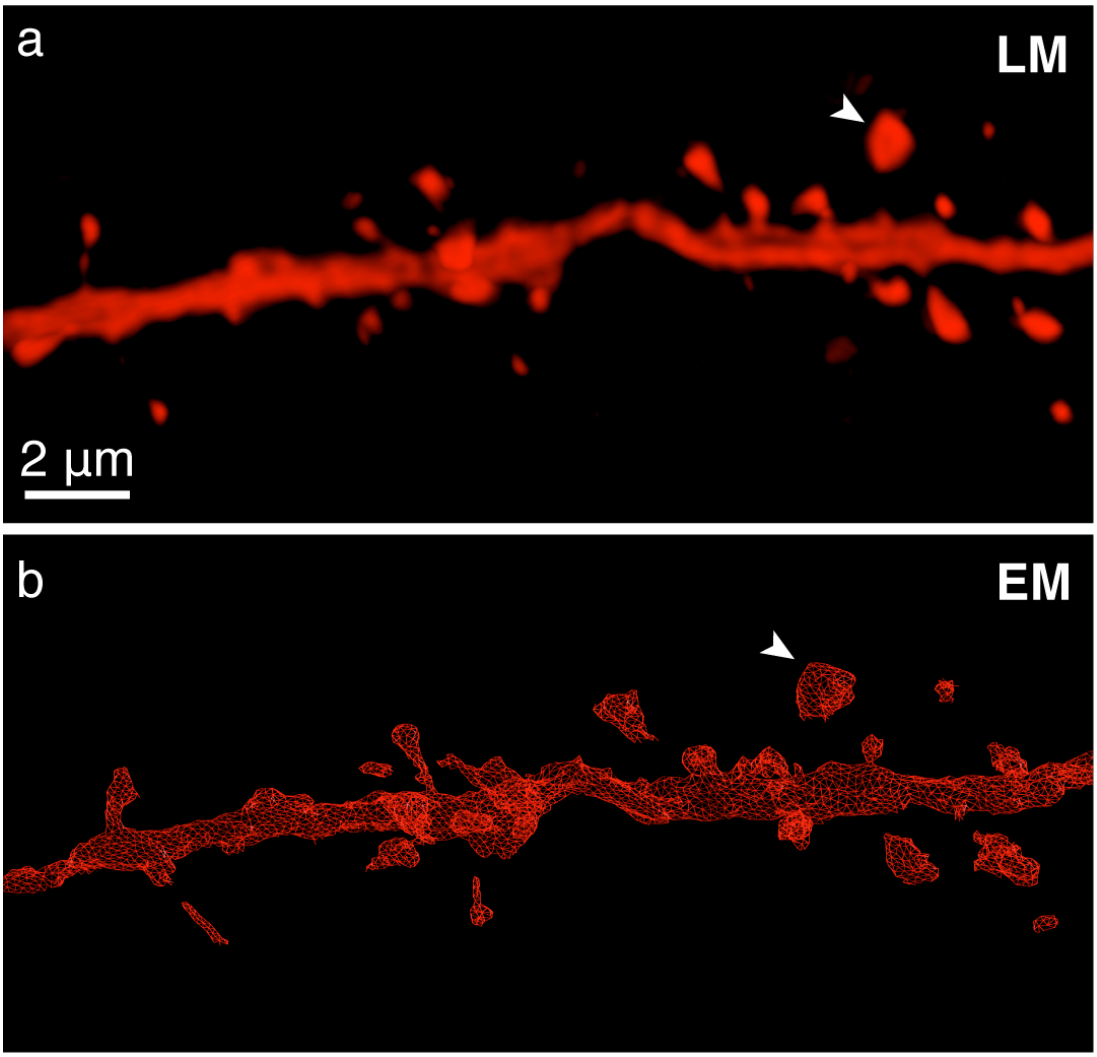

Figure 3.5. *Registration of dendritic spines across LM and EM. The same spines are examined both in confocal microscopy stacks (top) and in subsequent reconstructions of 70-nm serial sections imaged by SEM (bottom).*

3.2.2. Examining synapses under LM and EM

EM visualization revealed filled dendrites with a punctate staining pattern throughout the dendritic shaft, spine heads and spine necks, but absent within mitochondria (**Figure. 3.6.**).

After registering individual spines across LM and EM imaging modes, spines classified as TC in LM were then re-imaged at higher magnification under EM to determine whether the requisite ultrastructural features were present to confirm that they were indeed true TC synapses. DAB polymerization by HRP resulted in a subset of boutons with intensified VGluT2+, and unintensified VGluT2-, vesicle pools (**Figure. 3.7.**, green arrowhead: VGluT2+, blue arrowhead: VGluT2-). Owing to the punctate, rather than diffuse, nature of this staining method, PSDs were clearly visible (**Figure. 3.7.**, red arrowhead).

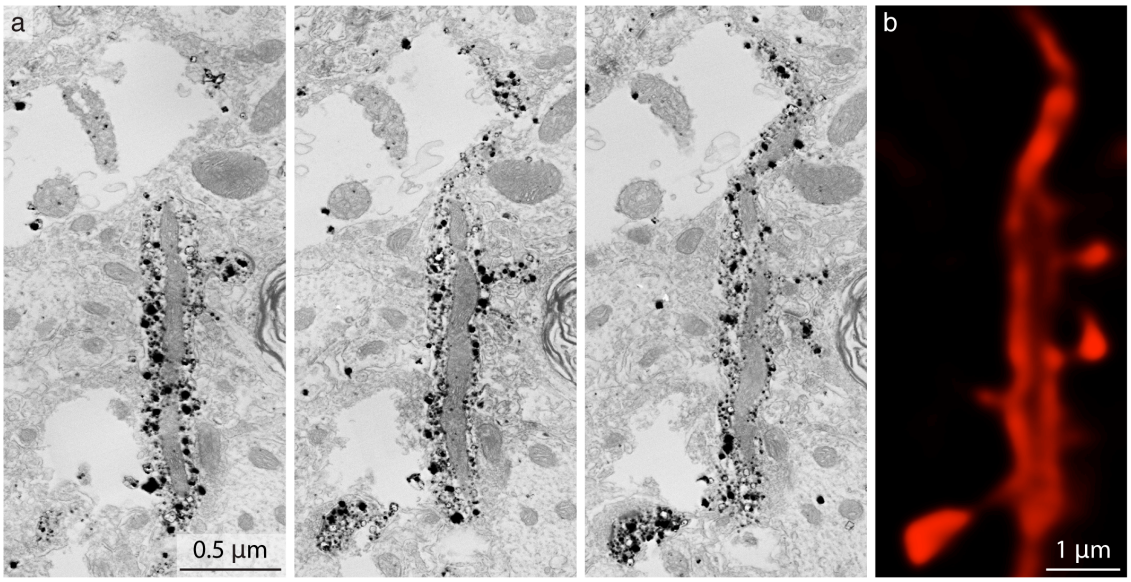

Figure 3.6. *Registration of dendrite segments across LM and EM. Three left panels: SEM photomicrographs of three consecutive 70 nm ultrathin sections obtained at low magnification (12 nm / pixel) reveal a punctate staining of the filled dendrite, resulting from silver-enhancement of the Alexa-nanogold-streptavidin triple-conjugate. The dendrite shaft, spine heads, and spine necks are clearly labeled, but a large mitochondrion remains unlabeled, implying the biotin did not penetrate this organelle during the neuron's filling. Right panel: a single LM plane (theoretical optical section thickness = 136.4 nm) approximately corresponding to this same area of dendrite. Deconvolution permits distinction between the dendrite's biotin-filled cytoplasm and its unfilled mitochondrion. This photomicrograph is an X, Y, Z subset of the dendrite shown in* ***Figure 3.5.****.*

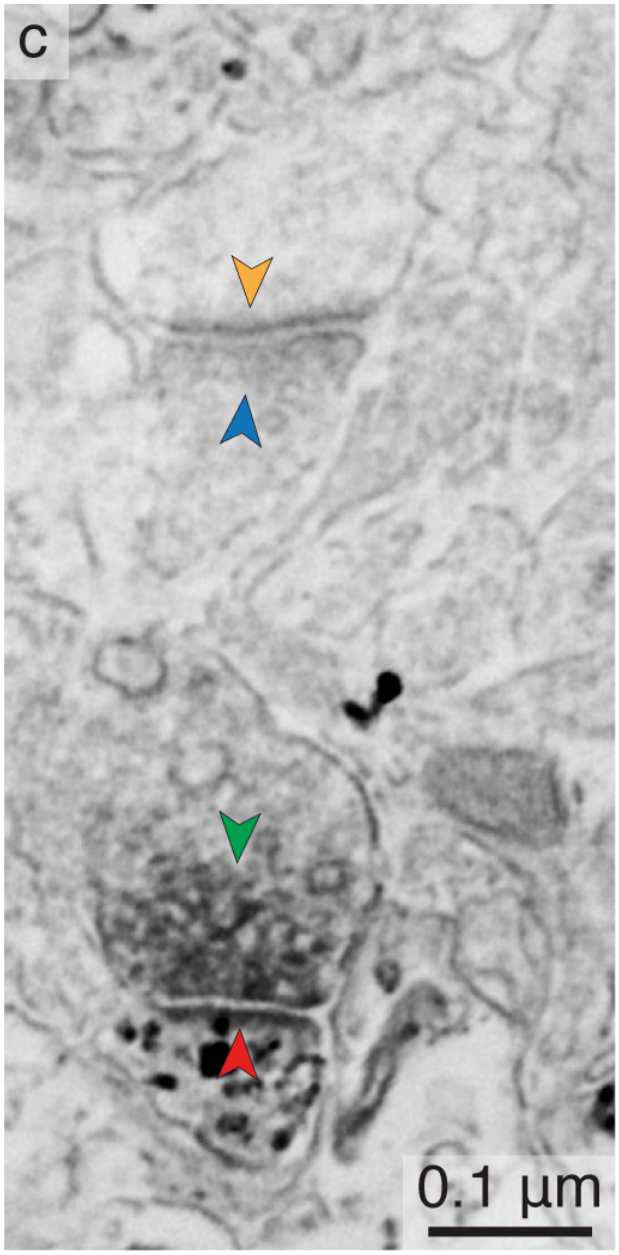

Figure 3.7. *Distinguishing labeling and unlabelled synaptic structures. High magnification (2 nm / pixel) SEM photomicrograph showing a DAB-labeled VGluT2+ vesicle pool (green arrowhead, dark grey diffuse stain) apposed to a silver-enhanced nanogold-labeled spine (black punctate stain) containing a PSD (red arrowhead); this contrasts with an unlabeled VGluT2- vesicle pool (blue arrowhead apposed to an unlabeled spine containing a PSD (yellow arrowhead). This photomicrograph shows a larger field of view surrounding the spine/vesicle pool shown in* ***Fig. 3.8, middle panels.***

3.2.3. Reliability of the LM mapping method

True positives were defined as putative TC spines in LM, whose PSDs, when visualized in EM, were apposed to a VGluT2+ vesicle pool (**Figure 3.8.**).

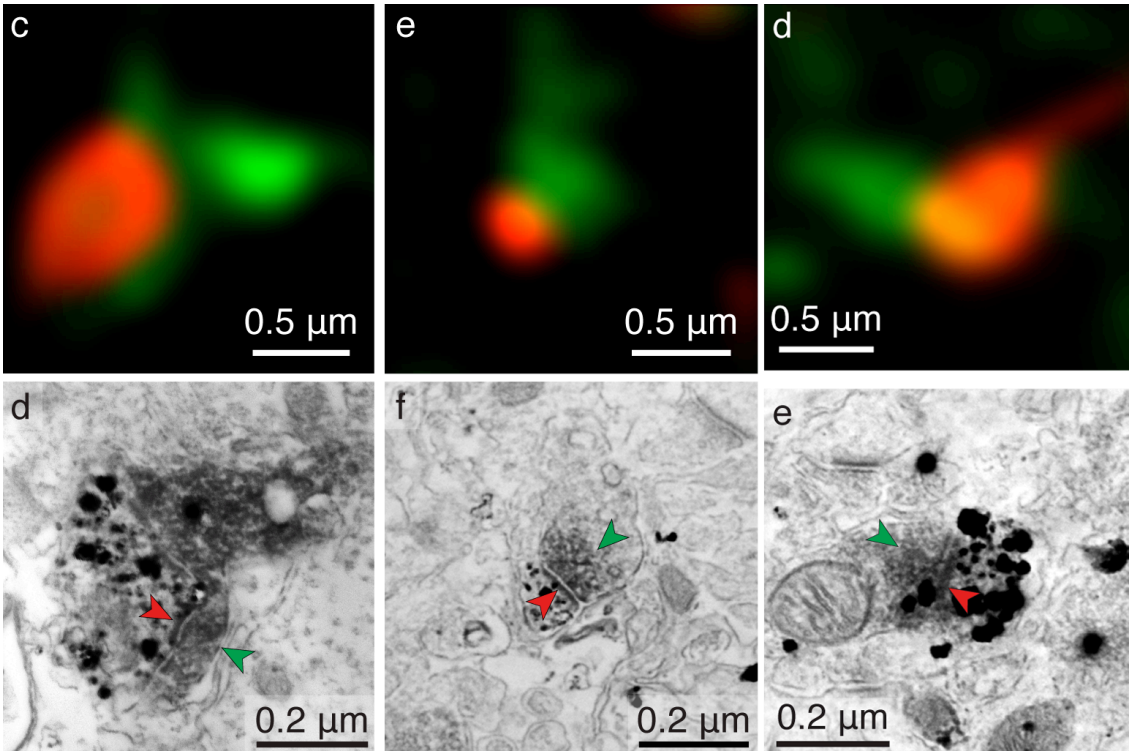

Figure 3.8. *Three examples of confirmed TC contacts. Under confocal microscopy (top row), the spine (red fluorescence) apposes a VGluT2+ vesicle pool (green fluorescence). The corresponding ultrastructure (bottom row) reveals the spine (black punctate stain), its PSD (red arrowheads) apposed to a VGluT2+ vesicle pool (dark grey diffuse stain, green arrowheads). (The left panels show the spine indicated by the arrowhead in* ***Fig. 3.5****. The other panels correspond to spines located in a different area of the same dendrite, not shown in* ***Fig. 3.5****.)*

False positives were defined as putative TC spines in LM, whose PSDs, when visualized in EM, were not apposed to a nearby VGluT2+ vesicle pool (**Figure 3.9.**).

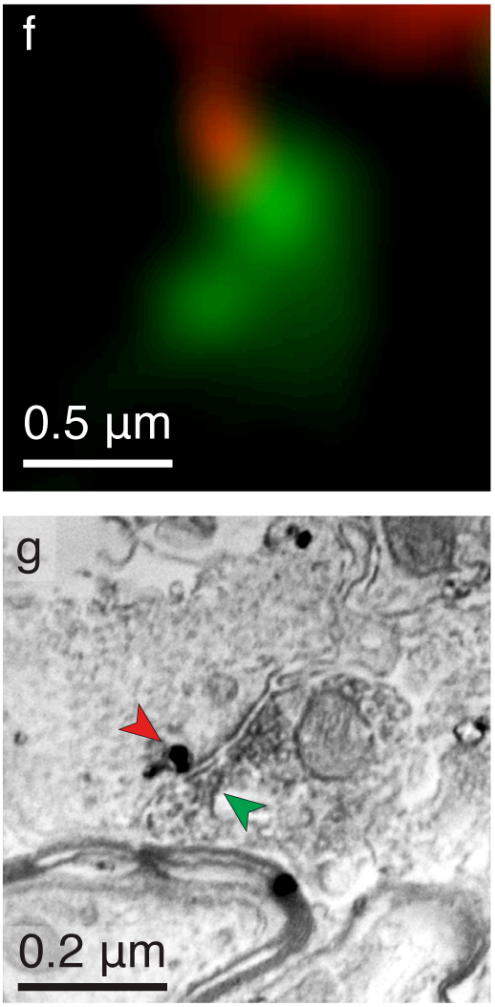

Figure 3.9. *Example of a false positive. Legend same for* ***Figure 3.8****; the 70nm section (bottom panel) in which the labeled spine (black punctate stain, red arrowhead) is closest to the VGluT2+ vesicle pool (green arrowhead) does not contain a PSD, and no synapse is formed between the two labeled structures. The labeled spine's PSD is located in a different section and does not contact the VGluT2+ vesicle pool. This section contains only a small, terminal portion of the spine.*

We examined 3 spines that did not meet the criteria for putative TC contacts in LM, but that were located near (< 75 nm) VGlut2+ puncta (**Figure 3.10.**), none of which were found to be TC synapses under EM.

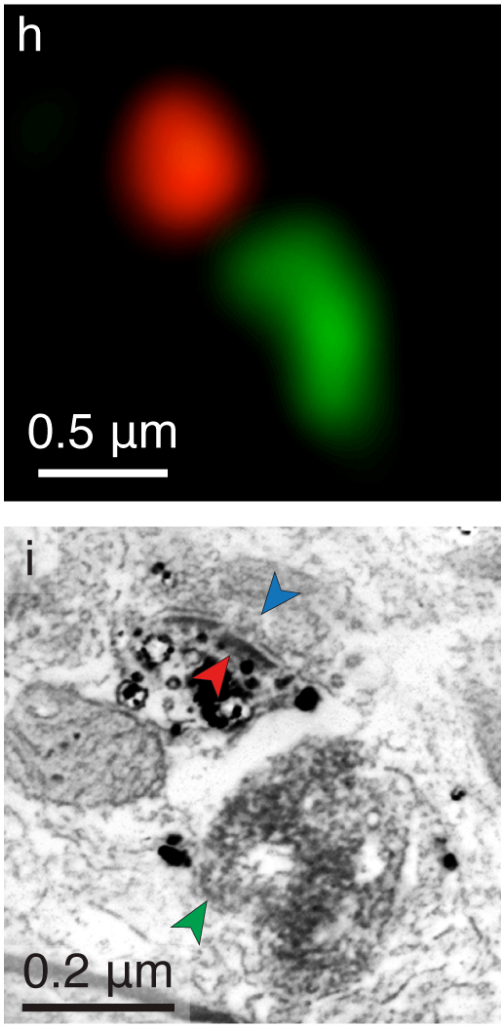

Figure 3.10. *Example of a true negative. Nearby, but non-apposed pre- and post-synaptic structures visualized under confocal microscopy (green, red fluorescence in top panel) are separated by ~50 nm.. This spine fails to satisfy the criteria for putative TC contacts; accordingly, it does not correspond to a synapse when examined under SEM. (Green arrowhead in bottom panel indicates the VGluT2+ vesicle pool in green fluorescence in top panel.) Instead, the labeled spine head (black punctate stain, red arrowhead indicates PSD) forms a synapse with a terminal containing a VGluT2- vesicle pool (blue arrowhead).*

In total we performed correlative microscopy on 7 segments of dendrite from 2 filled neurons in one animal. These dendrite segments containing 219 spines in total, 23 of which were determined to be putative TC synapses in LM (10.5%). Subsequent imaging under EM permitted examination of 16 of those putative TC synapses, 14 of which (87.5%) were determined to be true positives, and 2 false positives. We conclude that our LM strategy produces reliable maps.

3.3. Anatomical distribution of TC synapses

Do TC and CC inputs exhibit distinct spatial patterns of innervation in L4 neurons? We reconstructed the complete dendritic arbors (**Figure 3.11.**) of 6 spiny L4 neurons in somatosensory cortex, scoring each spine according to the criteria described above (n = 17863 spines).

Neurons were randomly sampled with regard to location within the barrel (**Figure 3.12.**).

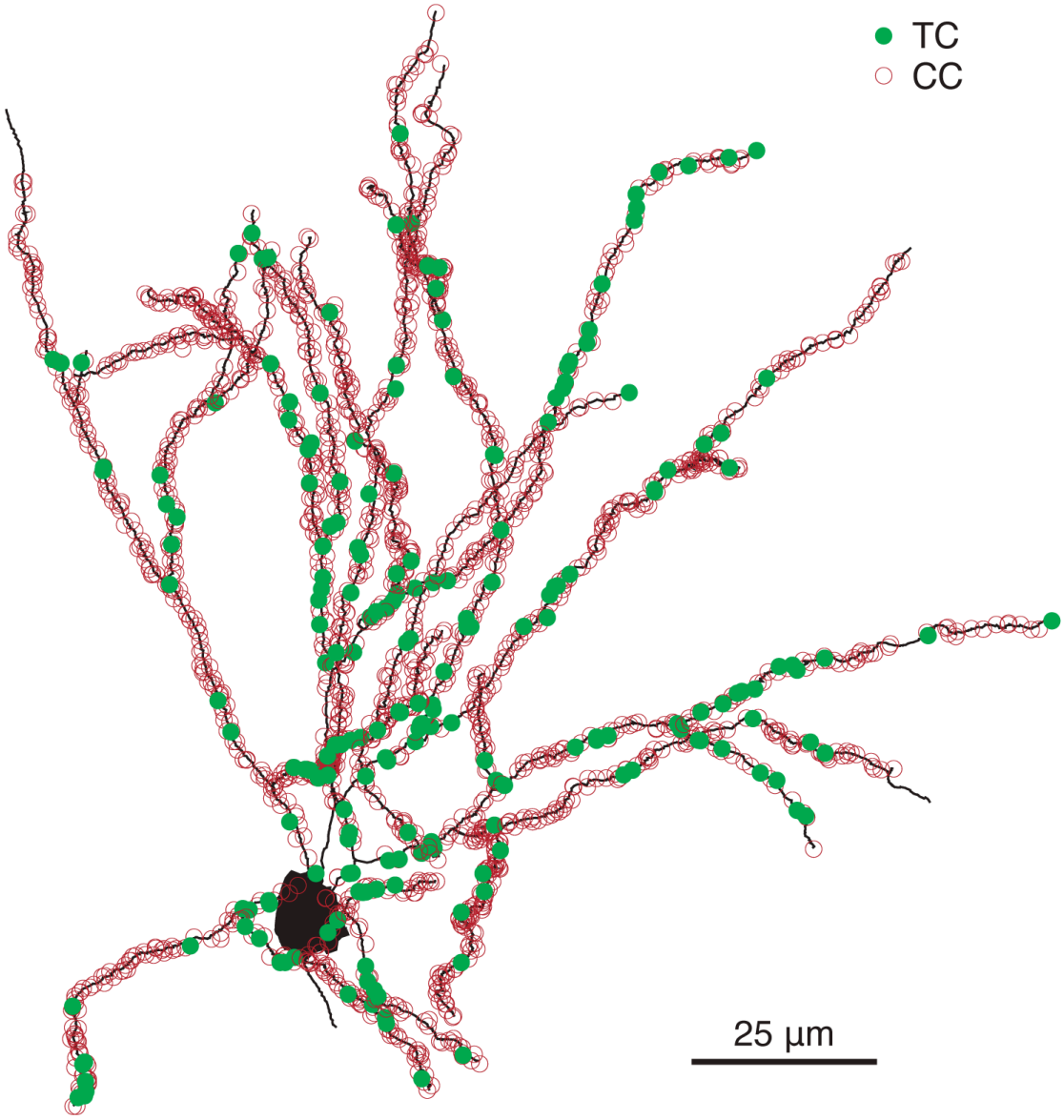

Figure 3.11. *Complete synaptic distribution of a L4 spiny stellate neuron. High resolution 3D reconstruction of a spiny stellate neuron showing individual spines apposed to synaptophysin-EGFP signal, denoted as TC (filled green circles), and unapposed spines, assumed to be CC (empty red circles). This cell corresponds to Cell 3 in* ***Figure 3.13.***

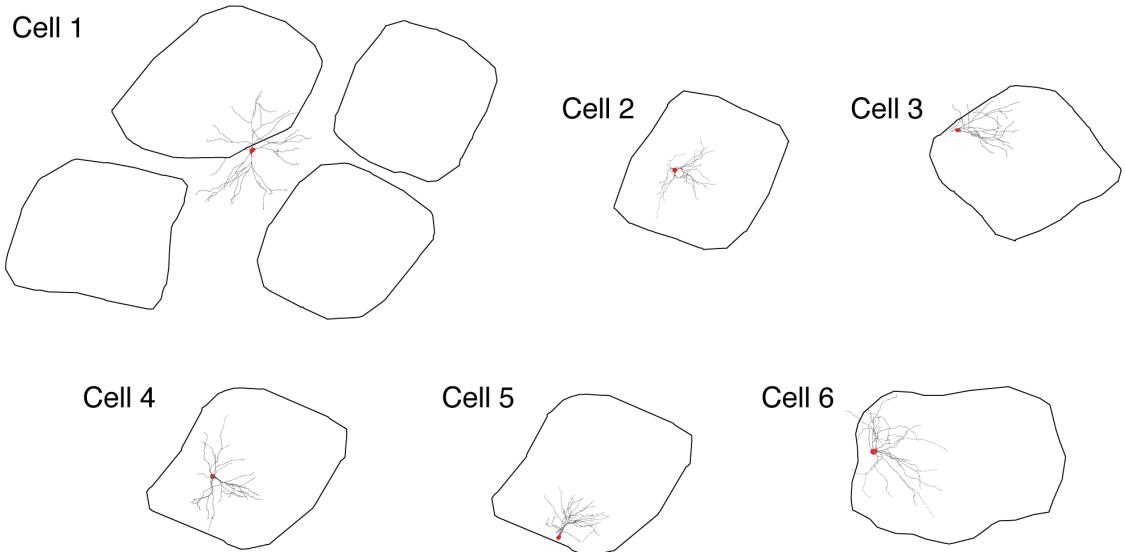

Figure 3.12. *Somata locations and dendritic arbors relative to barrel borders. The six fully reconstructed cells are depicted relative to their barrel's borders. (Barrel borders: black, somata: red, dendritic arbors: grey.) Cell 1, whose soma was located in the septum, is represented alongside its neighboring barrels. Note that Cell 4 and Cell 5 were located in the same barrel.*

3.3.1. TC synapses are more proximal to the soma than CC synapses

Our sample contained three spiny stellate neurons and three star pyramids, including one whose soma was located in the septum between neighboring barrels. Of the 2056 to 4897 spines examined per cell (mean 2977), between 5.92% and 15.2% (mean 9.98%) were scored as TC (**Figure 3.13.**).

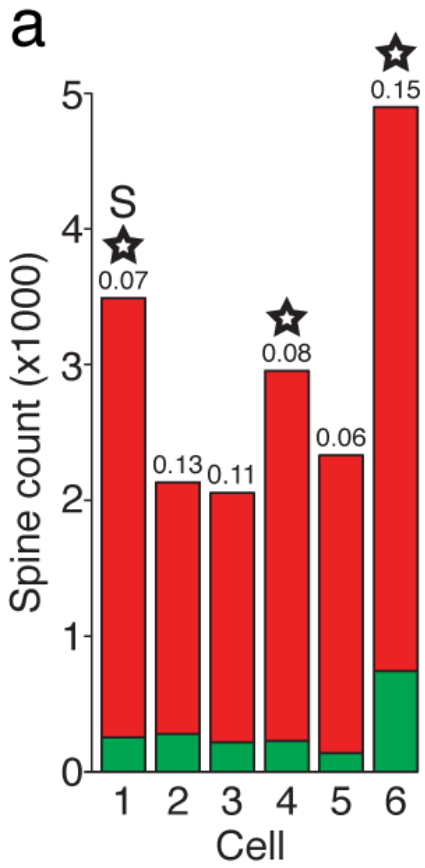

Figure 3.13. *Fraction of putative TC contacts by cell type. Between 6% and 15% of contacts are TC in fully reconstructed dendritic arbors. (stacked histogram; green: TC; red: CC; number: fraction of total spines that are TC; star: star pyramid, all others are spiny stellate; S: septal neuron, all others are barrel).*

Do TC synapses fall more proximally to the soma than CC synapses? The number of both TC and CC spines varied considerably over distance from the soma (**Figure 3.14.**, top left; median of 218 TC spines = 81.6 μm; median of 1838 CC spines = 96.2 μm, or 17.9% more distal; $p < 10^{-5}$, Wilcoxon signed-rank test; corresponds to Cell 3, shown in **Figure 3.11.**). The distribution of the total number of spines was factored out by quantifying the TC/CC ratio (**Figure 3.14.**, bottom left). In 5 out of 6 cells the probability of observing a TC synapse decreased with

distance from the soma**;** in 4 out of 6 this relationship was highly statistically significant ($p = 0.003, 0.33, 3x10^{-6}, 0.80, 0.003, 2x10^{-9}$, n = 3490, 2132, 2056, 2955, 2333, 4897, logistic regression for cells 1-6 respectively). Pooling the spine data from all six cells, TC spines were also significantly more proximal to the soma on average (**Figure 3.14.**, right; $p < 10^{-29}$, n = 17863, logistic regression). We conclude that TC synapses exhibit a subtle spatial bias.

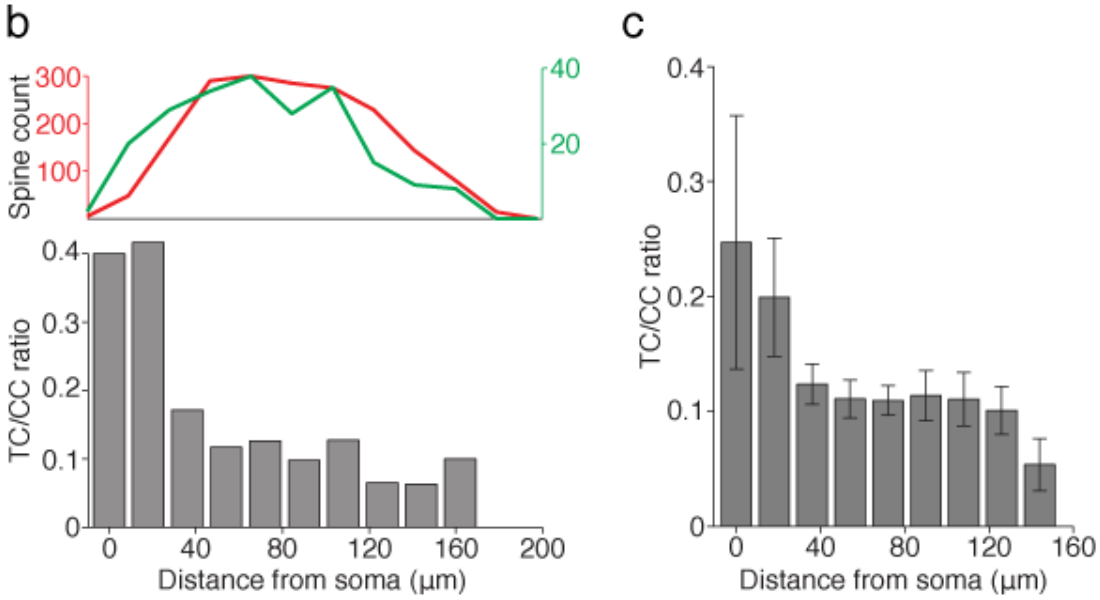

Figure 3.14. *Spatial distribution of TC and CC spines. Left panel, top: TC (green) and CC (red) spine density for one cell (Cell 3, shown in* ***Figure 3.13.****). Left panel, bottom: the ratio of TC to CC spines declines as a function of distance from the cell soma. Right panel: average of all fully reconstructed cells (error bars indicate standard error).*

3.3.2. TC synapses do not form on different types of spines than CC synapses

In a reconstruction comprised of 4897 spines (Cell 6 in **Figure 3.13.**), we classified each spine morphology as either mushroom, stubby or filopodium (Peters and Kaiserman-Abramof 1970). We found that TC contacts did not form preferentially onto any one of the three spine classes (**Figure 3.15.**, stacked histogram; green: TC, red: CC).

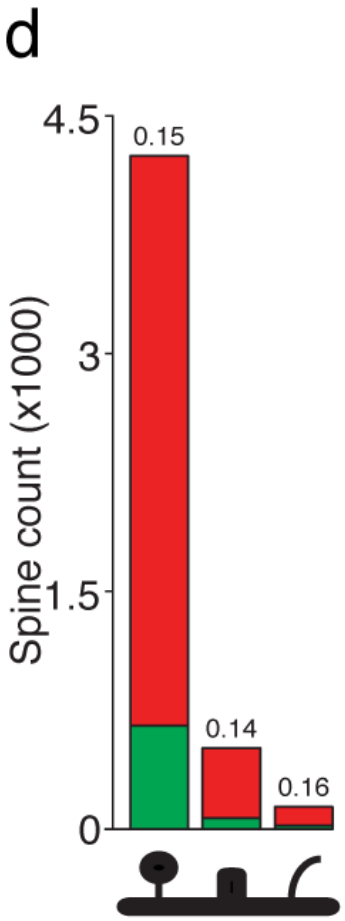

Figure 3.15. *TC and CC fractions by spine type. Spines in cell 6 were classified as either mushroom (left), stubby (middle) or filopodium (right; cartoon denoted on the x axis). The fraction of TC contacts was roughly equal across all three classes of spines (legend same as in* ***Figure 3.13.****).*

3.3.3. TC synapses do not exhibit more clustering than predicted by chance

If synapses from a highly synchronous population of cells such as thalamic neurons (Bruno and Sakmann 2006) were clustered together along a dendritic branch, rather than evenly distributed, they could provide the anatomical basis to support the initiation of dendritic spikes (Lavzin, Rapoport et al. 2012). Does the pattern of TC innervation display any postsynaptic clustering beyond that which would be predicted by chance? Such post-synaptic clusters could span spatial scales on the order of tens of microns, but an exact optimal spacing of constituent spines is unknown. We algorithmically searched for potential clusters, using a range of different definitions of allowable spacing between TC spines in a nominal cluster. For instance, if clusters were nominally defined by inter-spine distances of ≤2 μm, Cell 2 would contain 57 clusters (**Figure 3.16.**, left); if the definition were broadened to inter-spine distances of ≤4 microns, it would contain 73 clusters. We calculated 99% confidence levels by randomly distributing TC synapses according to Poisson statistics (dashed lines) and found that in five out of six cells, the distribution of possible clusters did not significantly cross chance levels. One cell (Cell 6) exhibited a slight but significant tendency for TC synapses to avoid one another rather than cluster (**Figure 3.16.**, right**)**. We conclude that TC synapses do not cluster postsynaptically any more than predicted by chance.

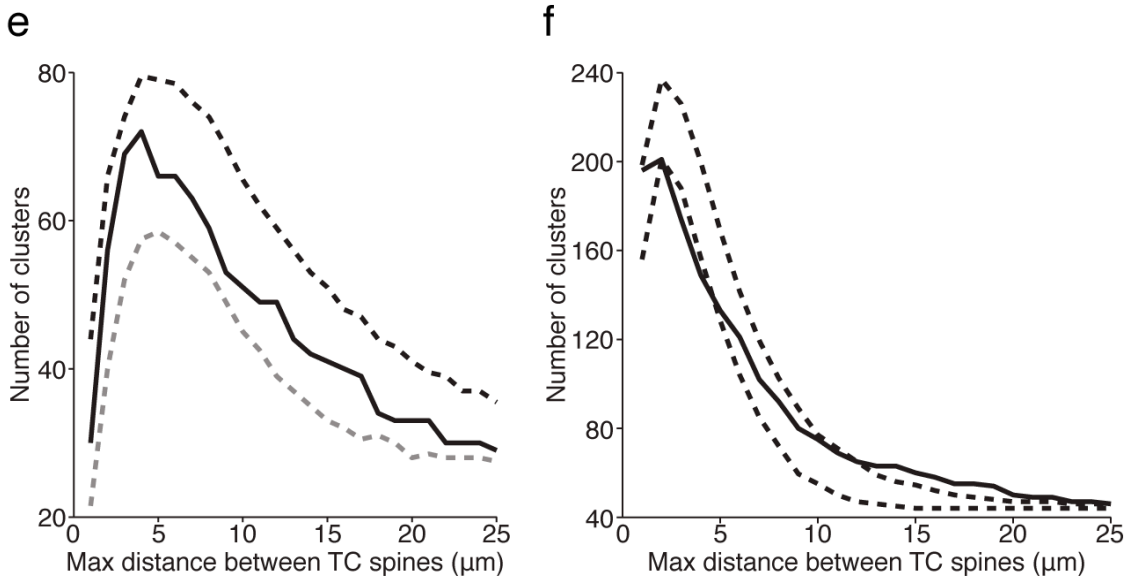

Figure 3.16. *TC spines do not form clusters. Potential post-synaptic clusters were nominally defined using different maximum possible spacings of TC synapses (black). 99% confidence limits obtained by Monte Carlo simulation (gray). Left panel: example of TC synapses clustering at chance levels (cell 2). Here, the most clusters were found for a threshold of 4 um. Right panel: the only cell deviating from chance exhibited anti-clustering of TC synapses when the threshold for a cluster was set to 3-4 um (cell 6).*

3.4. Methods

3.4.1. Animals

We used 5 adult (weight 174-408 grams) Wistar rats (Hilltop Laboratories, Charles River) for experiments.

3.4.2. Virus injections

Thalamic boutons were labeled with virus as previously described (Wimmer, Nevian et al. 2004). Briefly, animals were injected with adeno-associated virus (AAV1/2) encoding a synaptophysin-EGFP fusion protein under control of a hybrid CMV enhancer/chicken β-actin (CBA) promoter (titer: 1-4 $x10^7$ particles/ml). Rats were anesthetized with isoflurane, and rectal body temperature was maintained at 37°C with a heating pad. Injections were stereotaxically targeted to 2.85 mm posterior of bregma, 3.2 mm lateral of the midline, and 5.05 mm deep from the pia. Calibrated micropipettes (5 μL, intraMARK, Blaubrand, Wertheim, Germany) were used to measure the injected volume (250 nl). After injections rats were left to recover, and virus was allowed to express for ~5 months prior to cell filling. Injections infected 85-95% of thalamic neurons. No cortical neurons were found to be infected. Rats continued to explore their environments with their whiskers normally and showed no behavioral abnormalities, including in a separate group of control animals expressing the protein for ~1.5 years in which no cells were filled.

3.4.3. *In vivo* preparation

Rats were anesthetized with isoflurane, and rectal body temperature was maintained at 37ºC by a heating pad. The parietal and occipital bones were exposed, and a metal post for positioning the head was attached to the skull using dental acrylic. The parietal bone overlying left barrel cortex was thinned with a dental drill until transparent, and a craniotomy was made over a thin region of skull (0.5 x 0.5 mm; centered 2.5 mm posterior to bregma and 5.5 mm lateral of the midline). The barrel field was mapped using glass pipettes with tips of ~5 μm inside diameter (ID) filled with artificial cerebrospinal fluid (ACSF; 135 mM NaCl, 5.4 mM KCl, 1.8 mM $CaCl_2$, 1.0 mM $MgCl_2$, and 5.0 mM HEPES [pH 7.2]) and inserted vertically to a microdrive depth of ~700 μm. Signals were amplified, band-pass filtered at 0.3-9 kHz, and played over an audio monitor. Whiskers were deflected manually using hand-held probes to determine the principal whisker corresponding to any given penetration.

3.4.4. Cell Filling

Juxtasomal pipettes with tip ID of ~0.5 μm were pulled from 2-mm filamented borosilicate glass. Pipettes were tip filled with ACSF containing 2% biocytin and inserted perpendicular to the pia. After a single-cell recording was established, square current pulses (1-3 nA, 250 ms on, 250 ms off) were passed for several minutes. Regardless of whether cells were filled juxtasomally or intracellularly (see below) 1-2 h were usually allowed to elapse before perfusion.

3.4.5. Immunohistochemistry for light microscopy

Vesicular Glutamate Transporter 2 (VGluT2) protein labels thalamic but not cortical terminals in L4. Lesioning thalamus depletes VGluT2 immunoreactivity in cortex (Fujiyama, Furuta et al. 2001). *In situ* hybridization reveals dense VGluT2 expression in thalamus but little or no VGluT2 mRNA in somatosensory cortex except in a subset of Layer 3 (L3) cells (Graziano, Liu et al. 2008), which generally do not establish synapses in L4 (Bruno, Hahn et al. 2009, Lefort, Tomm et al. 2009).

All reagents were dissolved in 0.1 M phosphate buffer (PB) unless otherwise noted. The rat was perfused transcardially with cold 0.1 M PB followed by 4% paraformaldehyde (PFA). The brain was incubated overnight in 4% PFA at 4°C and then cryoprotected using 30% sucrose. Barrel cortex was cut tangentially in 50-µm sections on a freezing microtome (Microm HM 450). Floating sections were incubated in 1 mg/mL $NaBH_4$ for 7 min to reduce autofluorescence, then blocked in 5% Normal Goat Serum (NGS) and 1% Triton-X, rocking at room temperature. Rabbit anti-VGluT2 primary antibodies (1:2000 dilution, Synaptic Systems) and streptavidin-conjugated Alexa488/594 (1:1000 dilution, Invitrogen) were incubated for 12-18 h in 1% NGS and 1% Triton-X, rocking at 4°C. Goat anti-rabbit secondary antibodies conjugated to Alexa488 or Alexa594 (1:200 dilution, Invitrogen) were incubated for 2-4 h in 1% NGS and 1% Triton-X,

rocking at room temperature. Sections when then mounted onto glass slides under coverslip in SlowFade Gold (Invitrogen).

3.4.6. Microscopy and reconstruction

Epifluorescence images were obtained using an Olympus BX-51 upright microscope equipped with GFP and Alexa594 fluorescence filter cubes, a mercury light source, and 4x, 10x, and 20x air objectives (0.13, 0.3, and 0.5 NA respectively). High-resolution confocal image stacks were acquired using a Leica TCS SP2 or SP5 laser scanning microscope with 488-nm (EGFP/Alexa 488) and a 543-nm (Alexa 594) excitation wavelength using a 63x 1.3 NA glycerol objective and 5x digital zoom, oversampled with regard to Nyquist (voxel dimensions: 48.1 nm length x 48.1 nm width x 136.4 depth). The objective correction collar was set by maximizing the reflection of the laser off the slide. Signal-to-noise ratio was improved by 4x line-averaging. Neighboring stacks were set to overlap by ~5 μm to facilitate registration. Stacks were deconvolved using Huygens (Scientific Volume Imaging); parameters were optimized to avoid ringing (**Figure 3.17.**).

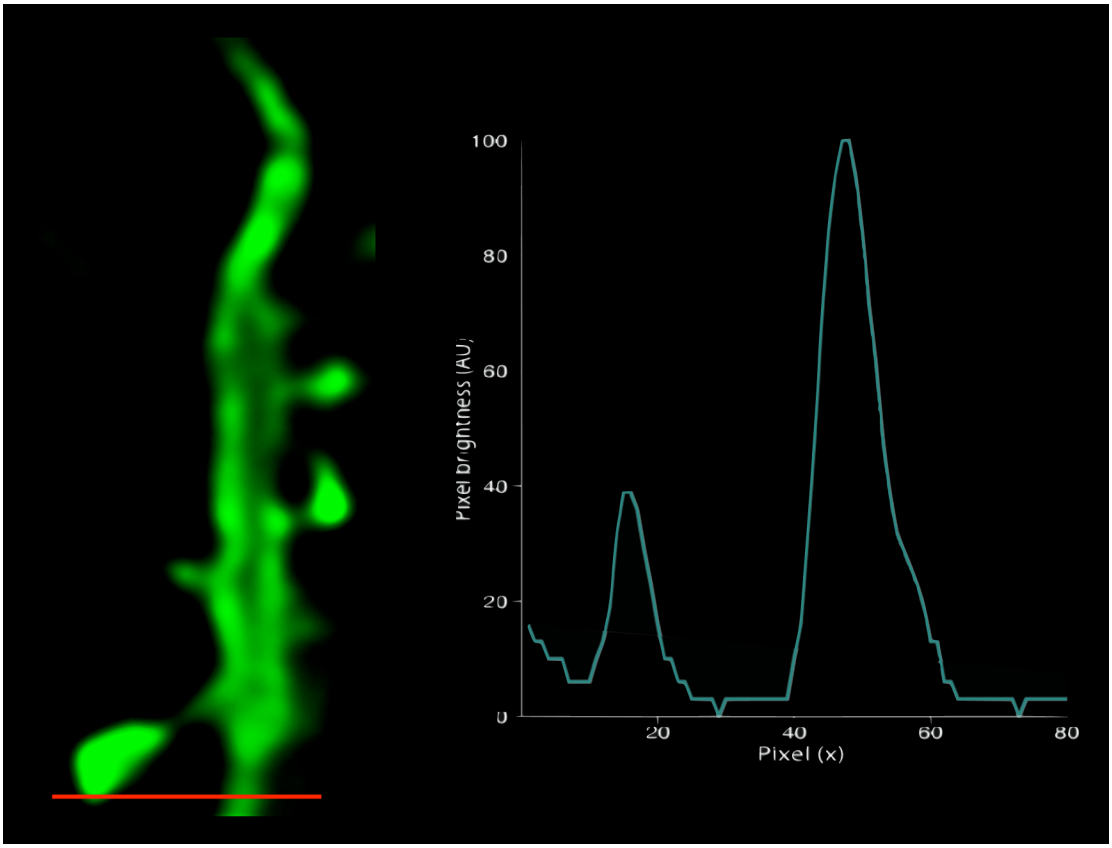

Figure 3.17. *Deconvolution does not cause ringing. A linescan (values plotted at right) across a single deconvolved optical plane (left) shows no ringing, a common artifact due to poorly set deconvolution parameters.*

Individual image stacks were imported into Neurolucida (MBF Biosciences) for reconstruction, after optimizing the dynamic range of each channel. Somata and dendrites were traced in 3 dimensions through the stack (including dendrite thickness for the volumetric reconstruction of cell 6), and each spine was examined for apposition to a VGluT2 or synaptophysin-EGFP punctum. Dendritic spines that either partially overlapped or were in direct contact with a

punctum were scored as TC. Spines that were not, including spines that were very near puncta but for which there was no signal between the border of the spine and the border of the VGluT2 punctum (e.g. **Figure 3.10.**), were scored as CC. Reconstructed segments were spliced together, with care to prevent any double-scoring of spines arising due to the overlap between neighboring image stacks. Using lower-magnification images of the dendritic arbor as reference, the spliced reconstructions of consecutive 50-µm sections where then spliced together, revealing the neuron's complete dendritic arbor. This final splicing step revealed that this method suffers negligible tissue loss due to sectioning, as the dendrite reconstructions across consecutive sections matched up with virtually no interruption. Anatomy data were analyzed using Neurolucida and custom-written routines in MATLAB.

3.4.7. Correlative LM-EM protocol

This protocol was developed after multiple unsuccessful attempts; these are outlined in Appendix A.

All reagents were dissolved in 0.1 M sodium phosphate buffer unless otherwise noted. After electroporating a single cell with biocytin (described above), the rat was perfused transcardially with cold 0.1 M PB buffer followed by 2% PFA and 0.75% glutaraldehyde (Electron Microscopy Sciences) in PB. The brain was incubated overnight in 4% PFA at 4°C and then cryoprotected using

30% sucrose. The brain was then frozen in a -80°C freezer for 20 min to fracture membranes rather than permeabilizing sections. Barrel cortex was cut tangentially in 25-µm sections on a freezing microtome. Floating sections were incubated in 1 mg/ml NaBH4 for 7 min to reduce autofluorescence, in 3% H_2O_2 for 30 min to quench endogenous peroxidases, and blocked in 5% normal goat serum (NGS) for 1-2 h at room temperature. Rabbit anti-VGluT2 primary antibodies (1:2000 dilution, Synaptic Systems) to label VPM terminals, and a nanogold-streptavidin-conjugated Alexa488 (1:100 dilution, Nanoprobes) to label the postsynaptic dendrites, were incubated for 12-18 h in 1% NGS, rocking at 4°C. The VGluT2 primary antibodies were then reacted simultaneously with goat anti-rabbit secondary antibodies conjugated to Alexa594 (1:200 dilution, Invitrogen) and horseradish peroxidase (HRP) (1:8.3 dilution, Invitrogen) for 12-18 h, rocking at 4°C. Sections were stored in 0.1 M buffer at 4°C during light imaging (1 to 3 days). For imaging, individual sections were trimmed (1 x 1 mm), mounted onto glass slides under coverslip in SlowFade Gold (Invitrogen), imaged under confocal microscopy as above, and then immediately unmounted and washed thoroughly. SlowFade Gold mounting medium slightly reduced HRP reactivity so the amount of time the sections were mounted was kept to a minimum (1-4 h).

Pre- and post-synaptic markers were labeled for scanning electron microscopy (SEM) by incubating sections in 50 mM glycine (3 x 10 min) and 1% bovine serum albumin (3 x10 min) followed by washes in distilled H_2O (3 x 10

min). The nanogold particles (in the dendrite) were enhanced using an HQ Silver enhancement kit (Nanoprobes) for 6-13 min rocking at room temperature covered in tin foil and then washed thoroughly in distilled H_2O. After transferring the sections back to buffer, HRP (at the VGluT2+ terminals) was reacted with a freshly made solution of 1.5 mg/ml diaminobenzidine (Dako) and 0.01% H_2O_2 for 20 min rocking at room temperature covered in tin foil, and then washed thoroughly. The previously fluorescent signal was then light-absorbent and was easily detected under bright-field microscopy (**Figure 3.18.**).

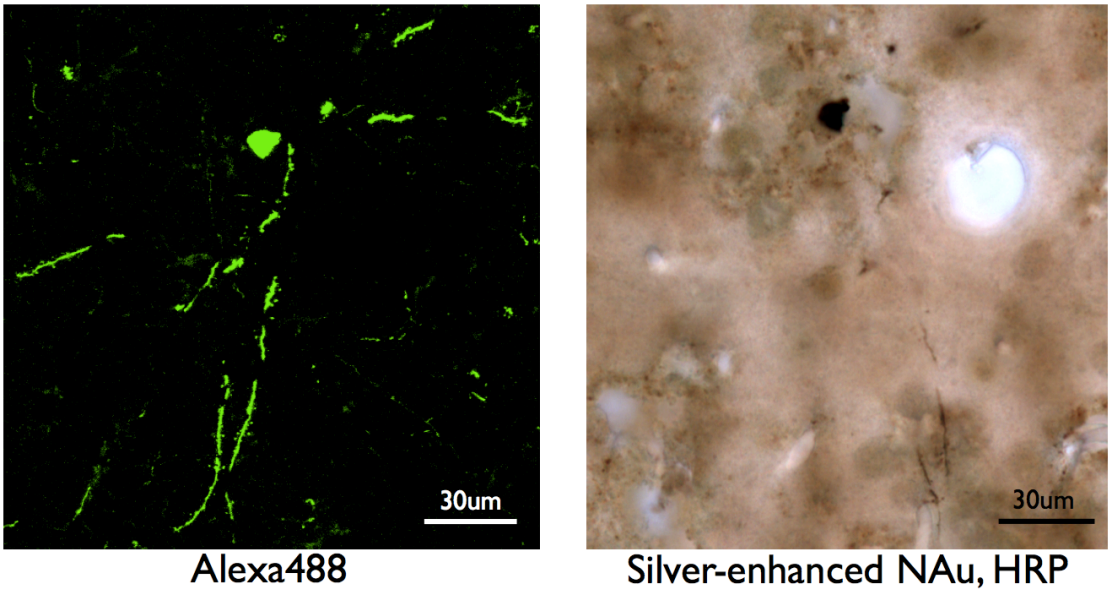

Figure 3.18. *Silver enhancement of fluorophore-conjugated gold particles. Left: fluorescently labeled soma and dendrite visualized under confocal microscopy (z-projection); right: following silver-enhancement of the fluorophore-conjugated gold particles, the soma and dendrite are rendered visible under bright-field*

microscopy.

To render cytoplasmic membranes electron-dense, the 25-µm sections were reacted in PBS (0.1 M) buffer containing 0.5% osmium and 1.5% K3[Fe(CN)6] (EMS) for 20 min rocking at room temperature. No uranyl acetate was employed in order to prevent washout of the enhanced silver signal. Sections were dehydrated in ethanol grades of 50%, 70%, 95% (all 1 x 40 sec), and 100% (2 x 40 sec) in a microwave (Pelco 3451 system, with cold spot) Dehydrated tissue was immediately infiltrated in 1:1 epon (Fullam Epox 812) and ethanol for 15 min in the microwave, then in 100% epon resin (2 x 15 min each with fresh epon) in the microwave. Specimens were then mounted between two plastic slides with epon and polymerized overnight at 60°C.

The next day the polymerized epon wafers with sections were separated from the plastic slides, and regions of interest were observed and photographed. Regions of interest were cut from the section and remounted on a small drop of epon on a blank Beem capsule block and placed in a spring tension apparatus (to keep the section piece flat on the block) and placed in the oven at 60°C for 18-24 hours. Once polymerized, the blockface was trimmed down to a slightly trapezoidal shape with sides of ~1.5 to 2mm. A small notch was trimmed off the upper right side corner for orientation purposes. 7µm sections were then cut with a diamond histo-knife using an ultramicrotome. Each 7µm section is collected using fine forceps and placed in order in drops of water on a glass slide. The sections are

then placed in 95% ethanol in a glass multi-well dish for a minute or two to make them wrinkle free and flat. Using fine forceps, each section was transferred to a piece of lens tissue paper to wick off the ethanol. The sections were then placed in order on a clean glass slide and coverslipped in immersion oil.

Sections were observed using a light microscope with phase optics, and any sections containing the original area of interest were photographed to use as a map for orientation in the electron microscope. The coverslip was gently removed, and each chosen section individually washed in 95% ethanol 3X for ~15 seconds to remove all the immersion oil, then placed on a piece of lens tissue paper to wick off the ethanol as previously. The section was then placed carefully on a very small drop of epon on a faced off blank Beem capsule block and placed in the spring tension apparatus. This was repeated for each section that will be used for ultrathin sectioning. A plastic slide was stacked with two glass slides (plastic slide on bottom) and secured in the apparatus. Each block was slowly raised up toward the plastic slide by releasing the spring so that the section is held perfectly flat to the plastic slide with slight tension. The apparatus was then placed in the oven at 60°C for at least 18-24 hours.

Serial ultrathin 70 nm sections were cut using a UC6 Ultramicrotome (Leica) equipped with a 45° Diamond Knife (Diatome). The ultrathin sections were collected onto Kapton tape using ATUM (Hayworth, Kasthuri et al. 2006) and placed on a silicon wafer (UniversityWafer) (**Figure 3.19.**). Sections were stained

for 30 sec with lead citrate (Leica) and coated with a thin carbon layer (<100 nm).

A Field Emission SEM (Sigma, Zeiss) was employed to acquire electron microscopy images. Volumetric reconstructions were traced in TrakEM2 (Cardona, Saalfeld et al. 2012) from image stacks of several hundred planes (197 x 197 μm side, 12-nm pixel, "low magnification"). These were compared with the previously acquired confocal image stacks, visualized using FIJI (Schindelin, Arganda-Carreras et al. 2012), allowing registration of segments of dendrites and individual spines across both imaging modes (**Figure 3.20.** and see also **Figure 3.5.**).

Although the tissue's ultrastructure was resolvable in low-magnification image planes, higher-magnification image stacks (4.1 x 4.1 μm side, 2-nm pixel, "high magnification") were acquired around spines putatively identified in the light to be TC. Three-dimensional renderings of the volumetric tracings were produced using 3ds Max (Autodesk).

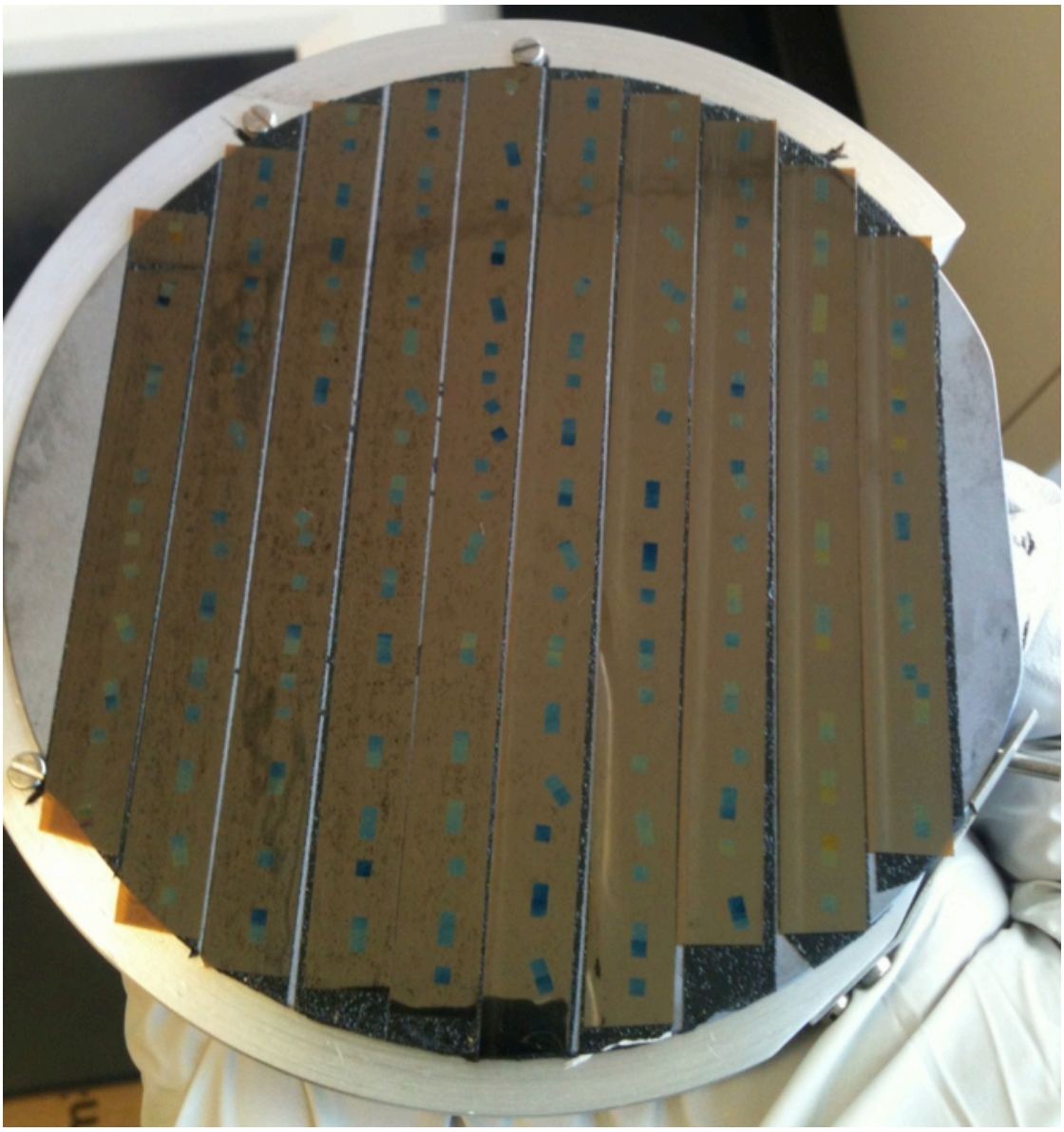

Figure 3.19. *Silicon wafer for SEM imaging. Ultrathin serial sections are collected onto 10 strips of Kapton tape, mounted on a silicon wafer.*

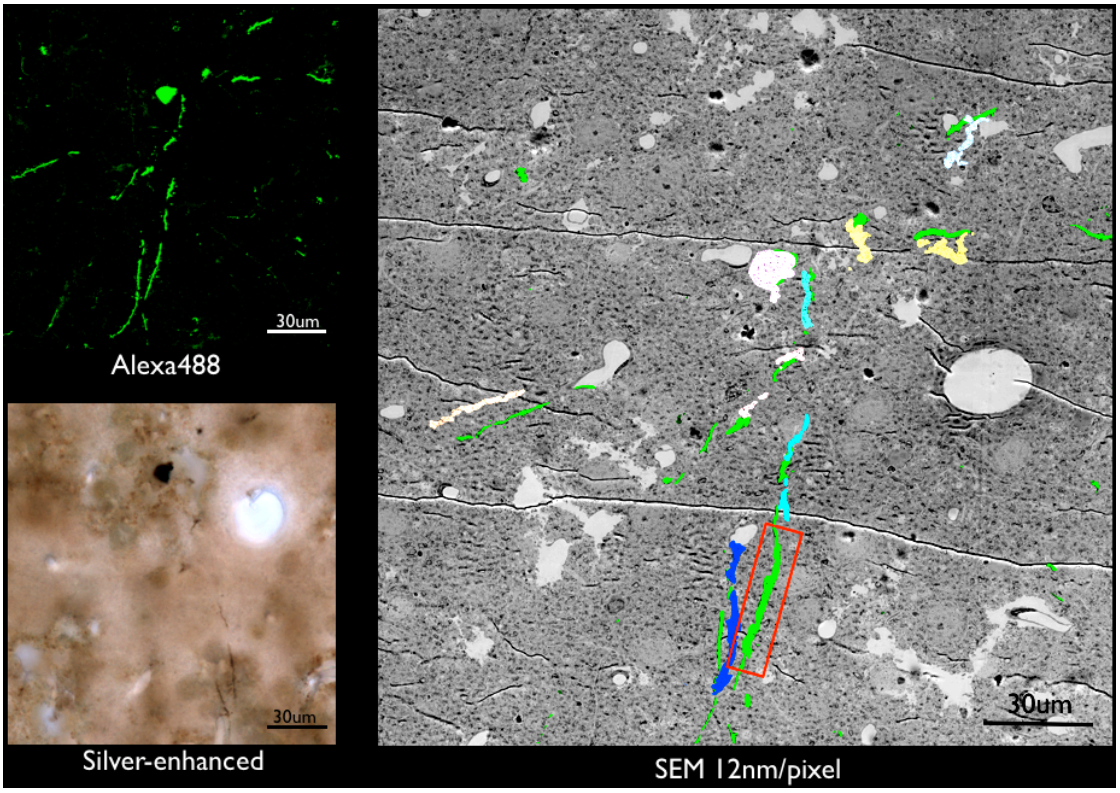

Figure 3.20. *Registering dendrite segments in LM and EM. Fluorescence (left, top), and bright-field (left, bottom, following silver-enhancement) visualization of dendrites corresponds to the reconstructed dendrites (right, colored segments) based on the low-magnification SEM stack. Left panels are reproduced from Figure 3.18 for comparison.*

Chapter 4

The strength of TC and CC inputs onto L4 barrel neurons

4.1. Compartmental modeling predicts similar synaptic strengths for TC and CC inputs

Our results indicate that on average TC synapses fall more proximally to the soma than CC synapses. To determine whether this spatial configuration and the passive filtering properties of L4 neuron dendrites are such that TC inputs depolarize the soma more strongly than CC inputs, we constructed a detailed compartmental model using actual morphological and physiological parameters measured *in vivo*.

4.1.1. Construction of the compartmental model (I): dendritic morphology

We reconstructed a star pyramid's complete dendritic arbor, including its detailed volumetric characteristics and scoring its spines as TC or CC as above (**Figure 4.1.** and **Figure 4.2.**).

A star pyramid was chosen since the dendritic arbor of a star pyramid is more extensive than that of a spiny stellate, and should maximize possible filtering effects. The volume of the spine heads and spine necks were not included in the reconstruction.

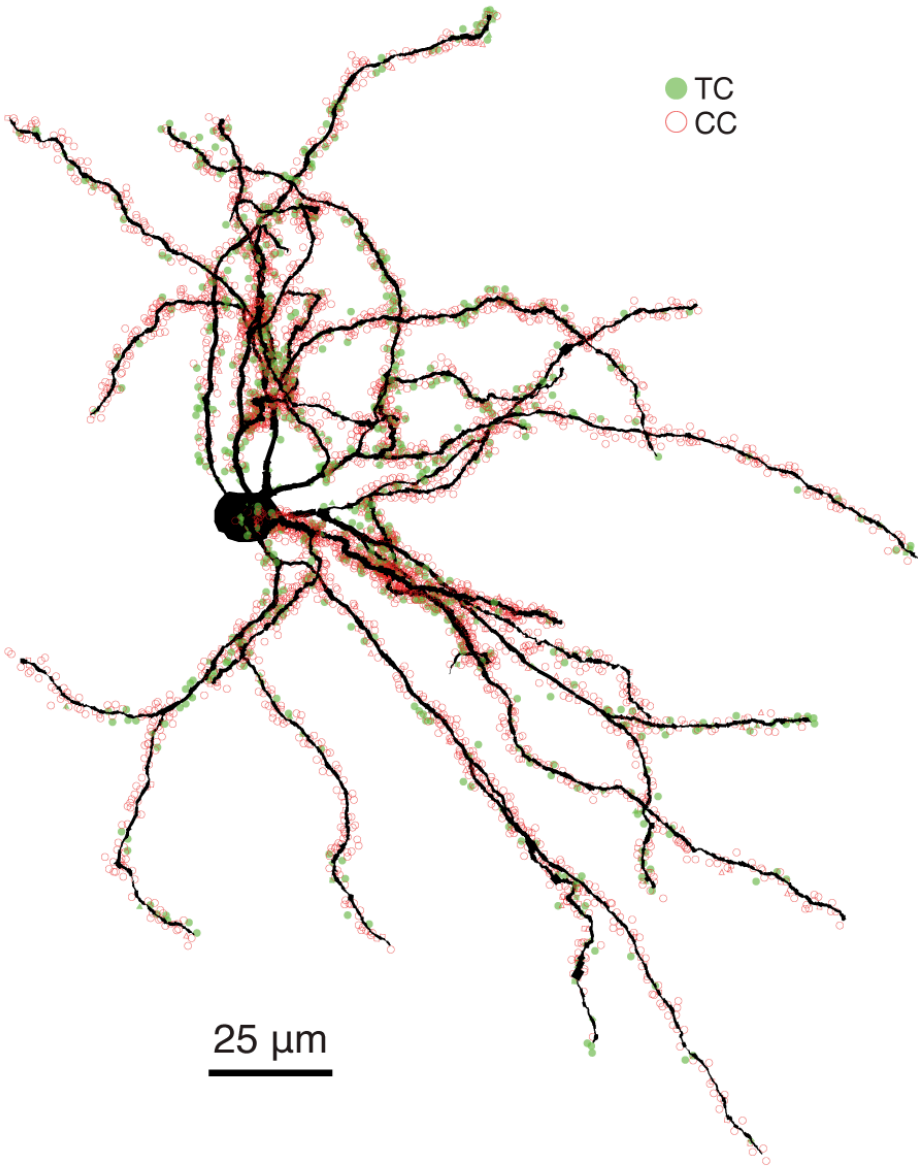

Figure 4.1. *Volumetric reconstruction of the L4 star pyramid used in the model: top view. The reconstruction includes the locations of TC (green, closed circles) and CC (red, open circles) spines. This cell was recorded in the whole-cell configuration and corresponds to cell 6.* ***Figures 4.1*** *and* ***4.2*** *were generated in Neurolucida.*

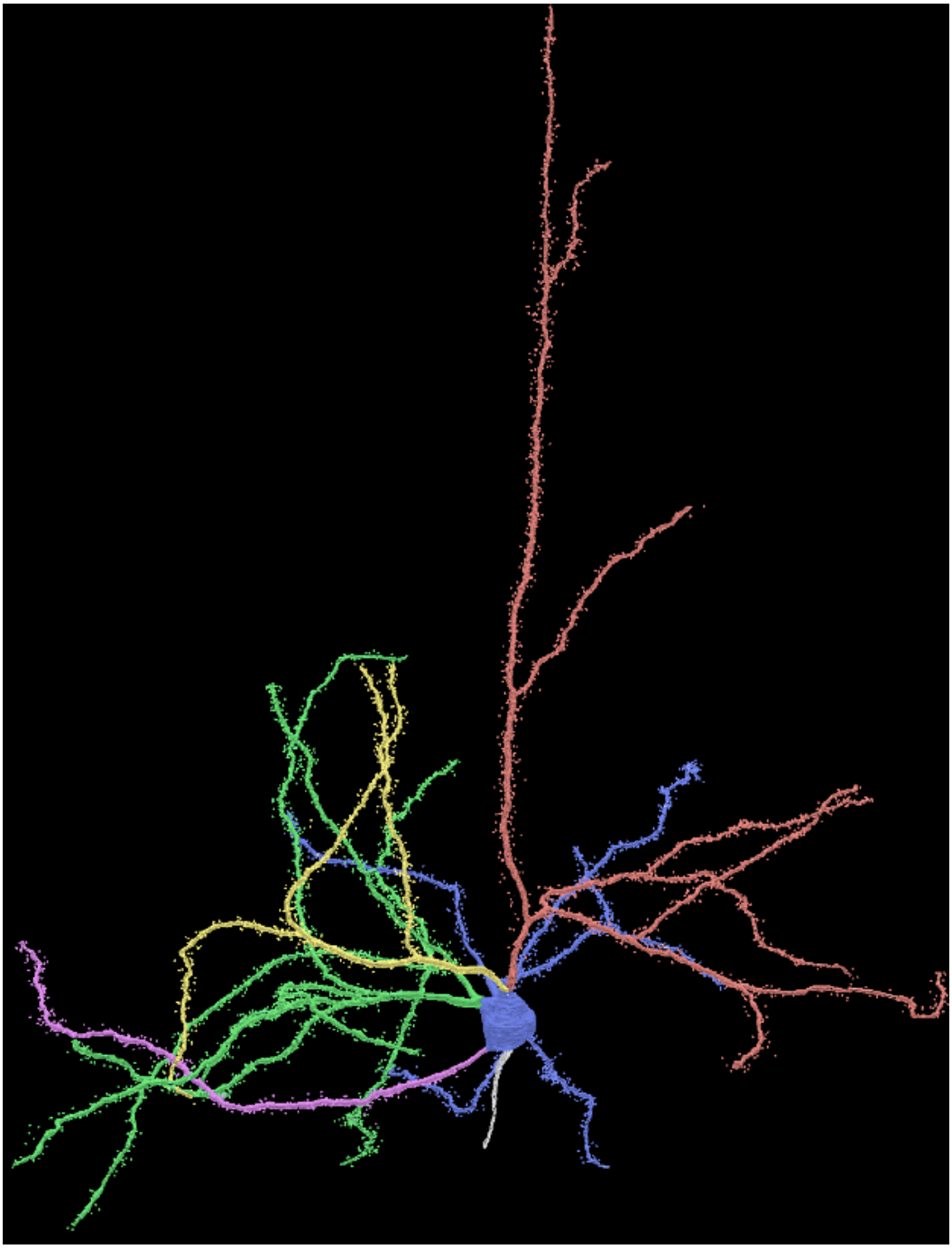

Figure 4.2. *Volumetric reconstruction of the L4 star pyramid used in the model: side view. Each primary dendrite is highlighted in a different color. Initial portion of the axon is white. The apical dendrite is salmon.*

4.1.2. Construction of the compartmental model (II): spine identity

As the others in the dataset, we found that this cell's TC spines were distributed more proximally than CC spines (**Figure 4.3.**) (median of 743 TC spines = 59.4 µm, median of 4154 CC spines = 65.8 µm or 10.8% more distal).

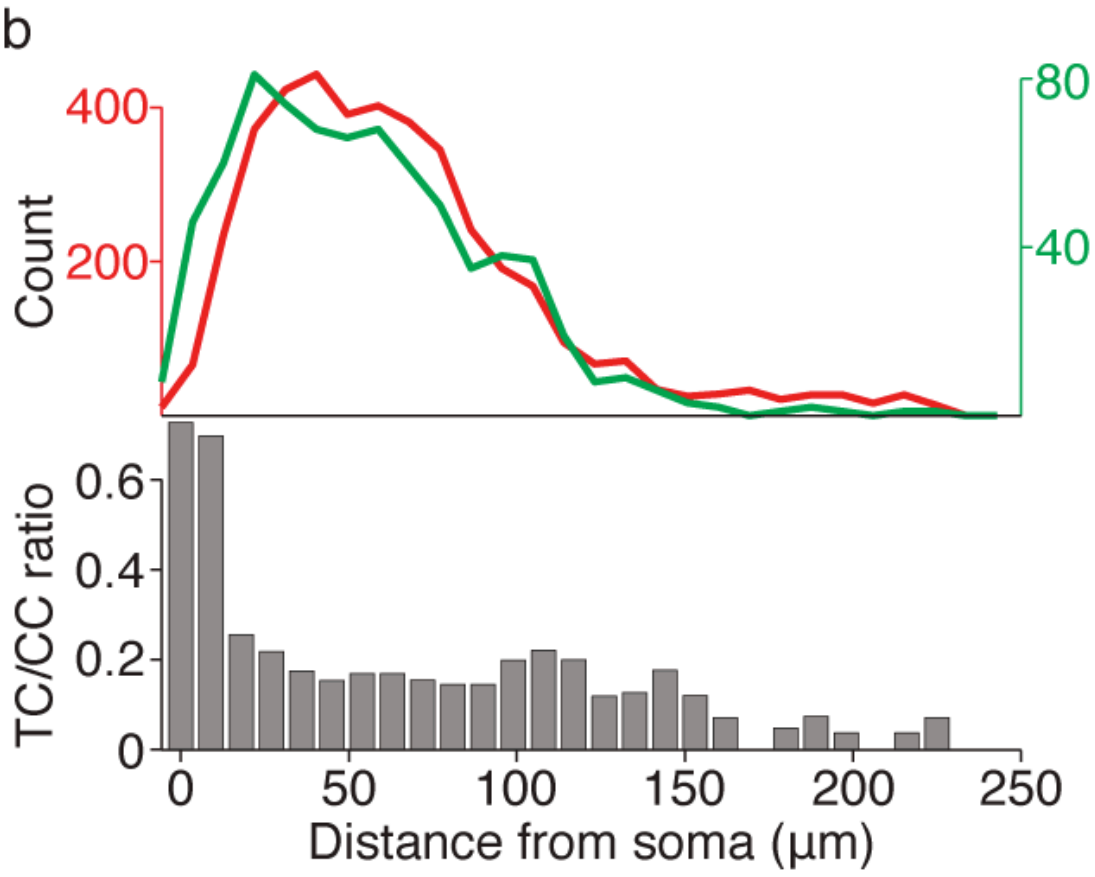

Figure 4.3. *Spatial distribution of spines in the star pyramid used in the model. Top: TC (green) and CC (red) spine density for this cell. Bottom: the ratio of TC to CC spines declines as a function of distance from the cell soma.*

4.1.3. Construction of the compartmental model (III): biophysical parameters

We then turned to modeling this cell's biophysical parameters. Even with precise morphological measurements of the dendrites, the numerous possible combinations of biophysical parameter values (i.e., specific axial resistance R_i, specific membrane resistance R_m, and specific membrane capacitance C_m) can yield models with drastically different passive filtering properties. We therefore fit the model by measuring the cell's impedance function, i.e. the *in vivo* voltage response of the actual neuron, recorded whole-cell, to pink noise (300-Hz cutoff) current injection (**Figure 4.4.**).

The combined morphology and impedance measurements constrained the fit of R_i, R_m and C_m to a narrow range. A 5-parameter model with independent dendritic and somatic R_m and C_m variables did not fit the data appreciably better than the 3-parameter model. We verified that distal dendrites contribute to the model's impedance by varying specific membrane conductance or capacitance in 4 short, distal terminal dendrite segments of the model's 48 segments and observing a resulting change in the fit (**Figure 4.5.**).

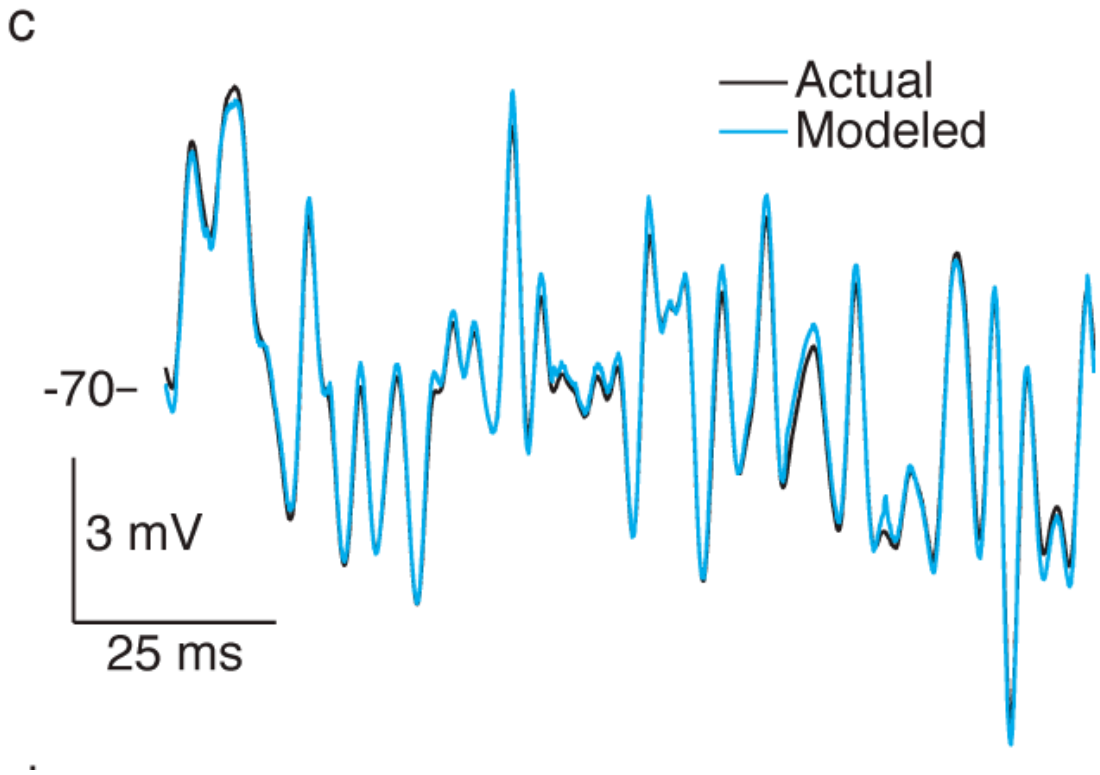

Figure 4.4. *Fitting the voltage response of the model. Voltage responses of actual cell (black) to somatic injection of pink noise current and the fitted model (blue) to the same current injection. A compartmental model based on the volumetric morphology shown in* ***Fig. 4.1.*** *and* ***Fig. 4.2.*** *and the voltage response were used to constrain the fit of three biophysical parameters (axial resistance, specific conductance, and specific capacitance).*

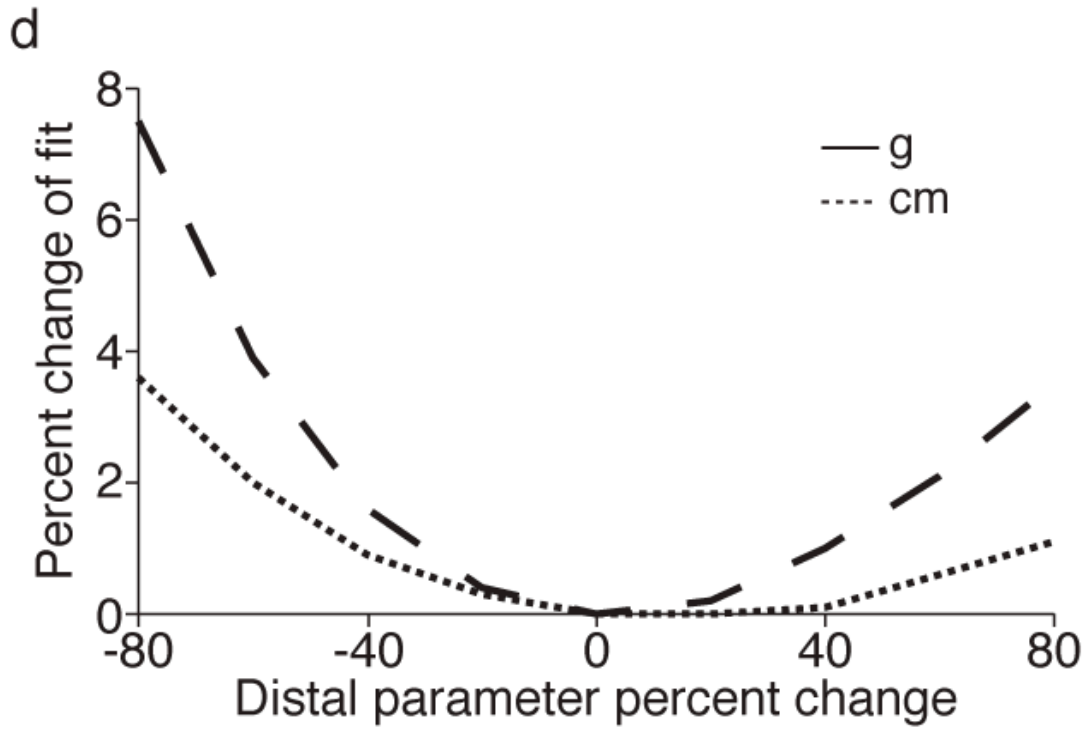

Figure 4.5. *Sensitivity of the model to distal compartment parameters. Percent change in mean squared error (MSE) of the model's fit when varying the specific membrane conductance and capacitance (g and cm, respectively) in 4 short, distal terminal dendrite segments of the cell's 48 segments.*

4.1.4. Construction of the compartmental model (IV): synapse parameters

We then sought to approximate the average synaptic conductance magnitude and timecourse (assuming it can be modeled using an alpha function) of each spine. For this we referred to an *in vitro* dataset of 131 monosynaptic connections obtained using dual intracellular L4/L4 recordings **(Figure 4.6.)** (Feldmeyer, Egger

et al. 1999). The parameters we fit our CC synapse properties to were: (1) EPSP rise time (20-80% of peak), (2) EPSP decay time constant, and (3) EPSP amplitude based on an estimated 3.4 release sites per synapse.

Figure 4.6. *(Following page) Approximation of the average synaptic conductance parameters. Simulated (left column) and recorded (right column) EPSP parameters for 20%-80% rise time (top row), decay time constant (middle row), and amplitude (bottom row) for all CC synapses in the model, versus all 131 CC connections measured* in vitro. *To fit EPSP amplitude we assumed that the L4 neurons form 3.4 connections on average, as estimated by the experimental study. In the right column, open histograms represent recordings at 34-26˚C, closed at 21-23˚C. The distributions on the left were produced by using an alpha synaptic conductance function with the following parameters: time to peak (tau = 0.7 ms), maximum conductance (g_{max} = 0.6 nS), reversal potential (e = 0 mV). Figures in the right column adapted from (Feldmeyer, Egger et al. 1999).*

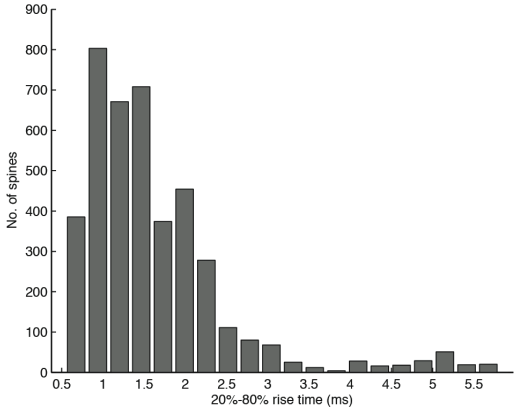
No. of spines
20%-80% rise time (ms)

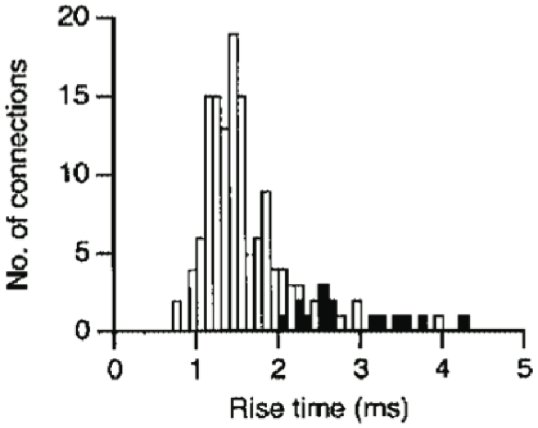
No. of connections
Rise time (ms)

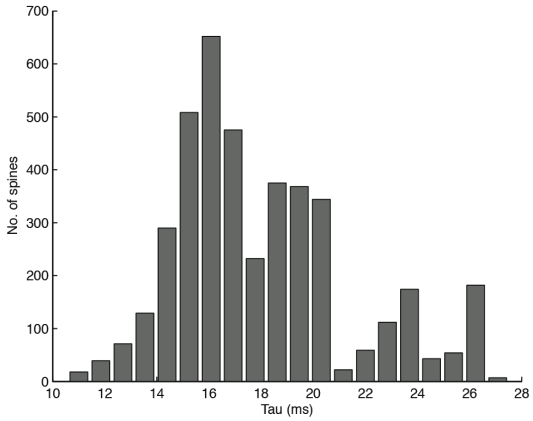
No. of spines
Tau (ms)

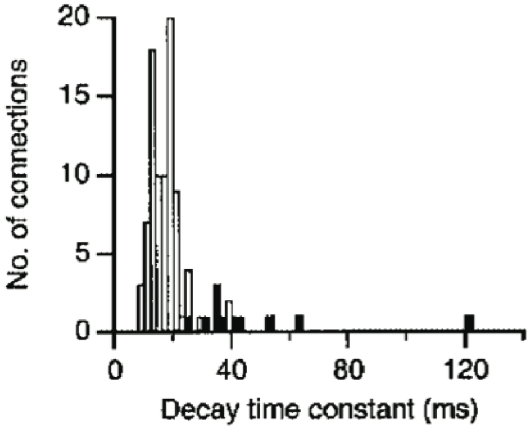
No. of connections
Decay time constant (ms)

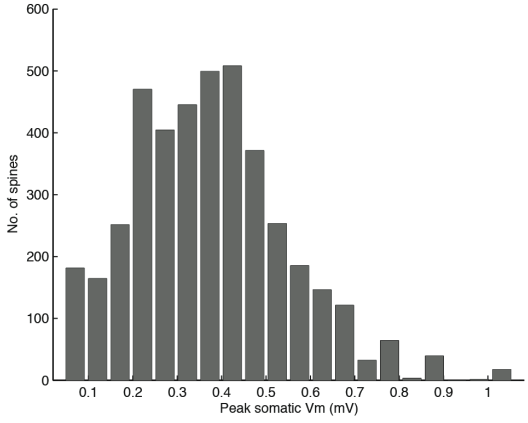
No. of spines
Peak somatic Vm (mV)

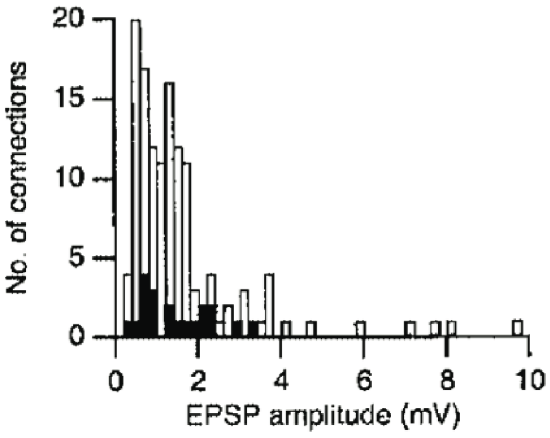
No. of connections
EPSP amplitude (mV)

4.1.5. Simulation of all TC and CC inputs

We then simulated a synaptic conductance at each spine location observed in the reconstruction, measuring the resulting voltage change at the soma (**Figure 4.7.**).

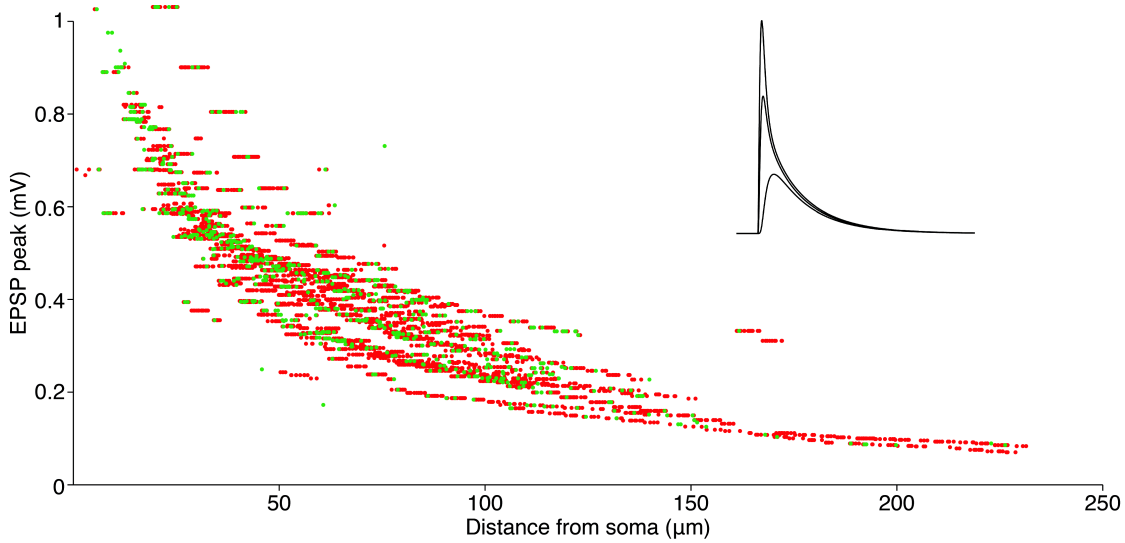

Figure 4.7. *Passive filtering by the model's dendrites results in strong voltage attenuation. Main panel: individual EPSP peaks measured at the soma resulting from a synaptic conductance injected into the compartmental model at the 4154 CC and 743 TC spine locations (green and red, respectively). Inset: three different EPSPs from proximal, intermediate and distal portions of the dendrites, showing progressively more temporal and amplitude filtering.*

On average the 743 simulated TC locations generated slightly higher amplitude EPSPs at the soma than the 4154 CC locations but this difference was

small (**Figure 4.8.**, CC median 0.390 mV; TC median 0.418 mV or 7.3% stronger, $p < 10^{-8}$, Wilcoxon signed-rank test). Therefore despite the moderate relative proximity of TC synapses, L4 neurons are either not sufficiently electrotonically compact, or the anatomical bias is not sufficiently pronounced, to explain the several-fold relative strength of TC inputs observed *in vitro*.

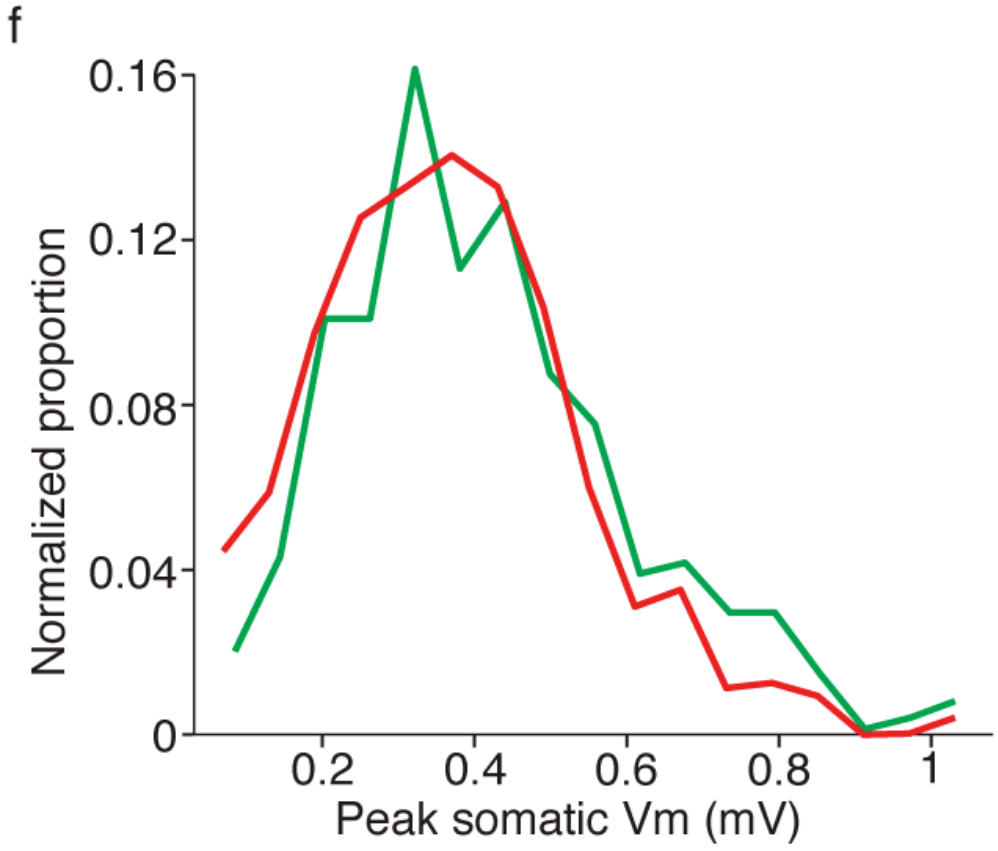

Figure 4.8. *Distribution of simulated somatic EPSP peaks for TC and CC inputs (same data as shown in* ***Figure 4.7.****).*

4.2. *In vivo* measurement of unitary TC and CC inputs

To test the model's prediction, we measured unitary TC and CC inputs in the living animal by adapting the "minimal stimulation" protocol developed for the acute slice preparation (Raastad, Storm et al. 1992, Stratford, Tarczy-Hornoch et al. 1996, Gil, Connors et al. 1999).

4.2.1. Selective activation of TC and CC fibers

To activate cortical axons originating from L4, we antidromically stimulated in Layer 2/3 (L2/3) at a depth of 300-350 μm within a 500-μm radius from the center of the barrel. Electrical stimuli here should activate L4 collaterals known to arborize in this location (Egger, Nevian et al. 2008) but not VPM axons, which typically do not arborize this superficially and horizontally distant to their target column (Oberlaender, Ramirez et al. 2012). Electrical stimuli here may activate axons originating from L2/3 and L5/6 cells, but these rarely form synapses in L4 (Bruno, Hahn et al. 2009, Lefort, Tomm et al. 2009).

To activate VPM fibers, we orthodromically stimulated in the white matter ~2000 μm below the pia (***Figure 4.9.*** white cross), centered on the barrel column, and adjusted the fine horizontal positioning to maximize the field EPSP response in L4. Shocks here should preferentially activate TC axons, which have lower stimulation thresholds than corticothalamic fibers. In addition the collaterals of

infragranular neurons rarely form synapses onto L4 excitatory neurons (Lefort, Tomm et al. 2009).

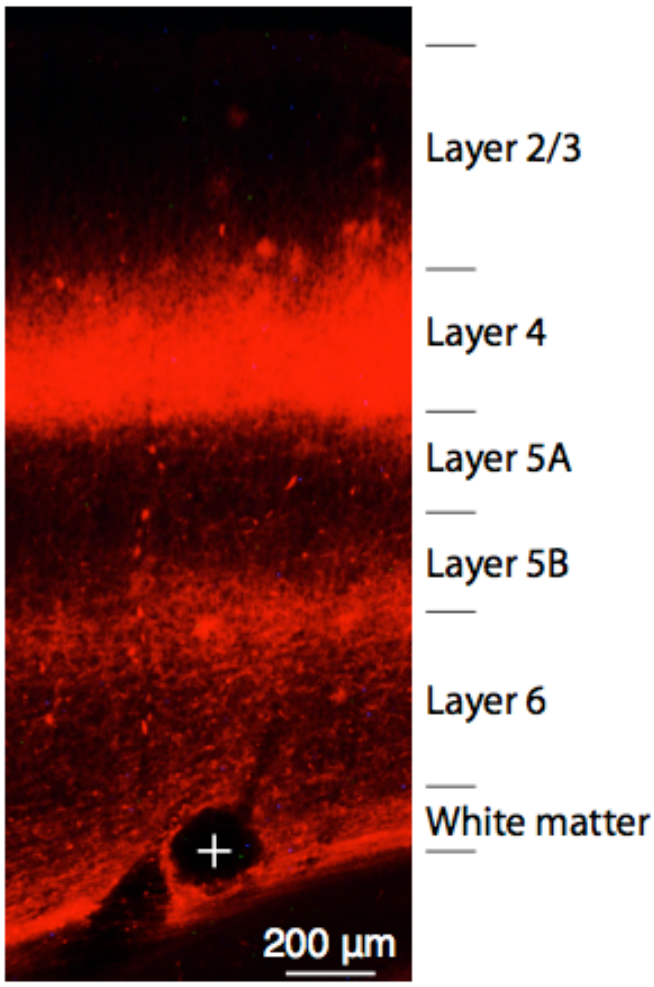

Figure 4.9. *Thalamocortical sections of barrel cortex three weeks after injection of ChR2-mCherry in VPM. The electrolytic lesion (white cross) was produced by targeting beneath the barrel column as described in the Methods and passing 10 µA of DC current for 10 s.*

We employed optogenetics to verify that electrical stimulation activates the desired TC-L4 or L4-L4 synapses. We injected VPM with a virus encoding

Channelrhodopsin2 (***Figure 4.9.***) and tested whether photo-activation of these fibers conditions the L4 field EPSP (fEPSP) elicited by electrical shock of the white matter.

In all animals we tested we found that the fEPSP evoked by electrical stimulation of the white matter was conditioned by photo-activation of VPM fibers 50 ms earlier (***Figure 4.10.*** left panel, n=3). Electrical stimulation in L2/3 was performed for two of these animals, but in neither case did photo-activation of VPM fibers condition the fEPSP evoked by presumed L4 collaterals (***Figure 4.10.*** right panel). Moreover, electrical stimulation of L2/3 could produce antidromic action potentials in L4 (***Figure 4.10.*** right panel, arrowhead). These results demonstrate that electrical stimulation of the white matter or L2/3 activates TC axons or L4 axons, respectively.

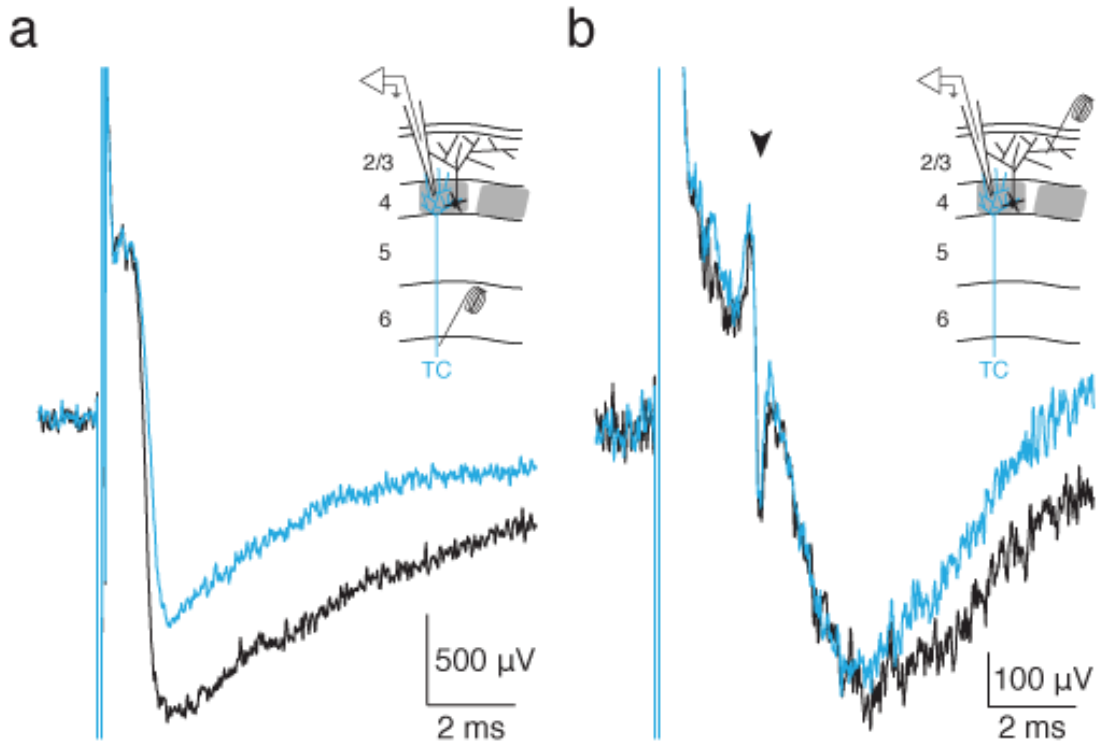

Figure 4.10. *Electrical stimulation permits selective thalamic or cortical fiber activation. Average fEPSP (n = 38 to 50 trials) in L4 evoked by electrical stimulation in adult animals. Black trace: control; blue trace: 50 ms after light activation of presynaptic fibers expressing ChR2. Insert: configuration of the recording and stimulation electrodes in a coronal view of S1; ChR2+ fibers indicated in blue. Left panel: ChR2 expression in VPM, electrical stimulation in white matter. Right panel: ChR2 expression in VPM, electrical stimulation in L2/3. Arrowhead: putative L4 multiunit activity following antidromic activation.*

4.2.2. Adapting minimal stimulation of TC and CC inputs to the intact preparation

Low-intensity stimulation resulted in all-or-none synaptic transmission in both juvenile and adult rats. Failures in transmission were clearly differentiable from successes despite the somewhat noisy membrane potential *in vivo* (***Figure 4.11.*** top left, stimulating thalamic fibers; ***Figure 4.11.*** bottom left, stimulating cortical fibers). Slightly reducing stimulus intensity from the level that produced 50% successful transmission (***Figure 4.11.*** top right, scatter plot, 2.55 V, ***Figure 4.11.*** bottom right, 9.75 V) resulted in complete failure. Moreover, varying the stimulus intensity did not alter the size or shape of evoked EPSPs. We fit a double-Gaussian function to the bimodal distribution of EPSP amplitudes produced by all-or-none activity (***Figure 4.11.*** right panels, histogram, black curve). Unitary EPSP size was calculated by subtracting the lower Gaussian's mean from the higher one, corresponding to those trials that resulted in successful synaptic transmission. The stimulation-EPSP onset latency was 2.22 msec ± 0.63 SD for TC inputs (n = 11) and 3.21 ± 0.84 SD for CC inputs (n = 9). Measurements in juvenile and adult animals did not differ significantly.

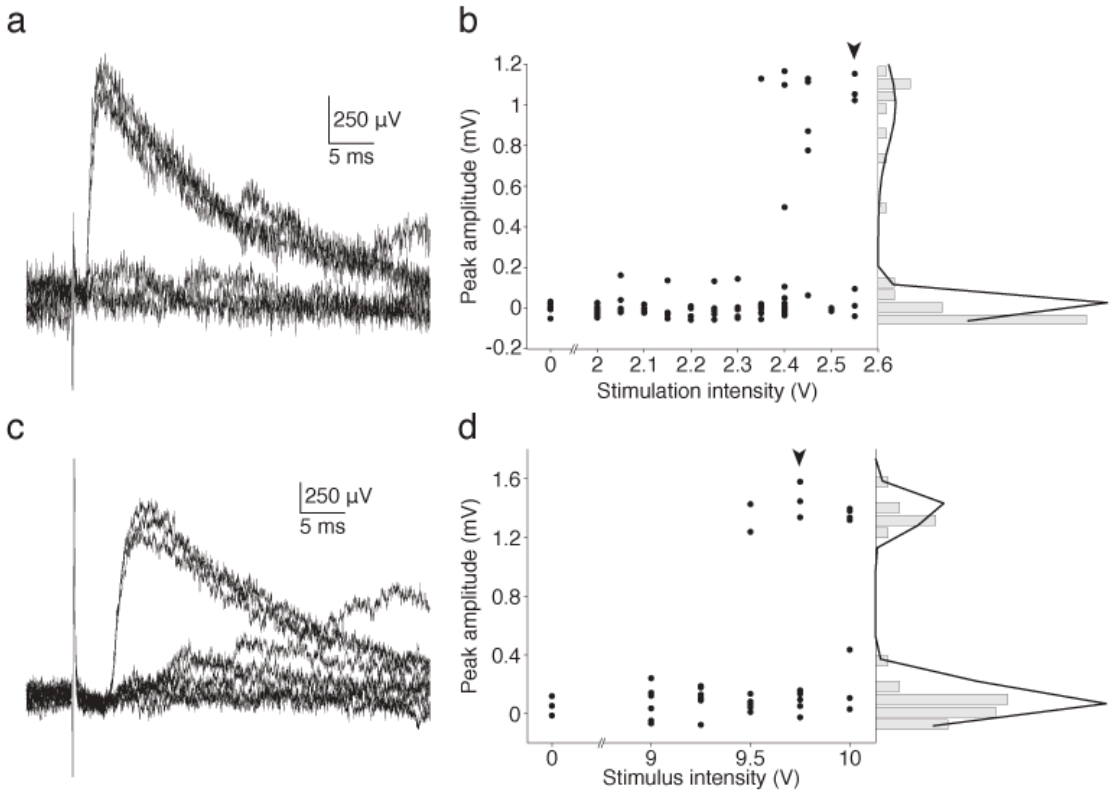

Figure 4.11. *Minimal stimulation* in vivo*. Top left: Somatic voltage recorded during seven trials of a L4 spiny stellate neuron, in response to an 2.55 V stimulus delivered to the white matter underneath the neuron's barrel column in an adult rat. The stimulus results in successful synaptic transmission 50% of the time. Top right: As the intensity of the stimulus is increased from 2 to 2.55 V (left), trials generated progressively more successes with relatively constant EPSP amplitude. Stimulus intensity was randomized during acquisition, but ordered in this plot for clarity. 0 indicates no stimulus; arrowhead indicates the stimulus intensity employed to obtain the traces shown in a. A histogram of the EPSP peak amplitude shows a bimodal distribution (right); black line indicates a fit using a double*

Gaussian function ($\mu1$ = 0.004 mV, $\sigma1$ = 0.047 mV, $\mu2$ = 1.00 mV, $\sigma2$ = 0.198 mV). Bottom panels same as for top panels, but in a young animal, stimulating in Layer 2/3. ($\mu1$ = 0.087 mV, $\sigma1$ = 0.102 mV, $\mu2$ = 1.383 mV, $\sigma2$ = 0.091 mV).

4.2.3. Short-term plasticity of TC and CC inputs

We observed short-term plasticity at these synapses using a paired-pulse protocol (**Figure 4.12.** left). EPSP strengths measured on individual trials revealed that the second pulse fails to result in synaptic transmission more often than the first, giving rise to a smaller average EPSP (**Figure 4.12.** middle). When stimulating twice at either 20 Hz, or 10 Hz to allow for complete decay of longer EPSPs, 100% of TC inputs exhibited short-term depression on average (mean EPSP2 to EPSP1 ratio = 0.74 ± 0.18 SD, n = 11). In contrast CC inputs showed a mix of short-term depression (44%) and facilitation (mean EPSP2 to EPSP1 ratio = 1.03, ± 0.36 SD, n = 9) (**Figure 4.12.** right).

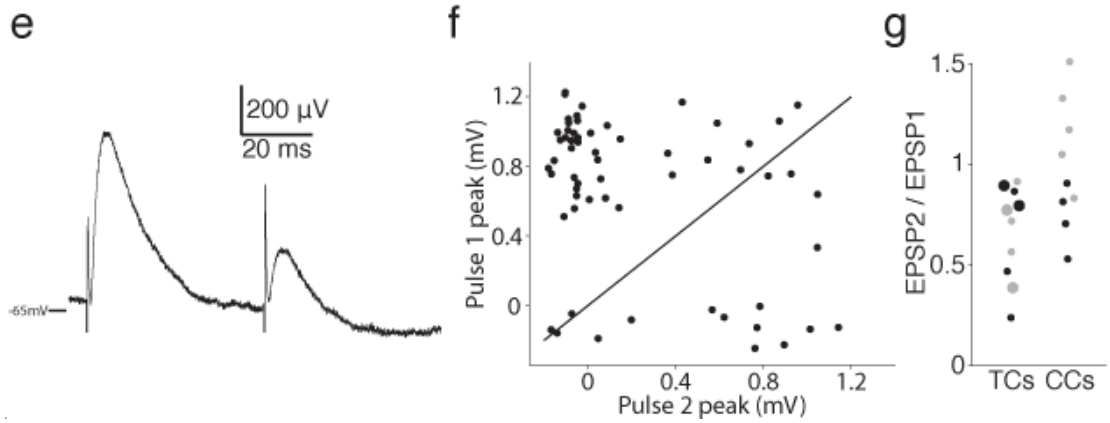

Figure 4.12. *Short-term plasticity of TC and CC inputs. Left panel: Paired pulses in white matter (20 Hz) reveal pronounced short-term depression (mean of 60 trials). Middle panel: EPSP peak amplitudes for both stimuli reveals either dual successes of synaptic transmission (top right quadrant), dual failures (bottom left quadrant), a preponderance of successes on the first stimulus only (top left quadrant), and a minority of successes on the second stimulus only (top right quadrant). Black line indicates identity. Right panel: EPSP2 / EPSP1 ratio for paired pulses at 20 Hz (large circles: 10 Hz) recorded in adult (black) and juvenile (grey) rats. Right panel: Summary of the unitary EPSP amplitudes recorded in adult (black) and juvenile (grey) rats. Lines indicate the means.*

4.2.4. Strength of TC and CC inputs

We found that the strengths of putative unitary TC and CC inputs *in vivo* were broadly similar (TC EPSPs mean = 0.63 mV ± 0.10 SEM, n = 11; CC EPSPs mean = 0.66 mV ± 0.16 SEM, n = 9; P = 0.85, t test; **Figure 4.13.**, black: adult, grey: juvenile). Thus, in agreement with the prediction from our model, and notwithstanding the anatomical configuration of TC versus CC inputs, we conclude that the TC synapses have no functional advantage over CC synapses.

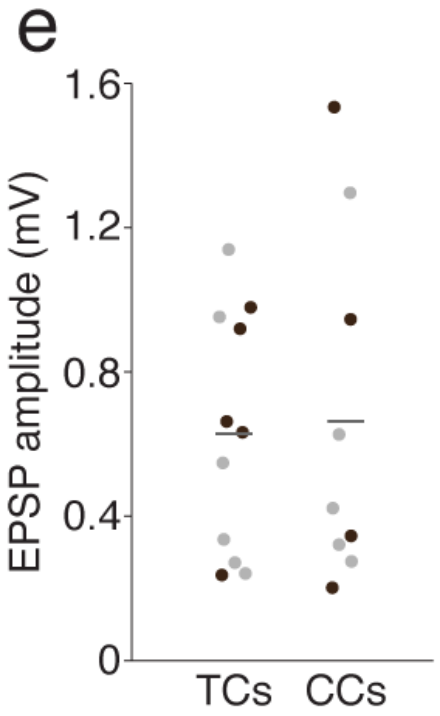

Figure 4.13. *Unitary TC and CC input strengths are comparable. Summary of the unitary EPSP amplitudes recorded in adult (black) and juvenile (grey) rats. Lines indicate the means.*

4.3. Methods

4.3.1. Animals

We used 6 juvenile (P16-21) and 12 adult (weight 167-235 grams) Wistar rats (Hilltop Laboratories, Charles River) for experiments.

4.3.2. *In vivo* preparation

As described in Chapter 3.

4.3.3. Whole-cell current clamp recordings

Patch pipettes were pulled from 2-mm filamented borosilicate glass. Tip inner diameter was ~0.75 μm. Pipettes were tip filled with 135 mM K-gluconate, 10 mM HEPES, 10 mM phosphocreatine-Na_2, 4 mM KCl, 4 mM ATP-Mg, 0.3 mM GTP, and 0.2% biocytin (pH 7.2). Cells were searched for in voltage-clamp mode. Whole-cell recordings were made in bridge mode using a MultiClamp 700B (Molecular Devices) for 20-60 min, digitized at 32 kHz. Pipette capacitance was neutralized immediately following break-in. Seal resistance was > 1 GΩ, series resistance 11-60MΩ, and spike height and overall Vm were stable throughout the recording. Series resistance was monitored following every trial and the bridge balance was adjusted accordingly. No holding current was applied. Mean input

resistance was 96.42 MΩ ± 49.64 SD.

4.3.4. Compartmental model

A compartmental model was constructed in NEURON (Carnevale and Hines 2006) based on the volumetric reconstruction of cell 6. The membrane potential recorded *in vivo* during pink noise (300-Hz cutoff) current injection was employed to fit three biophysical parameters in the model: specific membrane resistance (R_m = 6357.8 Ωcm^2), specific membrane capacitance (C_m = 2.967 μF/cm^2), and specific axial resistance (R_i = 500.5 Ωcm). An alpha synaptic conductance function was determined based on unitary CC synapse properties (EPSP peak, rise time, and decay time constant) measured from connected pairs *in vitro* (Feldmeyer, Egger et al. 1999): time to peak (tau = 0.7 ms), maximum conductance (g_{max} = 0.6 nS), reversal potential (e = 0 mV). That conductance was applied at each of the 743 TC and 4154 CC observed spine locations observed in the neuron's dendritic arbor, while the resulting simulated voltage change was recorded at the model's soma. The resulting simulated EPSP data was analyzed using custom-written routines in MATLAB.

4.3.5. Minimal Stimulation

Custom LabVIEW software was used to acquire data and inject current waveforms. We electrically stimulated fibers in the intact preparation by

positioning our recording and stimulating electrodes as in acute slice experiments. A bipolar concentric platinum/iridium 125 μm diameter electrode (FHC) was inserted vertically into the brain. Stimulus pulses (100 μs) were delivered using an A385 linear stimulus isolator (WPI). Stimulus intensity was randomized across trials to minimize effects due to potential changes in recording conditions or animal state. The location of the stimulation electrode was triangulated relative to the center of the barrel column. Cortical fibers were activated by stimulating in Layer 2/3, ~350 μm below the pia and superficial to the extent of thalamic fibers in somatosensory cortex (Oberlaender, Ramirez et al. 2012) and slightly (100-150 μm) caudal or rostral relative to the recording electrode to minimize the risk of them collision. TC fibers were stimulated by placing the bipolar electrode in the white matter ~2000 μm below the pia along the radial axis. While white matter stimulation is not guaranteed to activate thalamic fibers exclusively, our protocol is subject to this confound in equal measure as the *in vitro* protocol that it replicates. Placement was optimized by advancing the stimulation electrode while simultaneously applying electrical pulses and recording the resulting field EPSPs in the barrel.

During minimal stimulation, anesthesia was maintained at deep levels in order to minimize thalamic firing, cortical “up states”, and other spontaneous synaptic inputs. The criteria for minimal stimulation were as in (Gil, Connors et al. 1999): (1) all-or-none synaptic events, (2) little or no variation in EPSP latencies,

(3) a small change in the stimulus intensity did not change the mean size or shape of the EPSP, and (4) lowering stimulus intensities by 10-20% resulted in complete failure to evoke EPSPs.

Most analyzed cells were confirmed histologically as L4 excitatory barrel neurons. Three were not recovered but were classified as L4 excitatory barrel neurons based on the microdrive reading (between 786 and 818 μm below the pia), their intrinsic membrane properties (regular spiking, and the absence of "sag" during hyperpolarizing current injection) and receptive field properties (strong depolarization response to stimulating one whisker, and negligible depolarization to neighboring whiskers). Physiological data was analyzed using custom-written routines in MATLAB (MathWorks).

4.3.6. Optogenetics

To photo-activate VPM fibers, we injected VPM (as above) with a virus to drive expression of a ChR2-mCherry fusion protein driven by the CAG promoter (AAV1.CAG.hChR2(H134R)-mCherry.WPRE.SV40, Penn Vector). VPM was physiologically mapped, and volumes of 60-80 nl were injected over ~20 min using a Nanoject II auto-nanoliter injector (Drummond, Broomall, PA). The craniotomies were covered with bone wax post-injection and the incision closed with absorbable sutures. Animals were allowed to recover from surgery in a clean cage with softened food palettes and water overnight before returning to their

home cage.

These injections were performed in female ~70-100g rats. After housing the animals for ~3 weeks surgeries for physiology experiments were performed as described above (140-226 g). Light-activation of infected fibers was achieved by placing a 200-μm fiber optic immediately above the craniotomy and delivering 2-ms pulses of 473-nm light using a DPSS laser (OEM) (1.25-3.22 mW output from fiber) controlled by a mechanical shutter. Trials using light conditioning were interleaved with control trials.

Chapter 5

Discussion

5.1. Summary

We performed a comparative study of the anatomy and physiology of TC and CC synapses to address how activity in the thalamus transmits signals to cortex despite having several-fold fewer synaptic inputs. We found that, in spite of a subtle anatomical bias in their spatial distributions, TC and CC inputs influence the membrane potential of L4 barrel cortical neurons in approximately equal measure. We conclude that since these two classes of synapses are equivalent in strength, a relatively high TC efficacy cannot account for the thalamus' strong influence.

From a technical standpoint, several novel methods were developed in the course of this project:

1) Whole-dendrite mapping at single-spine resolution using LM. This resulted in the first such map and uncovered subtle anatomical biases heretofore

invisible to prior methods.

2) Correlative LM/EM strategy to assess the reliability of the LM method.

3) Detailed compartmental modeling using a current waveform of pink noise. This resulted in the first well-constrained biophysical model of an S1 L4 excitatory neuron.

4) Minimal stimulation *in vivo*. This resulted in the first measurements of TC and CC inputs on to S1 L4 excitatory neurons in an intact preparation.

5.2. Constructing detailed, reliable synaptic input maps

To our knowledge this is the first study to produce input maps of complete dendritic arbors at a single-synapse scale. The fraction of total spines we found to receive TC synapses (mean 9.98% ± 3.64% SD) is in line with estimates obtained using transmission electron microscopy from small segments of dendrites (13.9% (Benshalom and White 1986)). Ultrastructural examination of our putative light-level synaptic contacts indicates that 87% are true synapses (**Figure 3.8**). A false positive rate of 13% is tolerable for a number of purposes such as estimating a synapse type's total numbers or proximity along the dendrites to the soma.

Recently developed super-resolution light microscopy techniques may perfect our approach by improving lateral and axial resolution, thereby reducing the chance of false positives. Stochastic optical reconstruction microscopy (STORM) (Rust, Bates et al. 2006) has already been used to study the molecular

composition of synapses (Dani, Huang et al. 2010). Adapting this and other super-resolution methods to questions at the scale of complete dendritic arbors would require the capability to image large volumes, including in the Z dimension (i.e., > 300 x 300 x 300 μm) at reasonable time scales (a few days by our method). One promising avenue would be to apply deconvolution techniques to enhance the X-Y spatial resolution of array tomography imaging (Wang and Smith 2012), which already achieves high axial resolution by physical sectioning.

Prior studies have used brightfield microscopy to examine potential synaptic connectivity of labeled pre- and post-synaptic neurons. Correlative ultrastructural examination revealed, however, that brightfield microscopy suffers from high (~68%) false positive rates (da Costa and Martin 2011). The substantially lower false positive rate of our method is likely due to: (1) selective labeling of only synaptic markers (i.e. vesicle pools) rather than the entire cytosolic volume of thalamic axons, which drastically reduces chance non-synaptic contacts of pre- and post-synaptic signals, (2) imaging by confocal microscopy, which has inherently higher spatial resolution than brightfield, and (3) the use of linear deconvolution to reduce blurring caused by the point spread function.

Other methods to construct synapse-scale maps identify synapses functionally, rather than anatomically, such as by combining electrophysiology with two-photon calcium imaging *in vitro* (Richardson, Blundon et al. 2009, Little and Carter 2012, Macaskill, Little et al. 2012). Although calcium imaging ensures

the detection of functional synaptic contacts, it is not possible to construct comprehensive dendritic arbors due to the timescale of the protocol and the lifetime of *in vitro* recordings. Indeed, only a few synapses may be examined on a given dendritic arbor (Richardson, Blundon et al. 2009, Macaskill, Little et al. 2012), limiting this method's statistical power.

In addition, the inferior resolution of 2-photon microscopy, as compared to deconvolved confocal microscopy, renders it more difficult to distinguish between spine types such as stubby and mushroom. A more comprehensive method is subcellular channelrhodopsin-assisted circuit mapping (sCRACM) (Petreanu, Mao et al. 2009). However, the resolution of sCRACM, estimated at ~60 μm, does not permit detailed mapping at the level of individual spines. Clustering of synapses and subtle spatial biasing, such as that revealed by our study, would be difficult to detect by sCRACM.

We employed two strategies to label presynaptic structures of thalamic axon terminals, either viral-mediated expression of a synaptophysin-EGFP fusion protein or by taking advantage of the fact that VGluT2 antibodies predominantly label thalamic terminals in L4 (Fujiyama, Furuta et al. 2001, Nahmani and Erisir 2005, Graziano, Liu et al. 2008, Coleman, Nahmani et al. 2010) (and see Methods). The virus strategy is subject to the infection efficiency in the presynaptic population; since only 85-95% of thalamic neurons were infected, slight underestimations of the actual number of contacts are expected. Accounting

for incomplete infection would raise our estimate of TC synapses, for instance, from 10% to 11% of the total number axospinous contacts. Spatial distributions should however remain undistorted. By contrast, the immunohistological approach should be less biased with regard to total contact number.

In conclusion, our light-based method for mapping synaptic distributions is a scalable, generalizable and reliable strategy for mapping a neuron's complete dendritic arbor at the resolution of the synapse. The correlative LM-EM approach is also widely generalizable. The technology for these methods is within immediate reach of many neuroscience laboratories.

5.3. The distribution of thalamocortical inputs onto L4 neurons

On average TC synapses were found to be more proximal to the somata of excitatory L4 neurons than CC synapses. TC synapses were most prevalent within the first ~30 μm along the dendrites, after which their relative density dropped rapidly. This subtle bias is independent of the distribution of spine density along the dendritic arbor, which varies with regard to somatic proximity. It was observed in both spiny stellate cells and star pyramids, was independent of somatic location within the barrel, and cannot be predicted by the known anatomical distribution of TC axons.

A recent study in primary auditory cortex found that TC contacts are more prevalent on basal than apical dendrites and synapse more proximally on the apical trunk (Richardson, Blundon et al. 2009), as predicted by the laminar distribution of TC axons (Cruikshank, Rose et al. 2002, Smith, Uhlrich et al. 2012). No prominent spatial bias of TC synapses was reported within the basal compartments of auditory cortex neurons (Richardson, Blundon et al. 2009), but synapse detection by calcium imaging severely limits sample size. L4 of auditory cortex consists of true pyramidal neurons with extensive apical tufts (Smith and Populin 2001).

In contrast, the entire dendritic extent of the smaller spiny stellates found in L4 of somatosensory and visual cortex reside almost entirely in the dense arborization zone of TC axons, not just the area proximal to the soma. Our results

therefore cannot be explained simply by gross axonal anatomy. One possible way the asymmetry we uncovered could be achieved would be for VPM axons to complete their development earlier than cortical dendrites. Testing this hypothesis would require the careful study of the processes of single neurons over the course of S1 development.

The study in auditory cortex did reveal a preponderance of TC synapses onto stubby spines. We did not observe such a bias in our own data, which could reflect (1) differences in cortical areas and cell types, (2) the relative difficulty in distinguishing stubby and mushroom spines under two-photon, relative to deconvolved confocal, imaging, (3) our method's sampling of two orders of magnitude more spines per cell, and/or (4) changes in spine morphology induced by slicing (Kirov, Sorra et al. 1999).

A recent study implicates dendritic spikes in the generation of whisker direction preference in L4 barrel excitatory neurons (Lavzin, Rapoport et al. 2012). Spatiotemporal coincidence of synaptic inputs is one mechanism by which dendritic spikes can be initiated (London and Hausser 2005). And direction preference in the somatosensory system (Bruno and Sakmann 2006), and orientation preference in the visual system (Reid and Alonso 1995, Ferster, Chung et al. 1996), are strongly determined by thalamocortical innervation. However, we did not find evidence of clustering by TC inputs, and conclude that the anatomy of the thalamocortical innervation, on its own, does not appear to be configured to

promote these dendritic events.

5.4. Strength of TC and CC input

5.4.1. Effect of dendritic filtering on synaptic integration

Decreased filtering expected from proximal TC locations along the dendrites has been proposed as a mechanism for the pronounced TC efficacy encountered *in vitro* (Richardson, Blundon et al. 2009). Yet our compartmental model predicts that the strength of TC versus CC synapses, when measured at the soma and assuming equal conductance, is only marginally augmented, even though our model is less electrotonically compact than a previous biophysical model of this cell type (Segev, Friedman et al. 1995). We conclude that L4 cells are either not sufficiently electrotonically compact, or the anatomical bias is insufficiently pronounced, to explain the marked difference in the strength of these two classes of synapses. Our *in vivo* minimal stimulation experiments confirm the model's prediction, revealing that TC and CC synapses are similar in strength.

Our compartmental model contrasts in several respects with a previously published model of this same cell type (**Figure 5.1.**) (Segev and London 2000). Most notably, the previous model recorded a less pronounced attenuation of EPSP magnitude as distance from the soma increased. The previous model modeled the effect of spine heads and spine necks (ours did not); it did not employ physiological data to constrain the biophysical parameters (ours did); and because

it was based on a volumetric reconstruction produced using serial-section TEM, it was only of a limited section of the dendrite—one of the results of which was that it exhibited an extraordinarily high input resistance (540-660 MΩ, depending on the parameters).

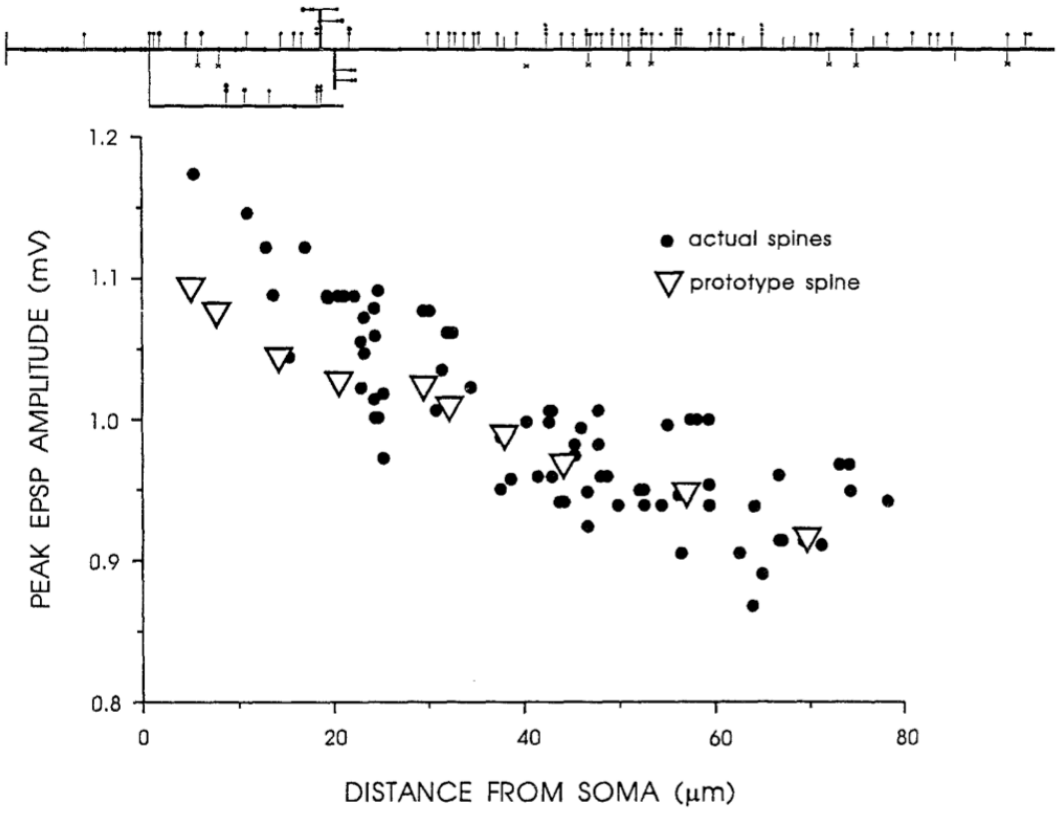

Figure 5.1. *Voltage attenuation of EPSPs in a previous model of L4 dendrites. Top: Diagram of the reconstruction portion of the dendrite and dendritic spines, that provided the morphological for a compartmental model. Bottom: voltage*

attenuation as a function of distance from the soma for the 75 modeled synapses is not very pronounced. Figure from (Segev and London 2000).

5.4.2. Unitary measurements of TC and CC synapse strength

To our knowledge, this is the first study to compare TC and CC synaptic strengths side-by-side *in vivo*. While TC inputs are weaker when measured *in vivo* than *in vitro* (Bruno and Sakmann 2006), the relative strength of TC and CC synapses in the living animal has remained unknown. Moreover, the prior *in vivo* estimate of TC synapse strength required averaging post-synaptic membrane potential under conditions of elevated thalamic firing rates induced by sensory stimulation, potentially limiting measurement to partially depressed TC synapses. The minimal stimulation technique used here requires no sensory stimulus and measures EPSPs on a single-spike basis, eliminating the potential confound of synaptic depression due to sustained thalamic activity during whisker stimulation.

Although it is impossible be certain about the identity of the fibers we stimulated, the *in vivo* protocol replicates the electrode placement of the *in vitro* protocols that have produced the dataset we are comparing ours to. The recorded short-term plasticity characteristics of TC and CC inputs (universal shot-term-depression, and a mixture of depression and facilitation, respectively) agree

qualitatively with those observed *in vitro*—one of the criteria for distinguishing these two classes of synapses.

Moreover, given that thalamocortical fibers extend only to lower L3 (Wimmer, Bruno et al. 2010), stimulating in upper L2/3 should not recruit those axons. It cannot be ruled out that stimulating in the white matter below the barrel column might have recruited L6 fibers that send collaterals to L4 excitatory neurons. However, very few L4 neurons project to L4; indeed, the connection probability is extremely low (one *in vitro* study (Lefort, Tomm et al. 2009) that reported 94 L6/L4 simultaneously recorded pairs of excitatory neurons did not find a single L6 to L4 connection).

Many parameters, such as altered intrinsic membrane properties, neuromodulatory environment, and circuit dynamics, could explain the *in vivo* and *in vitro* difference of TC synapses. Alternatively, low *in vivo* calcium concentration relative to traditional *in vitro* preparations (Borst 2010) could skew measurements of these synaptic properties. These factors could have impacted all synapse types equivalently *in vitro* resulting in a several-fold advantage of TC connections, but our study reveals that no such TC advantage exists in the living animal. The different release probabilities, synaptic dynamics, and VGluT isoforms of these synaptic classes observed *in vitro*, therefore, may reflect the evolution of distinct biophysical mechanisms to support the relatively higher firing

rates of thalamic neurons (Bruno and Sakmann 2006, Voigt, Brecht et al. 2008) rather than a difference in synaptic efficacy.

5.5. Implications for the propagation of information from thalamus to cortex

TC synapses are no stronger than CC synapses, which outnumber them ten to one, yet sensory stimuli depolarize L4 substantially. What alternative mechanisms could overcome this anatomical disadvantage?

TC convergence is high for excitatory neurons in L4, which each receive connections from as many ~90 thalamic neurons (Reid and Alonso 1995, Bruno and Sakmann 2006). Sensory stimuli synchronize neurons in the VPM to varying degrees on millisecond timescales (Alonso, Usrey et al. 1996, Temereanca and Simons 2003, Bruno and Sakmann 2006, Wang, Webber et al. 2010, Oberlaender, Ramirez et al. 2012), a phenomenon also observed in the cat lateral geniculate nucleus (LGN) (Alonso, Usrey et al. 1996, Stanley, Jin et al. 2012). Convergent, synchronous input may be necessary to activate L4, given that individual thalamocortical neurons depolarize the postsynaptic neuron by only ~0.5 mV. Thus TC synapses are both sufficiently convergent and synchronously active to powerfully influence cortical activity (Bruno 2011).

In addition, potent short-latency feed-forward inhibition in the cortex creates a tight window for integration of excitatory inputs onto neurons (Pouille

and Scanziani 2001, Bruno and Simons 2002, Wehr and Zador 2003, Wilent and Contreras 2005). Rapid changes in presynaptic firing rate and/or synchrony could be sufficient to produce substantial postsynaptic depolarization within that window, and permit a relatively small number of excitatory synapses to temporarily dominate the total flow of excitatory drive in the cortical network. Indeed, for networks in which excitation and inhibition are balanced, such large, fast changes in the rate of the presynaptic population are sufficient to transiently affect the state of the postsynaptic network (Vogels and Abbott 2009).

More generally, feed-forward inhibition in the cortex might sufficiently dampen recurrent excitation such that despite vigorous corticocortical excitatory drive, the global influence of excitatory cortical inputs following thalamic excitation could be counteracted by a proportionally strong inhibitory conductance.

Finally, although likely not a sufficient explanation on its own, both spontaneous and sensory-evoked firing rates are higher in the thalamus than in the cortex (Simons and Carvell 1989, Brecht and Sakmann 2002, Brecht and Sakmann 2002, Bruno and Simons 2002). Therefore, the fraction of total excitation contributed by the thalamus might approach or exceed that provided by the cortex, even though thalamic excitation is transmitted across fewer synapses.

5.6. Determining the precise mechanism of propagation

Future experiments manipulating the synchrony and the firing rate of the presynaptic population independently of one another will be required to determine the relative contribution of the mechanisms outlined above. This has previously been attempted via indirect means: there is a stronger relationship between the velocity of whisker stimulation and the synchrony of thalamic responses, rather than their firing rate (**Figure 5.2.**) (Pinto, Brumberg et al. 2000). By applying stimuli of different velocities, it was observed that the cortical spiking response correlates better with thalamic synchrony than with firing rate.

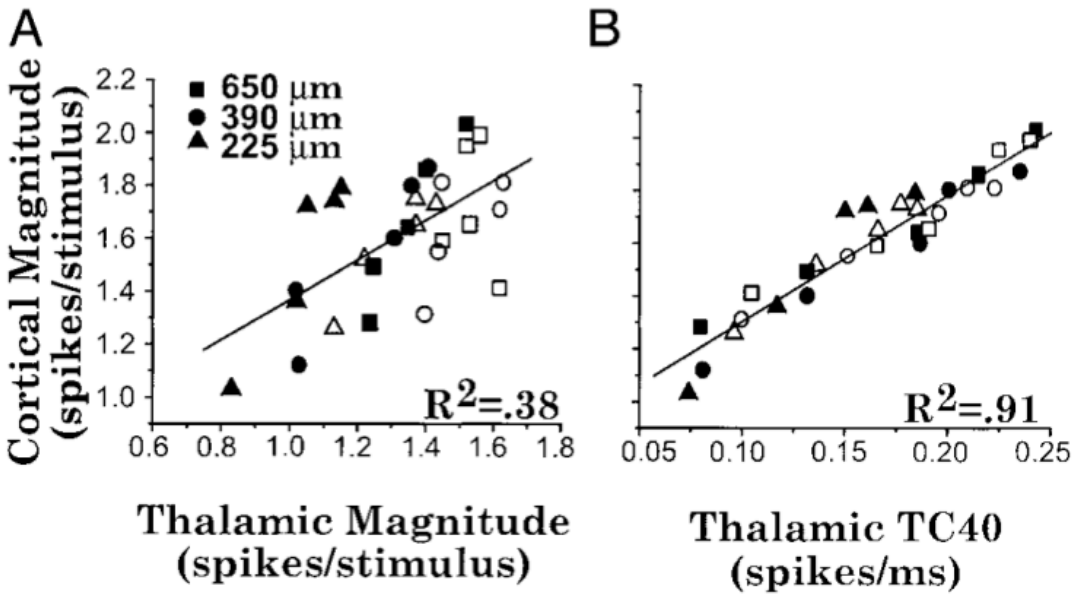

Figure 5.2. *Synchrony in thalamus determines cortical response. The cortical response is better predicted by thalamic synchrony (right) than thalamic spike rate (left). The temporal contrast metric ("TC40") is an indirect measure of synchrony, defined as the average firing rate during the time window it took to produce 40%*

of the sensory-evoked spikes. This plot accounts deflections at 5 different velocities and 3 different amplitudes (square, circle and triangle symbols), for a total of 30 different conditions. Open symbols: preferred direction of whisker deflection; closed symbols: caudal whisker deflection. Figure adapted from (Pinto, Brumberg et al. 2000).

However, in this experiment rate and synchrony are not fully decoupled rendering conclusive interpretation difficult. Moreover, the temporal contrast measure, used as a proxy for synchrony in the absence of simultaneously recorded population spike trains, is sensitive both to synchrony and rapid changes in firing rate without a change in synchrony beyond that determined by an elevated firing rate. Further, while relatively less correlated with cortical activity, thalamic firing rate clearly has a strong influence. The ideal experiment would on the one hand maintain rate constant while varying synchrony, and on the other hand maintain synchrony constant while varying rate.

The advent of optogenetic tools (Fenno, Yizhar et al. 2011) might prove useful in developing an improved protocol for manipulating synchrony and firing rate independently of one another. Stimulating thalamic neurons directly using Channelrhodopsin2 (Boyden, Zhang et al. 2005) would likely be too crude of a strategy to test the rate-synchrony parameter space. Instead, it might be possible to effect the necessary degree of control by inhibiting VPM using Channelrhodopsin2

delivered to the thalamic reticular nucleus (TRN) during sensory stimulation using varying amounts of velocity. The TRN forms a powerful inhibitory projection to first-order thalamic nuclei (Jones 1975, Houser, Vaughn et al. 1980, Lee, Friedberg et al. 1994) and could be exploited to modulate VPM firing rate tonically without affecting synchrony.

Finally, it would be instructive to distinguish between excitatory and inhibitory cortical neurons, which display vastly different intrinsic membrane and thalamic innervation properties, both pre- and postsynaptically (Hull, Isaacson et al. 2009, Bagnall, Hull et al. 2011). The effects of presynaptic firing rate and synchrony in interneurons might result in specific patterns of activation at the single-cell level, which could affect the cortical network's overall response.

References

Abbe, E. (1873). "Beiträge zur Theorie des Mikroskops und der mikroskopischen Wahrnehmung." Archiv für mikroskopische Anatomie **9**(1): 413-418.

Ahmed, B., J. C. Anderson, R. J. Douglas, K. A. Martin and J. C. Nelson (1994). "Polyneuronal innervation of spiny stellate neurons in cat visual cortex." J Comp Neurol **341**(1): 39-49.

Alonso, J. M., W. M. Usrey and R. C. Reid (1996). "Precisely correlated firing in cells of the lateral geniculate nucleus." Nature **383**(6603): 815-819.

Bagnall, M. W., C. Hull, E. A. Bushong, M. H. Ellisman and M. Scanziani (2011). "Multiple clusters of release sites formed by individual thalamic afferents onto cortical interneurons ensure reliable transmission." Neuron **71**(1): 180-194.

Bates, M., B. Huang, G. T. Dempsey and X. Zhuang (2007). "Multicolor super-resolution imaging with photo-switchable fluorescent probes." Science **317**(5845): 1749-1753.

Benshalom, G. and E. L. White (1986). "Quantification of thalamocortical synapses with spiny stellate neurons in layer IV of mouse somatosensory cortex." J Comp Neurol **253**(3): 303-314.

Betzig, E., G. H. Patterson, R. Sougrat, O. W. Lindwasser, S. Olenych, J. S. Bonifacino, M. W. Davidson, J. Lippincott-Schwartz and H. F. Hess (2006). "Imaging intracellular fluorescent proteins at nanometer resolution." Science **313**(5793): 1642-1645.

Bock, D. D., W. C. Lee, A. M. Kerlin, M. L. Andermann, G. Hood, A. W. Wetzel, S. Yurgenson, E. R. Soucy, H. S. Kim and R. C. Reid (2011). "Network anatomy and in vivo physiology of visual cortical neurons." Nature **471**(7337): 177-182.

Borst, J. G. (2010). "The low synaptic release probability in vivo." Trends Neurosci **33**(6): 259-266.

Boyd, I. A. and A. R. Martin (1956). "The end-plate potential in mammalian muscle." J Physiol **132**(1): 74-91.

Boyden, E. S., F. Zhang, E. Bamberg, G. Nagel and K. Deisseroth (2005). "Millisecond-timescale, genetically targeted optical control of neural activity." Nat Neurosci **8**(9): 1263-1268.

Brecht, M. and B. Sakmann (2002). "Dynamic representation of whisker deflection by synaptic potentials in spiny stellate and pyramidal cells in the barrels and septa of layer 4 rat somatosensory cortex." J Physiol **543**(Pt 1): 49-70.

Brecht, M. and B. Sakmann (2002). "Whisker maps of neuronal subclasses of the rat ventral posterior medial thalamus, identified by whole-cell voltage recording and morphological reconstruction." J Physiol **538**(Pt 2): 495-515.

Briggman, K. L. and D. D. Bock (2012). "Volume electron microscopy for neuronal circuit reconstruction." Curr Opin Neurobiol **22**(1): 154-161.

Briggman, K. L. and W. Denk (2006). "Towards neural circuit reconstruction with volume electron microscopy techniques." Curr Opin Neurobiol **16**(5): 562-570.

Briggman, K. L., M. Helmstaedter and W. Denk (2011). "Wiring specificity in the direction-selectivity circuit of the retina." Nature **471**(7337): 183-188.

Bruno, R. M. (2011). "Synchrony in sensation." Curr Opin Neurobiol **21**(5): 701-708.

Bruno, R. M., T. T. Hahn, D. J. Wallace, C. P. de Kock and B. Sakmann (2009). "Sensory experience alters specific branches of individual corticocortical axons during development." J Neurosci **29**(10): 3172-3181.

Bruno, R. M. and B. Sakmann (2006). "Cortex is driven by weak but synchronously active thalamocortical synapses." Science **312**(5780): 1622-1627.

Bruno, R. M. and D. J. Simons (2002). "Feedforward mechanisms of excitatory and inhibitory cortical receptive fields." J Neurosci **22**(24): 10966-10975.

Cardona, A., S. Saalfeld, J. Schindelin, I. Arganda-Carreras, S. Preibisch, M. Longair, P. Tomancak, V. Hartenstein and R. J. Douglas (2012). "TrakEM2 software for neural circuit reconstruction." PLoS One **7**(6): e38011.

Carnevale, N. T. and M. L. Hines (2006). The NEURON book. Cambridge, UK ; New York, Cambridge University Press,.

Coleman, J. E., M. Nahmani, J. P. Gavornik, R. Haslinger, A. J. Heynen, A. Erisir and M. F. Bear (2010). "Rapid structural remodeling of thalamocortical synapses parallels experience-dependent functional plasticity in mouse primary visual cortex." J Neurosci **30**(29): 9670-9682.

Conchello, J. A. and J. W. Lichtman (2005). "Optical sectioning microscopy." Nat Methods **2**(12): 920-931.

Cruikshank, S. J., H. J. Rose and R. Metherate (2002). "Auditory thalamocortical synaptic transmission in vitro." J Neurophysiol **87**(1): 361-384.

Cruikshank, S. J., H. Urabe, A. V. Nurmikko and B. W. Connors (2010). "Pathway-specific feedforward circuits between thalamus and neocortex revealed by selective optical stimulation of axons." Neuron **65**(2): 230-245.

da Costa, N. M. and K. A. Martin (2011). "How thalamus connects to spiny stellate cells in the cat's visual cortex." J Neurosci **31**(8): 2925-2937.

Dani, A., B. Huang, J. Bergan, C. Dulac and X. Zhuang (2010). "Superresolution imaging of chemical synapses in the brain." Neuron **68**(5): 843-856.

De Robertis, E. D. and H. S. Bennett (1955). "Some features of the submicroscopic morphology of synapses in frog and earthworm." J Biophys Biochem Cytol **1**(1): 47-58.

Del Castillo, J. and B. Katz (1954). "Quantal components of the end-plate potential." J Physiol **124**(3): 560-573.

Denk, W. and H. Horstmann (2004). "Serial block-face scanning electron microscopy to reconstruct three-dimensional tissue nanostructure." PLoS Biol **2**(11): e329.

Ding, J. B., K. T. Takasaki and B. L. Sabatini (2009). "Supraresolution imaging in brain slices using stimulated-emission depletion two-photon laser scanning microscopy." Neuron **63**(4): 429-437.

Egger, V., T. Nevian and R. M. Bruno (2008). "Subcolumnar dendritic and axonal organization of spiny stellate and star pyramid neurons within a barrel in rat somatosensory cortex." Cereb Cortex **18**(4): 876-889.

Feldmeyer, D., V. Egger, J. Lubke and B. Sakmann (1999). "Reliable synaptic connections between pairs of excitatory layer 4 neurones within a single 'barrel' of developing rat somatosensory cortex." J Physiol **521 Pt 1**: 169-190.

Fenno, L., O. Yizhar and K. Deisseroth (2011). "The development and application of optogenetics." Annu Rev Neurosci **34**: 389-412.

Ferster, D., S. Chung and H. Wheat (1996). "Orientation selectivity of thalamic input to simple cells of cat visual cortex." Nature **380**(6571): 249-252.

Franks, K. M. and J. S. Isaacson (2006). "Strong single-fiber sensory inputs to olfactory cortex: implications for olfactory coding." Neuron **49**(3): 357-363.

Franks, K. M., M. J. Russo, D. L. Sosulski, A. A. Mulligan, S. A. Siegelbaum and R. Axel (2011). "Recurrent circuitry dynamically shapes the activation of piriform cortex." Neuron **72**(1): 49-56.

Fujiyama, F., T. Furuta and T. Kaneko (2001). "Immunocytochemical localization of candidates for vesicular glutamate transporters in the rat cerebral cortex." J Comp Neurol **435**(3): 379-387.

Gentet, L. J., M. Avermann, F. Matyas, J. F. Staiger and C. C. Petersen (2010). "Membrane potential dynamics of GABAergic neurons in the barrel cortex of behaving mice." Neuron **65**(3): 422-435.

Gil, Z., B. W. Connors and Y. Amitai (1999). "Efficacy of thalamocortical and intracortical synaptic connections: quanta, innervation, and reliability." Neuron **23**(2): 385-397.

Goldstein, J. (2003). Scanning electron microscopy and x-ray microanalysis. New York, Kluwer Academic/Plenum Publishers.

Graziano, A., X. B. Liu, K. D. Murray and E. G. Jones (2008). "Vesicular glutamate transporters define two sets of glutamatergic afferents to the somatosensory thalamus and two thalamocortical projections in the mouse." J Comp Neurol **507**(2): 1258-1276.

Gustafsson, M. G. (2005). "Nonlinear structured-illumination microscopy: wide-field fluorescence imaging with theoretically unlimited resolution." Proc Natl Acad Sci U S A **102**(37): 13081-13086.

Harris, K. M., E. Perry, J. Bourne, M. Feinberg, L. Ostroff and J. Hurlburt (2006). "Uniform serial sectioning for transmission electron microscopy." J Neurosci **26**(47): 12101-12103.

Hayworth, K. J., N. Kasthuri, R. Schalek and J. W. Lichtman (2006). "Automating the Collection of Ultrathin Serial Sections for Large Volume TEM Reconstructions." Microscopy and Microanalysis **12**(Supplement S02): 86-87.

Heintzmann, R., T. M. Jovin and C. Cremer (2002). "Saturated patterned excitation microscopy--a concept for optical resolution improvement." J Opt Soc Am A Opt Image Sci Vis **19**(8): 1599-1609.

Hell, S. W. and J. Wichmann (1994). "Breaking the diffraction resolution limit by stimulated emission: stimulated-emission-depletion fluorescence microscopy." Opt Lett **19**(11): 780-782.

Hess, S. T., T. P. Girirajan and M. D. Mason (2006). "Ultra-high resolution imaging by fluorescence photoactivation localization microscopy." Biophys J **91**(11): 4258-4272.

Heymann, J. A., M. Hayles, I. Gestmann, L. A. Giannuzzi, B. Lich and S. Subramaniam (2006). "Site-specific 3D imaging of cells and tissues with a dual beam microscope." J Struct Biol **155**(1): 63-73.

Hines, M. L. and N. T. Carnevale (1997). "The NEURON simulation environment." Neural Comput **9**(6): 1179-1209.

Houser, C. R., J. E. Vaughn, R. P. Barber and E. Roberts (1980). "GABA neurons are the major cell type of the nucleus reticularis thalami." Brain Res **200**(2): 341-354.

Hull, C., J. S. Isaacson and M. Scanziani (2009). "Postsynaptic mechanisms govern the differential excitation of cortical neurons by thalamic inputs." J Neurosci **29**(28): 9127-9136.

Jack, J. J. B., D. Noble and R. W. Tsien (1975). Electric current flow in excitable cells. Oxford, Clarendon Press.

Jones, E. G. (1975). "Some aspects of the organization of the thalamic reticular complex." J Comp Neurol **162**(3): 285-308.

Jones, E. G. and I. T. Diamond (1995). The barrel cortex of rodents. New York, Plenum Press.

Katz, B. (1969). The release of neural transmitter substances. Liverpool, Liverpool University Press.

Kirov, S. A., K. E. Sorra and K. M. Harris (1999). "Slices have more synapses than perfusion-fixed hippocampus from both young and mature rats." J Neurosci **19**(8): 2876-2886.

Klar, T. A., S. Jakobs, M. Dyba, A. Egner and S. W. Hell (2000). "Fluorescence microscopy with diffraction resolution barrier broken by stimulated emission." Proc Natl Acad Sci U S A **97**(15): 8206-8210.

Knott, G., H. Marchman, D. Wall and B. Lich (2008). "Serial section scanning electron microscopy of adult brain tissue using focused ion beam milling." J Neurosci **28**(12): 2959-2964.

Land, P. W., S. A. Buffer, Jr. and J. D. Yaskosky (1995). "Barreloids in adult rat thalamus: three-dimensional architecture and relationship to somatosensory cortical barrels." J Comp Neurol **355**(4): 573-588.

Lavzin, M., S. Rapoport, A. Polsky, L. Garion and J. Schiller (2012). "Nonlinear dendritic processing determines angular tuning of barrel cortex neurons in vivo." Nature **490**(7420): 397-401.

Lee, S. M., M. H. Friedberg and F. F. Ebner (1994). "The role of GABA-mediated inhibition in the rat ventral posterior medial thalamus. I. Assessment of receptive field changes following thalamic reticular nucleus lesions." J Neurophysiol **71**(5): 1702-1715.

Lefort, S., C. Tomm, J. C. Floyd Sarria and C. C. Petersen (2009). "The excitatory neuronal network of the C2 barrel column in mouse primary somatosensory cortex." Neuron **61**(2): 301-316.

Lichtman, J. W. and W. Denk (2011). "The big and the small: challenges of imaging the brain's circuits." Science **334**(6056): 618-623.

Little, J. P. and A. G. Carter (2012). "Subcellular synaptic connectivity of layer 2 pyramidal neurons in the medial prefrontal cortex." J Neurosci **32**(37): 12808-12819.

London, M. and M. Hausser (2005). "Dendritic computation." Annu Rev Neurosci **28**: 503-532.

London, M., A. Schreibman, M. Hausser, M. E. Larkum and I. Segev (2002). "The information efficacy of a synapse." Nat Neurosci **5**(4): 332-340.

London, M. and I. Segev (2001). "Synaptic scaling in vitro and in vivo." Nat Neurosci **4**(9): 853-855.

Lorente de Nó, R. (1922). "La corteza cerebral del raton." Trab. Lab. Invest. Biol. (Madrid) **20**: 41-78.

Lu, J. and J. W. Lichtman (2007). "Imaging the neuromuscular junction over the past centuries." Sheng Li Xue Bao **59**(6): 683-696.

Lubke, J. and D. Feldmeyer (2007). "Excitatory signal flow and connectivity in a cortical column: focus on barrel cortex." Brain Struct Funct **212**(1): 3-17.

Macaskill, A. F., J. P. Little, J. M. Cassel and A. G. Carter (2012). "Subcellular connectivity underlies pathway-specific signaling in the nucleus accumbens." Nat Neurosci **15**(12): 1624-1626.

Magee, J. C. (1999). "Dendritic lh normalizes temporal summation in hippocampal CA1 neurons." Nat Neurosci **2**(6): 508-514.

Magee, J. C. and E. P. Cook (2000). "Somatic EPSP amplitude is independent of synapse location in hippocampal pyramidal neurons." Nat Neurosci **3**(9): 895-903.

McGuire, B. A., J. P. Hornung, C. D. Gilbert and T. N. Wiesel (1984). "Patterns of synaptic input to layer 4 of cat striate cortex." J Neurosci **4**(12): 3021-3033.

Miller, J. P., W. Rall and J. Rinzel (1985). "Synaptic amplification by active membrane in dendritic spines." Brain Res **325**(1-2): 325-330.

Minsky, M. (1961). "US Patent No. 3,013,467." Washington, DC: U.S. Patent and Trademark Office.

Minsky, M. (1988). "Memoir on inventing the confocal scanning microscope." Scanning **10**(4): 128-138.

Nahmani, M. and A. Erisir (2005). "VGluT2 immunochemistry identifies thalamocortical terminals in layer 4 of adult and developing visual cortex." J Comp Neurol **484**(4): 458-473.

Oberlaender, M., A. Ramirez and R. M. Bruno (2012). "Sensory experience restructures thalamocortical axons during adulthood." Neuron **74**(4): 648-655.

Okun, M. and I. Lampl (2008). "Instantaneous correlation of excitation and inhibition during ongoing and sensory-evoked activities." Nat Neurosci **11**(5): 535-537.

Palade, G. E. and S. L. Palay (1954). "Electron microscope observations of interneuronal and neuromuscular synapses." Anatomical Record **118**: 335–336.

Peters, A. and E. G. Jones (1984). Cerebral cortex. New York, Plenum Press.

Peters, A. and I. R. Kaiserman-Abramof (1970). "The small pyramidal neuron of the rat cerebral cortex. The perikaryon, dendrites and spines." Am J Anat **127**(4): 321-355.

Peters, A. and B. R. Payne (1993). "Numerical relationships between geniculocortical afferents and pyramidal cell modules in cat primary visual cortex." Cereb Cortex **3**(1): 69-78.

Petreanu, L., T. Mao, S. M. Sternson and K. Svoboda (2009). "The subcellular organization of neocortical excitatory connections." Nature **457**(7233): 1142-1145.

Pinto, D. J., J. C. Brumberg and D. J. Simons (2000). "Circuit dynamics and coding strategies in rodent somatosensory cortex." J Neurophysiol **83**(3): 1158-1166.

Pouille, F. and M. Scanziani (2001). "Enforcement of temporal fidelity in pyramidal cells by somatic feed-forward inhibition." Science **293**(5532): 1159-1163.

Raastad, M., J. F. Storm and P. Andersen (1992). "Putative Single Quantum and Single Fibre Excitatory Postsynaptic Currents Show Similar Amplitude Range and Variability in Rat Hippocampal Slices." Eur J Neurosci **4**(1): 113-117.

Rall, W. (1962). "Electrophysiology of a dendritic neuron model." Biophys J **2**(2 Pt 2): 145-167.

Rall, W. and J. Rinzel (1973). "Branch input resistance and steady attenuation for input to one branch of a dendritic neuron model." Biophys J **13**(7): 648-687.

Ramón y Cajal, S. (1995). Histology of the nervous system of man and vertebrates. New York, Oxford University Press.

Reid, R. C. and J. M. Alonso (1995). "Specificity of monosynaptic connections from thalamus to visual cortex." Nature **378**(6554): 281-284.

Richardson, R. J., J. A. Blundon, I. T. Bayazitov and S. S. Zakharenko (2009). "Connectivity patterns revealed by mapping of active inputs on dendrites of thalamorecipient neurons in the auditory cortex." J Neurosci **29**(20): 6406-6417.

Rinzel, J. and W. Rall (1974). "Transient response in a dendritic neuron model for current injected at one branch." Biophys J **14**(10): 759-790.

Rust, M. J., M. Bates and X. Zhuang (2006). "Sub-diffraction-limit imaging by stochastic optical reconstruction microscopy (STORM)." Nat Methods **3**(10): 793-795.

Schindelin, J., I. Arganda-Carreras, E. Frise, V. Kaynig, M. Longair, T. Pietzsch, S. Preibisch, C. Rueden, S. Saalfeld, B. Schmid, J. Y. Tinevez, D. J. White, V. Hartenstein, K. Eliceiri, P. Tomancak and A. Cardona (2012). "Fiji: an open-source platform for biological-image analysis." Nat Methods **9**(7): 676-682.

Schwindt, P. C. and W. E. Crill (1995). "Amplification of synaptic current by persistent sodium conductance in apical dendrite of neocortical neurons." J Neurophysiol **74**(5): 2220-2224.

Segev, I., A. Friedman, E. L. White and M. J. Gutnick (1995). "Electrical consequences of spine dimensions in a model of a cortical spiny stellate cell completely reconstructed from serial thin sections." J Comput Neurosci **2**(2): 117-130.

Segev, I. and M. London (2000). "Untangling dendrites with quantitative models." Science **290**(5492): 744-750.

Simons, D. J. and G. E. Carvell (1989). "Thalamocortical response transformation in the rat vibrissa/barrel system." J Neurophysiol **61**(2): 311-330.

Simons, D. J. and T. A. Woolsey (1984). "Morphology of Golgi-Cox-impregnated barrel neurons in rat SmI cortex." J Comp Neurol **230**(1): 119-132.

Smith, P. H. and L. C. Populin (2001). "Fundamental differences between the thalamocortical recipient layers of the cat auditory and visual cortices." J Comp Neurol **436**(4): 508-519.

Smith, P. H., D. J. Uhlrich, K. A. Manning and M. I. Banks (2012). "Thalamocortical projections to rat auditory cortex from the ventral and dorsal divisions of the medial geniculate nucleus." J Comp Neurol **520**(1): 34-51.

Stanley, G. B., J. Jin, Y. Wang, G. Desbordes, Q. Wang, M. J. Black and J. M. Alonso (2012). "Visual orientation and directional selectivity through thalamic synchrony." J Neurosci **32**(26): 9073-9088.

Stevens, C. F. and Y. Wang (1995). "Facilitation and depression at single central synapses." Neuron **14**(4): 795-802.

Stratford, K. J., K. Tarczy-Hornoch, K. A. Martin, N. J. Bannister and J. J. Jack (1996). "Excitatory synaptic inputs to spiny stellate cells in cat visual cortex." Nature **382**(6588): 258-261.

Stuart, G. and B. Sakmann (1995). "Amplification of EPSPs by axosomatic sodium channels in neocortical pyramidal neurons." Neuron **15**(5): 1065-1076.

Stuart, G. and N. Spruston (1998). "Determinants of voltage attenuation in neocortical pyramidal neuron dendrites." J Neurosci **18**(10): 3501-3510.

Stuart, G., N. Spruston and M. Häusser (1999). Dendrites. Oxford ; New York, Oxford University Press.

Swadlow, H. A. (1995). "Influence of VPM afferents on putative inhibitory interneurons in S1 of the awake rabbit: evidence from cross-correlation, microstimulation, and latencies to peripheral sensory stimulation." J Neurophysiol **73**(4): 1584-1599.

Tapia, J. C., N. Kasthuri, K. J. Hayworth, R. Schalek, J. W. Lichtman, S. J. Smith and J. Buchanan (2012). "High-contrast en bloc staining of neuronal tissue for field emission scanning electron microscopy." Nat Protoc **7**(2): 193-206.

Tapia, J. C., J. D. Wylie, N. Kasthuri, K. J. Hayworth, R. Schalek, D. R. Berger, C. Guatimosim, H. S. Seung and J. W. Lichtman (2012). "Pervasive synaptic branch removal in the mammalian neuromuscular system at birth." Neuron **74**(5): 816-829.

Temereanca, S. and D. J. Simons (2003). "Local field potentials and the encoding of whisker deflections by population firing synchrony in thalamic barreloids." J Neurophysiol **89**(4): 2137-2145.

Turney, S. G., M. K. Walsh and J. W. Lichtman (2012). "In vivo imaging of the developing neuromuscular junction in neonatal mice." Cold Spring Harb Protoc **2012**(11): 1166-1176.

Van Kempen, G. M. P., L. J. Van Vliet, P. J. Verveer and H. T. M. Van Der Voort (1997). "A quantitative comparison of image restoration methods for confocal microscopy." Journal of Microscopy **185**(3): 354-365.

Vogels, T. P. and L. F. Abbott (2009). "Gating multiple signals through detailed balance of excitation and inhibition in spiking networks." Nat Neurosci **12**(4): 483-491.

Voigt, B. C., M. Brecht and A. R. Houweling (2008). "Behavioral detectability of single-cell stimulation in the ventral posterior medial nucleus of the thalamus." J Neurosci **28**(47): 12362-12367.

Wang, G. and S. J. Smith (2012). "Sub-diffraction limit localization of proteins in volumetric space using Bayesian restoration of fluorescence images from ultrathin specimens." PLoS Comput Biol **8**(8): e1002671.

Wang, Q., R. M. Webber and G. B. Stanley (2010). "Thalamic synchrony and the adaptive gating of information flow to cortex." Nat Neurosci **13**(12): 1534-1541.

Wehr, M. and A. M. Zador (2003). "Balanced inhibition underlies tuning and sharpens spike timing in auditory cortex." Nature **426**(6965): 442-446.

Wildanger, D., R. Medda, L. Kastrup and S. W. Hell (2009). "A compact STED microscope providing 3D nanoscale resolution." J Microsc **236**(1): 35-43.

Wilent, W. B. and D. Contreras (2005). "Dynamics of excitation and inhibition underlying stimulus selectivity in rat somatosensory cortex." Nat Neurosci **8**(10): 1364-1370.

Williams, S. R. and G. J. Stuart (2002). "Dependence of EPSP efficacy on synapse location in neocortical pyramidal neurons." Science **295**(5561): 1907-1910.

Wimmer, V. C., P. J. Broser, T. Kuner and R. M. Bruno (2010). "Experience-induced plasticity of thalamocortical axons in both juveniles and adults." J Comp Neurol **518**(22): 4629-4648.

Wimmer, V. C., R. M. Bruno, C. P. de Kock, T. Kuner and B. Sakmann (2010). "Dimensions of a projection column and architecture of VPM and POm axons in rat vibrissal cortex." Cereb Cortex **20**(10): 2265-2276.

Wimmer, V. C., T. Nevian and T. Kuner (2004). "Targeted in vivo expression of proteins in the calyx of Held." Pflugers Arch **449**(3): 319-333.

Woolsey, T. A. and H. Van der Loos (1970). "The structural organization of layer IV in the somatosensory region (SI) of mouse cerebral cortex. The description of a cortical field composed of discrete cytoarchitectonic units." Brain Res **17**(2): 205-242.

Xu, K., G. Zhong and X. Zhuang (2013). "Actin, spectrin, and associated proteins form a periodic cytoskeletal structure in axons." Science **339**(6118): 452-456.

Xu, N. L., M. T. Harnett, S. R. Williams, D. Huber, D. H. O'Connor, K. Svoboda and J. C. Magee (2012). "Nonlinear dendritic integration of sensory and motor input during an active sensing task." Nature **492**(7428): 247-251.

Yu, J. and D. Ferster (2010). "Membrane potential synchrony in primary visual cortex during sensory stimulation." Neuron **68**(6): 1187-1201.

Zucker, R. S. and W. G. Regehr (2002). "Short-term synaptic plasticity." Annu Rev Physiol **64**: 355-405.

Appendix A

Strategies tested for the correlative LM/EM protocol

The correlative LM/EM protocol was established after multiple unsuccessful attempts. Here I summarize each one and list the primary reason in parentheses for why it failed.

In all of these protocols I have listed the dendrite stain before the bouton stain, e.g. "SA-A488, VG2/A594".

Abbreviations:

TX: Triton-X

0perm/stage: No permeabilization, only using freezing stage to fracture membranes

0perm/80C: No permeabilization, placing tissue in -80˚C freezer to fracture membranes

SA-A488, SA-A594, SA-A647: Streptavidin-Alexa conjugates

SA-Au: Streptavidin-gold conjugate

SA-A488-NAu, SA-A594, SA-A647: Streptavidin-Alexa-nanogold triple conjugate

SA-Cy5: Streptavidin-cyanine conjugate

VG2: anti-VGluT2 primary antibody

A488, A594, A647: Alexa secondary antibodies

Cy5: Cyanine secondary antibody

α-A_Au: gold-conjugated anti-Alexa primary antibody

1- , **2Au-enhance**: single and double gold enhancement of gold particles

Ag-enhance: silver enhancement of gold particles

25-, 50µm: floating section thickness

P-Ox, **2P-Ox**: single photo-oxidation for dendrite alone, and double photo-oxidation for both dendrite and boutons

KCN: potassium cyanide[1]

NH_4Cl: Ammonium chloride

pre-O_2 treatment: high-O_2 photo-oxidation medium

high-NA: using an immersion lens with high numerical aperture

---

[1] No kidding.

epi pre-bleach: bleach the section's autofluorescence with a long exposure under the epifluorescence microscope

laser pre-bleach: bleach the section's autofluorescence with a long exposure under the confocal microscope

slow LM: long confocal imaging step (>48 hours)

HRP: horseradish peroxidase secondary antibody against anti-VGluT2 primary

BP535, **HCRed**, **Cy5**: filter cubes with different band-pass light filters to better control photo-oxidation

osm, **2osm**: single osmication and double osmication

Pb: lead stain

UA: uranyl acetate

TEM: Transmission Electron Microscopy

SEM: Scanning Electron Microscopy

1. TX dilution series (0.001% to 1%), SA-A488, VG2/A594, TEM

(ultrastructure washed out)

2. 0perm/stage, SA-A488/SA-Au/1Au-enhance, VG2/A594/α-A_Au/2Au-enhance, TEM

(very high background)

3. 0perm/stage, 50µm, SA-A488, VG2/A594, 2P-Ox

(bad penetration)

4. 0perm/stage, 25µm, SA-A488, VG2/A594, 2P-Ox

(bad penetration)

5. 0perm/80C, 25µm, SA-A488, VG2/A594 (long incubation), 2P-Ox

(very high background)

6. 0perm/80C, 25µm, SA-A488, VG2(AbCam)/A594, 2P-Ox

(high background)

7. 0perm/80C, 25µm, SA-A488, VG2/A594, Invitrogen DAB, 2P-Ox

(high background)

8. 0perm/80C, 25µm, SA-A488, VG2/A594, Dako DAB, 2P-Ox

(high background)

9. 0perm/80C, 25µm, SA-A488, VG2/A594, Dako DAB, KCN,

2P-Ox (high background)

10. 0perm/80C, 25µm, SA-A488, VG2/A594, Dako DAB, NH4Cl, 2P-Ox

(high background)

11. 0perm/80C, 25µm, SA-A488, VG2/A594, Dako DAB, pre-O_2 treatment, 2P-Ox

(high background)

12. 0perm/80C, 25µm, SA-A488, VG2/A594, Dako DAB, high pH, 2P-Ox

(high background)

13. 0perm/80C, 25µm, SA-A488, VG2/A594, Dako DAB, 2P-Ox, high-NA

(high backgound)

14. 0perm/80C, 25µm, SA-A488, VG2/A594, Dako DAB, 2P-Ox, high-NA, epi pre-bleach

(high background)

15. 0perm/80C, 25µm, SA-A488, VG2/A594, Dako DAB, 2P-Ox, high-NA, laser pre-bleach

(high background)

16. 0perm/80C, 25µm, SA-A488, VG2/A594, Dako DAB, 2P-Ox, high-NA, BP535/HCRed filter cubes

(high background)

17. 0perm/80C, 25µm, SA-A488, VG2/A594, Dako DAB, 2P-Ox, high-NA, HCRed/BP535 filter cubes

(high background)

18. 0perm/80C, 25µm, SA-Cy5, VG2/A594, Dako DAB, 2P-Ox, high-NA, Cy5/HCRed filter cubes

(Cy5 bleaching during confocal imaging)

19. 0perm/80C, 25µm, SA-A647, VG2/A594, minimal LM exposure, Dako DAB, 2P-Ox, high-NA, Cy5/HCRed filter cubes

(dendrite too dark under EM to distinguish PSDs)

20. 0perm/80C, 25µm, SA-A647, VG2/A594, minimal LM exposure, Dako DAB, 2P-Ox, high-NA, Cy5/HCRed filter cubes
(cell too light to find under EM; 2P-Ox calibration very tricky across consecutive experiments)

21. 0perm/80C, 25µm, SA-A647, VG2/A594, Dako DAB, 2P-Ox, high-NA, HCRed/BP535 filter cubes
(not enough VGluT2+ separation under EM)

22. 0perm/80C, 25µm, SA-A488, VG2/A594/HRP, Dako DAB, 2P-Ox, TEM
(too much section loss for serial EM + reconstructions)

23. 0perm/80C, 25µm, SA-A488, VG2/A594/HRP, Dako DAB, P-Ox, 2osm, SEM
(high background)

24. 0perm/80C, 25µm, SA-A488, VG2/A594/HRP, Dako DAB, P-Ox, Pb, SEM
(bad secondaries ratio)

25. 0perm/80C, 25µm, SA-A488, VG2/A594/HRP, Dako DAB, P-Ox, Pb, SEM
(dend too dark bc. of lead)

26. 0perm/80C, 25µm, SA-A488-NAu, VG2/A488-NAu, Au-enhance Pb,

(weak terminal signal)

27. 0perm/80C, 25µm, SA-A488-NAu, VG2/A594/HRP Pb,

(bad secondaries ratio)

28. 0perm/80C, 25µm, SA-A488-NAu, VG2/A594/HRP, slow LM Pb

(Na+ azide quenched HRP)

29. 0perm/80C, 25µm, SA-A488-NAu, VG2/A594/HRP, Au-enhance Pb

(enhancer doesn't penetrate sufficiently)

30. 0perm/80C, 25µm, SA-A488-NAu, VG2/A594/HRP, Ag-enhance, normal osm, UA, Pb, SEM

(washed out Ag)

31. 0perm/80C, 25µm, SA-A488-NAu, VG2/A594/HRP, Ag-enhance, normal osm, Pb, SEM

(washed out Ag)

32. 0perm/80C, 25µm, SA-A488-NAu, VG2/A594/HRP, fast LM, Ag-enhance, normal osm, UA, gold toning, Pb, SEM

(very high background)

33. 0perm/80C, 25µm, SA-A488-NAu, VG2/A594/HRP, Ag-enhance, low osm, Pb, SEM

(success)